LEABHARLANN CHOLÁISTE NA TRÍONÓIDE, BAILE ÁTHA CLIATH | TRINITY COLLEGE LIBRARY DUBLIN
Ollscoil Átha Cliath | The University of Dublin

Terms and Conditions of Use of Digitised Theses from Trinity College Library Dublin

Copyright statement

All material supplied by Trinity College Library is protected by copyright (under the Copyright and Related Rights Act, 2000 as amended) and other relevant Intellectual Property Rights. By accessing and using a Digitised Thesis from Trinity College Library you acknowledge that all Intellectual Property Rights in any Works supplied are the sole and exclusive property of the copyright and/or other IPR holder. Specific copyright holders may not be explicitly identified. Use of materials from other sources within a thesis should not be construed as a claim over them.

A non-exclusive, non-transferable licence is hereby granted to those using or reproducing, in whole or in part, the material for valid purposes, providing the copyright owners are acknowledged using the normal conventions. Where specific permission to use material is required, this is identified and such permission must be sought from the copyright holder or agency cited.

Liability statement

By using a Digitised Thesis, I accept that Trinity College Dublin bears no legal responsibility for the accuracy, legality or comprehensiveness of materials contained within the thesis, and that Trinity College Dublin accepts no liability for indirect, consequential, or incidental, damages or losses arising from use of the thesis for whatever reason. Information located in a thesis may be subject to specific use constraints, details of which may not be explicitly described. It is the responsibility of potential and actual users to be aware of such constraints and to abide by them. By making use of material from a digitised thesis, you accept these copyright and disclaimer provisions. Where it is brought to the attention of Trinity College Library that there may be a breach of copyright or other restraint, it is the policy to withdraw or take down access to a thesis while the issue is being resolved.

Access Agreement

By using a Digitised Thesis from Trinity College Library you are bound by the following Terms & Conditions. Please read them carefully.

I have read and I understand the following statement: All material supplied via a Digitised Thesis from Trinity College Library is protected by copyright and other intellectual property rights, and duplication or sale of all or part of any of a thesis is not permitted, except that material may be duplicated by you for your research use or for educational purposes in electronic or print form providing the copyright owners are acknowledged using the normal conventions. You must obtain permission for any other use. Electronic or print copies may not be offered, whether for sale or otherwise to anyone. This copy has been supplied on the understanding that it is copyright material and that no quotation from the thesis may be published without proper acknowledgement.

A non-perturbative study of the renormalisation of action parameters in anisotropic lattice QCD with applications to finite temperature QCD

by

Richard Morrin
B.A. (Mod.), M.Sc.

A Project submitted to
The University of Dublin
for the degree of

Doctor in Philosophy

School of Mathematics
University of Dublin
Trinity College

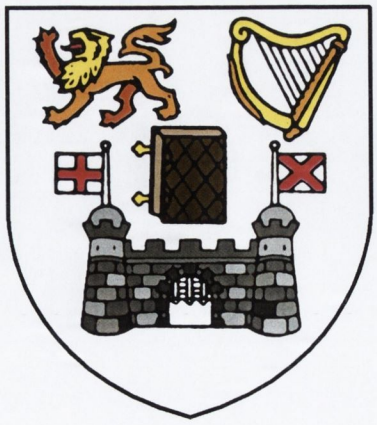

October, 2008

TRINITY COLLEGE
10 AUG 2009
LIBRARY DUBLIN
THESIS
8811

Declaration

This project has not been submitted as an exercise for a degree at any other University. Except where otherwise stated, the work described herein has been carried out by the author alone. This project may be borrowed or copied upon request with the permission of the Librarian, University of Dublin, Trinity College. The copyright belongs jointly to the University of Dublin and Richard Morrin.

Signature of Author ... .

Richard Morrin

31 March, 2009

Summary

The advantages of using anisotropic lattices, instead of the more usual isotropic lattices, in QCD simulations are well established. Anisotropic lattices can be used to increase signal resolution and allow computational overhead to be kept to a minimum while minimising finite volume effects. A fine temporal discretisation can be used to suppress mass-dependent errors which has considerable advantages; particularly for heavy quark simulations. Finite temperature field theory has a natural asymmetry which is ideally suited to an anisotropic lattice formulation.

This thesis starts with a general introduction to the field and continues with a brief overview of the techniques and improvements used in the course of the simulations conducted therein.

The use of an anisotropic lattice introduces two separate bare parameters into the quark and gluon actions. These parameters must be tuned so that the resulting physical measurements of the renormalised anisotropy are the same for both the gauge and fermion fields. This tuning procedure is trivial for quenched QCD. The increase of available computational power means that the introduction of dynamical fermions into simulations has become feasible. The introduction of these dynamical fermions complicates the tuning procedure considerably. A non-perturbative procedure for tuning these anisotropy parameters is presented and is shown to be successful.

Finite temperature lattice QCD provides a tool for investigation into the nature of the transition from the hadronic phase at low temperature to the quark-gluon plasma phase at high temperature. The equations of state of the quark-gluon plasma must be determined in order to understand its underlying properties. One of the methods which can be used to determine the equations of state requires the measurement of Karsch's anisotropy coefficients. These coefficients have proven to be notoriously difficult to calculate. Attempts have been made to calculate them perturbatively. However the perturbative coefficients are known to lead to pathological results such as negative pressure and a non-vanishing pressure gap at the deconfining phase of $SU(3)$ gauge theory. Non-perturbative attempts at their calculation have also been shown to be difficult. The gauge configurations used in the tuning procedure mentioned above are recycled along with a number of new simulations which allow for the investigation into the viability of an alternative method for the computation of the Karsch coefficients. Two approaches are attempted and are found to give consistent answers. The measured values are well behaved with reasonable associated statistical errors. It is concluded that this method holds considerable promise for the determination of the required coefficients.

Acknowledgements

I have to thank my supervisor Dr. Sinéad Ryan for all encouragement, assistance and patience provided over the five long years of this project. Thanks are also due to Dr. Michael Peardon who was my official acting supervisor for two six-month periods of maternity leave. Dr. Jonivar Skullerud supplied some valuable input, particularly into the Karsch section of this thesis.

I am grateful for all financial support from a number of sources over the course of this Ph.D. I held a Class II Studentship from Trinity College for three years, which provided a total of €12k, in return for performing a number of hours tutorials gratis each week during term time. I received two years of funding, totalling €16k, from PRTLI/IITAC/IRCSET award SC/03/393Y. That grant also paid for me to attend the BUSSTEPP 2004 Summer School held in Plymouth and my conference fee to attend Lattice XXIII, which was organised by the Trinlat group here in Trinity College Dublin. I was fortunate to receive another two years of funding, again totalling €16k, from SFI grant number 04/BRG/P0275. My first three years tuition fees were covered by the Trinity College Studentship mentioned above. Fees for the final two years were covered personally.

The School of Mathematics kindly provided me with the requisite facilities including office space and a computer. I was also able to avail of the ample opportunities to take on extra tutorials, maths help-rooms and a variety of revision and other short courses. The major computational work involved during this project was performed on clusters provided by the Trinity Centre For High Performance Computing.

Finally, I'd like to thank my parents; both in general and in particular for putting up with me messing about in college for so long.

A change of speed, a change of style.

Contents

List of Figures

List of Tables

Chapter 1

Introduction

Since the 1970's, most particle physicists have agreed that the elementary particles that make up matter consist of a set of fermions which interact primarily through the exchange of vector bosons. These elementary fermions include the quarks, $\binom{u}{d}, \binom{c}{s}, \binom{t}{b}$, and the leptons, $(e, \mu, \tau, \nu_e, \nu_\mu, \nu_\tau)$. All of these particles are spin-$\frac{1}{2}$ fermions.

These fermions interact through three forces, the *strong*, *weak* and *electromagnetic* forces. The strong interaction is responsible for nuclear binding and the interactions of the constituents of nuclei. The weak interaction is responsible for radioactive beta decay processes. The electromagnetic interaction is coupled minimally to all electrically charged quarks and leptons.

Each quark can come in one of three types, each denoted by a different "colour". Colour is the "charge" associated with the strong interaction. Quarks also carry an electric charge. Leptons do not carry a colour charge and do not participate in the strong interaction. The neutrinos do not carry any electric charge and do not participate in electromagnetic interactions. All of the particles may interact via the weak interaction which is mediated by the exchange of spin-1 bosons. The photon mediates the electromagnetic interaction, the heavy W and Z bosons mediate the weak interaction and the strong interaction is mediated by 8 massless colour-charged gluons.

The Standard Model (SM) of particle physics has been successful in synthesising

the strong, weak and electromagnetic forces, together into a single theory. Mathematically it can be described as a $SU(3) \times SU(2) \times U(1)$ gauge theory. The fourth and final fundamental interaction, gravity, is omitted from the SM. However at the energies with which the standard model is concerned, its effects are very weak when compared to the other three fundamental forces. Quantum Electrodynamics (QED) [1] mathematically predicts phenomena involving electrically charged particles interacting by means of exchange of photons. It successfully describes the electromagnetic interaction part of the SM. QED has the structure of an Abelian gauge theory with the symmetry group being U(1) gauge group.

A complete theory of the weak interaction requires the simultaneous incorporation of the electromagnetic interaction. The so-called electroweak interaction [2] of Glashow, Weinberg and Salam succeeded in unifying the weak and electromagnetic interactions under a $SU(2) \times U(1)$ gauge group.

The part of the Standard Model that deals with the strong force is called Quantum Chromodynamics (QCD) [3]. It is formulated in terms of quarks and gluons which are accepted as the basic degrees of freedom that make up hadronic matter. QCD has approximate flavour symmetry since the strong interaction does not discriminate between the different quark flavours. However the symmetry is broken by the differing masses of the quarks which vary in the range 1.5 Mev for the "up" quark to 173 Gev for the "top" quark.

Low-lying hadron spectra are well described by the quark model. However, attempts to produce single quarks in scattering experiments have proved fruitless. This can be understood as evidence that the force between two quarks is strong. Paradoxically, high-energy cross sections can be successfully described by the *parton model* [4] in which the quarks do not interact at all. The scattering amplitude of the QCD process

$$e^+e^- \rightarrow q\bar{q}, \tag{1.1}$$

where q and $\bar{q}$ are a quark and antiquark pair, can be accurately predicted by trivial changes to the QED process

$$e^+e^- \rightarrow \mu^+\mu^-, \tag{1.2}$$

without including any effects of the strong interaction of the produced quark and antiquark. This result is counter intuitive and shows that in the high energy limit, the effect of the strong interaction on the quark production process can be completely neglected. QCD successfully incorporates both kinds of behaviour via *confinement* [3] and *asymptotic freedom* [5, 6]. Asymptotic freedom means that the interaction between quarks reduces as the distance between them reduces (and hence energy increases), and tends to zero as the distance between them reduces to zero. Conversely, as the force between quarks does not diminish with increasing distance, it would take an infinite amount of energy to separate two quarks an infinite distance apart. If an attempt is made to separate a pair of quarks, then at some point, the energy required to produce a separation exceeds the pair production energy of a quark-antiquark pair and so it is more energetically favourable for a quark-antiquark pair to be produced. Quarks and gluons are only ever found inside colour-neutral hadrons. This aspect of the theory is verified within lattice QCD computations, but is not mathematically proven.

In the early 1970's, 't Hooft, Politzer, Gross and Wilczek [5, 6] discovered a class of asymptotically-free field theories in four dimensions. It was subsequently shown that these *non-Abelian gauge theories* are the only such theories [7]. Thus any attempt to construct an asymptotically free theory such as QCD must involve a non-Abelian gauge. QCD is a gauge theory of the SU(3) gauge group obtained by taking the colour charge to define a local symmetry

Tools for working with QCD include *perturbation theory* [3], *1/N expansion* [8] and various *effective theories* [9]. The masses of the up and down quarks are $\ll \Lambda_{\text{QCD}} \sim 200\text{Mev}$, the QCD scale. Chiral flavour symmetry is a good approximation to QCD for these quarks and chiral perturbation theory (ChPT) [10] has had some success in the non-perturbative regime of the strong interaction [11]. Wilson Chiral Perturbation Theory (WChPT) [12, 13] is an adaption of ChPT for the lattice. The mass of the strange quark $\sim$ 100Mev and the applicability of ChPT to the strange quark sector is under debate [14]. At the hadronic scale, the strong coupling constant, $\alpha_s \sim 1$, and so it becomes impossible to utilise perturbation theory to make accurate

predictions. Lattice QCD can be used to make non-perturbative QCD calculations. It can therefore be used as an important tool to test the effectiveness and accuracy of QCD and the standard model.

Chapter 2

QCD on the lattice

2.1 The QCD Lagrangian

As stated earlier in Chapter 1, QCD is a gauge theory of the SU(3) gauge group. A gauge theory is a theory that is based on the idea of gauge invariance [15]. This means that the theory is invariant under a gauge transformation. This invariance or gauge symmetry is a transformation that allows an independent symmetry transformation at every point in spacetime. Gauge symmetry is a fundamental principle that actually determines the form of the Lagrangian of the theory.

Considering an arbitrary continuous group of transformations which transform as

$$\psi(x) \rightarrow V(x)\psi(x), \tag{2.1}$$

with

$$V(x) = exp(i\alpha^a(x)t^a), \tag{2.2}$$

where the traceless Hermitian matrices, t^a, are the basic generators of the group. For $SU(3)$ t^a are taken to be the equal to $\frac{\lambda_a}{2}$ where λ_a are generalisations of the Pauli matrices and are known as Gell-Mann matrices. The generators of the group obey the usual Lie Algebra commutation relations $[t^a, t^b] = \sum_i^{N^2-1} f^{abc}t^c$ where f^{abc} are the "structure constants" of the group [16].

The difficulty in trying to construct a gauge invariant Lagrangian arises when try-

ing to consider terms involving derivatives. The standard definition of the derivative of $\psi(x)$ in the direction of a vector n^μ is

$$n^\mu \partial_\mu \psi = \lim_{\epsilon \to 0} \frac{1}{\epsilon} \left[\psi(x + \epsilon n) - \psi(x) \right]. \tag{2.3}$$

However, this definition can cause a problem for the case of fields which transform under Eqs. 2.1 as the two fields $\psi(x + \epsilon n)$ and $\psi(x)$ will transform differently. The solution is to define a "parallel transporter" which transforms as

$$U(y, x) \to V(y) U(y, x) V^\dagger(x). \tag{2.4}$$

This quantity can be used to define a more sensible derivative which is called the gauge covariant derivative

$$n^\mu D_\mu \psi = \lim_{\epsilon \to 0} \frac{1}{\epsilon} \left[\psi(x + \epsilon n) - U(x + \epsilon n, x) \psi(x) \right]. \tag{2.5}$$

For infinitesimal separation,

$$U(x + \epsilon n, x) = 1 + ig\epsilon n^u A^a_\mu t^a + \mathcal{O}(\epsilon^2), \tag{2.6}$$

where g is an arbitrarily extracted constant, called the coupling. The coefficient of the displacement, the vector field A^a_μ, is known as a connection. Eqs. 2.5 and 2.6 lead to the usual form of the covariant derivative

$$D_\mu = \partial_\mu - igA^a_\mu t^a. \tag{2.7}$$

The infinitesimal transformation law for A^a_μ is

$$A^a_\mu \to A^a_\mu + \frac{1}{g} \partial_\mu \alpha^a + f^{abc} A^b_\mu \alpha^c. \tag{2.8}$$

The gauge transformation of the covariant derivative has the same transformation

law as the field ψ,

$$D_\mu \psi(x) \to V(x) D_\mu \psi(x). \tag{2.9}$$

The commutator of covariant derivatives also follows the same transformation law

$$[D_\mu, D_\nu]\psi(x) \to V(x)[D_\mu, D_\nu]\psi(x). \tag{2.10}$$

The field tensor is defined by

$$[D_\mu, D_\nu] = -igF^a_{\mu\nu} t^a, \tag{2.11}$$

with

$$F^a_{\mu\nu} = \partial_\mu A^a_\nu - \partial_\nu A^a_\mu + g f^{abc} A^b_\mu A^b_\nu. \tag{2.12}$$

This quantity transforms as

$$F^a_{\mu\nu} t^a \to V(x) F^a_{\mu\nu} t^a V^\dagger(x), \tag{2.13}$$

or infinitesimally

$$F^a_{\mu\nu} \to F^a_{\mu\nu} - f^{abc} \alpha^b F^c_{\mu\nu}. \tag{2.14}$$

The required Lagrangian must be a gauge invariant function of ψ and its covariant derivatives and of $F^a_{\mu\nu}$ and its covariant derivatives and must also be invariant under global phase transformations. If further symmetries such as T (time-reversal) and P (parity) are required for the theory then the terms in the Lagrangian must not violate these symmetries. The field strength is not itself a gauge-invariant quantity, however it is trivial to form gauge invariant combinations of the field strengths. The simplest case is called the *Yang-Mills* Lagrangian

$$\mathcal{L}_{YM} = -\frac{1}{2}\mathrm{Tr}\left[(F^a_{\mu\nu} t^a)^2\right] = -\frac{1}{4}(F^a_{\mu\nu})^2. \tag{2.15}$$

which is a gauge invariant kinetic energy term for the fields A^i_μ. Up to operators of dimension four, there are only two other possible terms which satisfy the criteria

mentioned above. These two terms are the terms of the Dirac Lagrangian and adding these to the Yang-Mills pure gauge Lagrangian from Eq. 2.15 results in the QCD Lagrangian

$$\mathcal{L} = -\frac{1}{4}\sum_{a}(F^{a}_{\mu\nu})^2 + \sum_{f}\left[\bar{\psi}_f(i\not{D})\psi_f - m_f\psi_f\bar{\psi}_f\right], \tag{2.16}$$

where the Dirac and colour indices of the quark fields have been suppressed.

2.2 QCD on the Lattice

Lattice QCD (LQCD) is QCD formulated on a discrete four-dimensional Euclidean space-time grid using tools analogous to those used in statistical mechanics. Comprehensive introductions to the subject can be found in references [17, 18, 19, 20]. The basic numerical strategy is to approximate integrals using Monte Carlo simulations. The discrete space-time lattice is useful in that it also acts as a non-perturbative regularisation scheme by acting as an ultraviolet cut off at $\frac{\pi}{a}$ for a regular lattice. Renormalised physical quantities have a well behaved limit as the lattice spacing is taken to zero.

2.2.1 Path integral approach to QCD

The path integral approach to quantum mechanics can be most easily rationalised as a gedanken experiment extension of the classic two slit experiment. Considering the classic setup of a particle source S and a detector separated by a screen with two narrow holes A_1 and A_2 drilled into it. The pattern of arrivals at the detector at any point D is an interference pattern which can be explained as

$$\mathcal{A}(\text{Detected at D}) = \sum_{i}(\mathcal{A}(S \rightarrow A_i \rightarrow D).$$

If this screen is replaced by a screen with N holes drilled in it rather than two, then the same equation holds. Now placing another intermediate screen B with M holes in between screen A and the detector D one must find that the amplitude at D is

given by

$$\mathcal{A}(\text{Detected at D}) = \sum_i \sum_j (\mathcal{A}(S \rightarrow A_i \rightarrow B_j \rightarrow D).$$

The logical extension of this is to place an infinite number of screens in between the source and detector and then drill an infinite number of holes in each screen. Thus the amplitude for a particle to appear at the detector must be a sum of all amplitudes over all possible paths that the particle can take. In quantum mechanical notation we would have that the propagation of a state $\langle q^{'}, t^{'} | q, t \rangle = \int_q^{q^{'}} Dq e^{iS[q]}$ where S[q] is the action for real time. However this formalism is not suitable for numerical calculations as the paths are weighted with an oscillating function. To get around this problem a Wick rotation can be performed, $t \rightarrow -i\tau$. As a result $\langle q^{'}, t^{'} | q, t \rangle = \int_q^{q^{'}} Dq e^{-S_E[q]}$ where $S_E[q]$ is the Euclidean action. $\int_q^{q^{'}} Dq e^{-S_E[q]}$ is equivalent to the classical statistical mechanics partition function and thus there exists many equivalences between a Euclidean field theory and a classical statistical mechanics system.

2.2.2 Discretisation

LQCD is an attempt to numerically simulate QCD on a computer. Computers only have finite computing power and can only simulate a finite volume of space-time with a finite number of points in that space-time being sampled. The obvious structured way to implement this is to introduce a hypercubic grid in which points in the volume are sampled at regular intervals. The use of random lattices [21] has also been attempted but is currently unsuitable for computing realistic QCD properties.

Since space-time is discretised, so must the theory of QCD be discretised. The operators of the theory must be reformulated in terms of their lattice equivalents. A lattice version of a theory can only be accepted to be valid if the continuum theory is recovered as the lattice spacing goes to zero. Perhaps the simplest example of this is to consider the definition of a derivative of a simple one dimensional function $f(x)$ by first principles. It is given by

$$\frac{df(x)}{dx} = \lim_{h \rightarrow 0} \frac{f(x+h) - f(x)}{h}. \tag{2.17}$$

On an n-dimensional lattice for a quantity $U(x)$ this simply becomes

$$\frac{dU(x)}{dx_i} \approx \frac{U(x+a_i) - U(x)}{a_i}, \tag{2.18}$$

where x_i denotes the i^{th} direction and a_i is the lattice spacing in this direction. This example is what is known as a forward-difference approximation. An alternative strategy might be to use a central-difference approximation

$$\frac{df(x)}{dx} = lim_{h\to 0}\frac{f(x+h) - f(x-h)}{2h}. \tag{2.19}$$

The forward-difference approximation has error $\mathcal{O}(h)$ whereas the central difference approximation has error $\mathcal{O}(h^2)$. In order to reduce error in any simulation it is therefore desirable to choose appropriate discretisation schemes and also to try to keep the "step-size", h, as small as possible. On a lattice this corresponds to keeping the lattice spacing, a, as small as possible. Higher order derivatives can be found by recursively iterating one of the finite difference approximations. For example, iterating Eq. 2.19 leads to

$$\frac{d^4f(x)}{dx^4} = \lim_{h\to 0}\frac{f(x+4h) - 4f(x+2h) + 6f(x) - 4f(x-2h) + f(x-4h)}{16h^4}, \tag{2.20}$$

or by choosing a step-size of $\frac{h}{2}$ instead of h,

$$\frac{d^4f(x)}{dx^4} = \lim_{h\to 0}\frac{f(x+2h) - 4f(x+h) + 6f(x) - 4f(x-h) + f(x-2h)}{h^4}. \tag{2.21}$$

Various improved discretisation schemes exist. For example, by expanding the terms $f(x+h)$ etc. in a Taylor series, it can be easily seen that

$$\frac{1}{h}\left\{\frac{2}{3}[f(x+h) - f(x-h)] - \frac{1}{12}[f(x+2h) - f(x-2h)]\right\} = \frac{df}{dx} + \mathcal{O}(h^4). \tag{2.22}$$

Finite Volume Effects

As stated above, a computer may only simulate a finite number of space-time points. If the number of points being simulated is kept fixed but the spacing between ad-

jacent points is reduced then the volume of space-time being simulated is reduced. As the volume becomes smaller, errors due to *finite-volume effects* become more pronounced. Finite-volume effects have been studied extensively both analytically [22] and numerically [23]. Studies show that the shift between masses measured on a finite lattice and the infinite volume masses decrease exponentially to zero with increasing lattice size. Comparisons between full and quenched QCD simulations have shown that finite-size effects are smaller for the quenched case [24]. The difference between quenched and unquenched simulations will be explained in detail in Chapter 3.

Ideally one should have $\zeta \ll L$ where ζ is the quantity that determines the rate of the exponential decay of a correlation function (i.e. the correlation length) and L is the linear length of the lattice. In order to obtain good measurements of any quantity it is also statistically important that the lattice spacing is much less than the correlation length so that the relatively fine mesh will sufficiently sample the quantity that is being modelled or measured. One must therefore have $a \ll \zeta \ll L$ in any simulation.

2.3 Continuum Limit

Due to the fact that any simulation is done on a finite lattice with finite lattice spacing it follows that in order to determine physical values from any simulations it is necessary to take the double limit $a \to 0$ and $V \to \infty$ in order to reach the continuum limit values.

The algorithms used in lattice QCD simulations become progressively slower for decreasing quark mass values so simulations are performed at larger quark masses than the physical values of the up and down quarks. Therefore, predictions obtained for hadrons which contain up or down quarks may also require a further extrapolation down to small quark mass [25].

2.4 Construction of Actions

The Euclidean space equivalent of the QCD Lagrangian density of Eq. 2.16 is given by

$$\mathcal{L} = -\frac{1}{4}F^{\alpha}_{\mu\nu}F^{\mu\nu}_{\alpha} + \sum_{f}\bar{\psi}_f\gamma_\mu[\partial_\mu - igA^{\alpha}_{\mu}t_\alpha]\psi_f + \sum_{f} m_f\bar{\psi}_f\psi_f, \tag{2.23}$$

where $\alpha = 1, \ldots, 8$ is the gluon-colour index, f is the flavour index and t_α are the generators of $SU(3)$. In order to successfully reproduce QCD on the lattice, one must design a lattice version of this quantity which reduces to the continuum Lagrangian in the limit $a \rightarrow 0$.

2.4.1 Gluon action

The gluonic part of the continuum QCD action is given earlier in Eq. 2.15. The lattice version of this action will have a number of arbitrary input parameters. In order to recover the continuum action, these input parameters may have to be tuned. The number of input parameters will be affected by the choice and properties of the lattice action. QCD is invariant with respect to gauge transformations. With explicit gauge invariance the quark-gluon, three-gluon and four-gluon couplings are equal and the bare gluon mass is equal to zero. If gauge invariance is broken then these couplings must be independently tuned and a gluon mass introduced in order to recover QCD. This procedure would be very expensive so it would be highly advantageous to preserve gauge invariance. It would be possible to formulate QCD directly in terms of the gauge fields A_μ however the resulting theory would only have approximate gauge invariance.

A gauge invariant lattice Lagrangian must be constructed from objects which themselves are gauge invariant.

The operator constructed from the parametrised path ordered integral running from $s = 0$ at $x = y$ to $s = 1$ at $x = z$

$$U_{\mathcal{P}}(z, y) = \mathcal{P}\left\{exp\left[ig\int_0^1 ds\frac{dx^\mu}{ds}A^a_\mu(x(s))t^a\right]\right\}, \tag{2.24}$$

satisfies Eq. 2.4. $\mathcal{P}$ denotes the path ordering operation. The path ordering is a necessary construct for a non-Abelian group. This quantity is known as a *Wilson line*. Note also that $U_{\mathcal{P}}(z,y) = U^{\dagger}_{\mathcal{P}}(y,z)$ from this definition. One possible gauge invariant quantity is a Wilson line capped by a fermion and an anti-fermion i.e.

$$\bar{\psi}(z)U_{\mathcal{P}}(z,y)\psi(y) \rightarrow \bar{\psi}(z)V^{\dagger}(z)V(z)U_{\mathcal{P}}(z,y)V^{\dagger}(y)V(y)\psi(y) = \bar{\psi}(z)U_{\mathcal{P}}(z,y)\psi(y), \tag{2.25}$$

where the fermion field ψ transforms as in Eq. 2.1. The only other gauge invariant quantity that can be constructed using $U_{\mathcal{P}}(z,y)$ is $\mathrm{Tr}U_{\mathcal{P}}(x,x)$ where $U_{\mathcal{P}}(x,x)$ is taken about a closed loop. Considering a path taken about a small square of size a in the $\mu\nu$ plane

$$U_{\mathcal{P}}(x,x) = U_{\mathcal{P}}(x, x+a\hat{\mu})U_{\mathcal{P}}(x+a\hat{\mu}, x+a\hat{\mu}+a\hat{\nu})U_{\mathcal{P}}(x+a\hat{\mu}+a\hat{\nu}, x+a\hat{\nu})U_{\mathcal{P}}(x+a\hat{\nu}, x). \tag{2.26}$$

Substituting the discretised version of Eq. 2.24 into 2.26 and expanding up to order a^2 results in

$$U_{\mathcal{P}}(x,x) = 1 + iga^2 F^b_{\mu\nu}(x)t^b - \frac{g^2a^4}{2}\left(F^c_{\mu\nu}(x)t^c\right)^2 + (a^6). \tag{2.27}$$

This expression is not gauge invariant as the field strength tensor transforms as in Eq. 2.13 above and thus $F^b_{\mu\nu}(x)t^b$ is not gauge invariant. However, taking the trace of $U_{\mathcal{P}}(x,x)$ is gauge invariant i.e.

$$\mathrm{Tr}U_{\mathcal{P}}(x,x) \rightarrow \mathrm{Tr}U_{\mathcal{P}}(x,x). \tag{2.28}$$

To transcribe the above derivations to the lattice, one needs to simply consider a square in the $\mu\nu$ plane, as in Fig. 2-1. In this case, the path integral, Eq. 2.24 is taken along a straight line, say from the point x to a point $x + a\hat{\mu}$ in the $\hat{\mu}$ direction, i.e $U(x, x+a\hat{\mu})$. For compactness, this can be written as $U_{\mu}(x)$. $U_{\mu}(x)$ is also known as a link variable and can be thought of as "living" on the links connecting adjacent

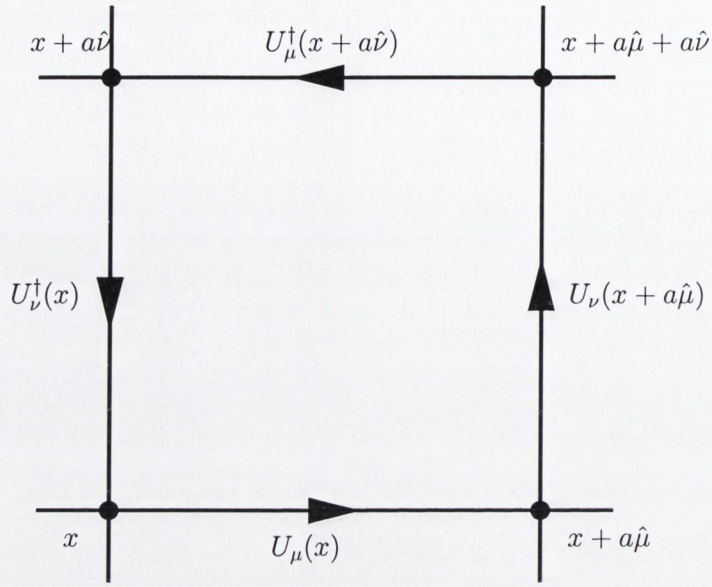

Figure 2-1: A diagram showing an elementary 1×1 plaquette or Wilson loop

lattice sites. The unit 1×1 plaquette can be written as

$$W_{\mu\nu}^{1\times1} = U_\mu(x)U_\nu(x+\hat{\mu})U_\mu^\dagger(x+\hat{\nu})U_\nu^\dagger(x). \tag{2.29}$$

From Eq. 2.27 above and using the identities from Sec. 2.1 it can be shown that the following combination, taken over the sum of plaquettes P,

$$\begin{aligned}\beta\sum_P\left[1-\frac{1}{2N}\mathrm{Tr}(W_{\mu\nu}^{1\times1}+(W_{\mu\nu}^{1\times1})^\dagger)\right] =&\beta\sum_x\sum_{\mu<\nu}\left[\frac{1}{2N}\mathrm{Tr}\left(a^4g^2\left(F_{\mu\nu}^c(x)t^c\right)^2\right)\right]+\mathcal{O}(a^2),\\ =&\beta\frac{a^4g^2}{2N}\sum_x\sum_{\mu,\nu}\mathrm{Tr}\left(F_{\mu\nu}^c(x)t^c\right)^2+\mathcal{O}(a^2),\end{aligned} \tag{2.30}$$

In the limit $a \to 0$ this becomes

$$\beta\frac{g^2}{2N}\frac{1}{4}\int d^4x\left(F_{\mu\nu}^b\right)^2, \tag{2.31}$$

which reduces to the continuum gluon action for $\beta = \frac{2N}{g^2}$. $(W_{\mu\nu}^{1\times1})^\dagger$ corresponds to a path integral taken around the same 1×1 unit square as $W_{\mu\nu}^{1\times1}$, but in the opposite direction. Taking the combination $\left(W_{\mu\nu}^{1\times1}+(W_{\mu\nu}^{1\times1})^\dagger\right)$ ensures the hermiticity of the action. As QCD is an $SU(3)$ gauge theory, the gluonic part of the action can be

written by taking $N = 3$ in the above equation.

$$S_G[U] = \beta \sum_x \sum_{\mu<\nu} \frac{1}{3} \mathrm{ReTr}\left[1 - W_{\mu\nu}^{1\times1}(x)\right], \tag{2.32}$$

using the fact that $\left(\frac{1}{2}(W_{\mu\nu}^{1\times1} + W_{\mu\nu}^{1\times1})^\dagger = \mathrm{Re}[W_{\mu\nu}^{1\times1}]\right)$. This action is called the *Wilson Action*. This action has discretisation error $\mathcal{O}(a^2)$. This example is constructed using only 1×1 Wilson loops. The use of small loops reduces computational costs and also reduces the size of discretisation errors. More accurate lattice gauge actions can be constructed by the addition of other types of loops as shown in Sec 2.6 below.

2.5 Quark Actions

From Eq. 2.23 we can write the quark part of the QCD Lagrangian as

$$S_F = \sum_x \sum_f \bar{\psi}_f(x)(\gamma_\mu \nabla_\mu + m_f)\psi_f(x). \tag{2.33}$$

where ∇_μ is the the gauge covariant symmetrised difference operator [26]

$$\nabla_\mu \psi(x) = \frac{1}{2a} \sum_\mu \left[U_\mu(x)\psi(x+\hat{\mu}) - U_\mu^\dagger(x-\hat{\mu})\psi(x-\hat{\mu})\right], \tag{2.34}$$

The use of a symmetrised difference is needed in order to preserve the hermiticity of the theory. However this means that while the lattice spacing is a, the derivative involves twice the lattice spacing. This leads to the appearance of so-called "*doublers*" into the theory. In other words the fermion propagator will have $2^d = 16$ poles in the first Brillouin zone at $(0,0,0,), \ldots, (\pi,\pi,\pi,\pi)$ rather than the physically expected one. The theory must be modified in order to correct for this.

2.5.1 Wilson Action

A lattice action need only reduce to the continuum action in the limit $a \to 0$. Therefore additional irrelevant operators can be added to the action as long as the effect of those operators vanishes as the spacing goes to zero. This is called *universality*.

Ref. [27] uncovered a "universality anomaly", however this anomaly was shown to be independent of the gauge field and hence physically inconsequential [28]. These additional operators can be used to reduce error in the model or to solve other problems such as the doubling problem mentioned in section 2.5 above. The Wilson Action [29] is obtained by introducing a second derivative term to the naive action. The so-called "Wilson term" is given by $ar\bar{\psi}\Box\psi$ where

$$\Box_\mu \psi(x) = \frac{1}{a_\mu^2}\left[\psi(x+\hat{\mu}) + \psi(x-\hat{\mu}) - 2\psi(x)\right]. \tag{2.35}$$

Explicitly, the Wilson Action is written as

$$S_W = \sum_x \sum_f \bar{\psi}_f \left(\gamma_\mu \nabla_\mu + m_f - a_\mu \frac{r}{2}\Box_\mu\right)\psi_f \tag{2.36}$$

The effect of this extra term is that the extra fifteen species at $p = \pi$ get a mass proportional to $\frac{r}{a}$. As the lattice spacing goes to zero, these doublers become infinitely heavy and decouple from the theory. As this added term is essentially the mass term for doublers, the chiral symmetry is violated even in the limit of vanishing bare quark mass. While Wilson fermions are computationally inexpensive, the approach to the continuum limit is slow. Observables are spoiled by the large $\mathcal{O}(a)$ discretisation errors and quantitative extrapolations to the continuum limit must be performed from simulations done at small lattice spacings, typically less than 0.1 fm. This necessitates the use of very large four-dimensional lattices in order to provide reasonable physical simulation volumes

2.6 Improvements

2.6.1 Symanzik Improvement

In order to successfully simulate any process, one should have a situation where the lattice spacing is much smaller than the physical scale in order to minimise discretisation errors. The physical scale should also be much smaller than the box-size

in order to reduce finite-volume effects. However, finite computational power places limits on the number of points which can be simulated, so a balance must be reached between discretisation and finite-volume effects. One possible strategy is to try to improve the model that is being simulated in order to reduce the discretisation effects. Symanzik introduced a systematic way of improving corrections to the continuum theory from finite lattice spacing by modifying lattice actions with added irrelevant terms. These irrelevant terms can be chosen to compensate for some of the systematic errors due to finite spacing. It is theoretically possible to eliminate errors to any order in a by the addition of suitable terms. These terms are higher dimension improvement terms which mimic the effects of the ultraviolet modes which are removed due to the lattice cut-off. In Ref. [30] the basic principles were outlined and applied to ϕ^4 theory and the procedure was also applied to the non-linear sigma model in Ref. [31]. A preliminary investigation for pure Yang-Mills theory in four dimensions was given in Ref. [32]. Ref. [33] looked at the addition of the most basic dimension six term i.e. the 2×1 rectangle, to the Wilson action and found that this was sufficient to remove errors of $\mathcal{O}(a^2)$. This result was verified by [34] from calculation of the small-a expansion of the static potential in 1-loop order. Symanzik's original approach was to remove the $\mathcal{O}(a^2)$ artifacts from Green's functions but this led to a problem as Green's functions are not gauge invariant. A solution for this problem was given by Lüscher and Weisz [35] who implemented on-shell improvement by removing $\mathcal{O}(a^2)$ artifacts from spectral quantities only. On-shell improved refers to taking the "minimal" improvement condition which is that the error term is reduced to $\mathcal{O}(a^2)$ for all low lying energy values.

2.6.2 Tadpole improvement

Tadpole (or mean-field) improvement refers to the procedure in which gauge fields are re-scaled by a factor u_0. As mentioned in Sec. 2.4.1, lattice perturbation theory is performed by expanding the link variable as

$$U_\mu(x) = exp[iagA_\mu(x)] \rightarrow 1 + iagA_\mu(x) - \frac{a^2g^2}{2}A_\mu(x)^2 + \dots . \tag{2.37}$$

The higher order terms in this expression represent higher order vertices that are purely lattice artifacts. At a first glance, it would seem that contributions from higher order terms in this expansion would decrease as $a \rightarrow 0$. However if the factors of gaA_μ in $\frac{a^2g^2}{2}A_\mu(x)^2 + \ldots$ are contracted with each other, the result is ultraviolet divergences that exactly cancel out the additional powers of a meaning that the higher order terms are only suppressed by powers of g^2 and do not vanish in the limit $a \rightarrow 0$. The solution proposed by Lepage and Mackenzie [36] was to separate out the gauge field into ultraviolet and infrared (IR) parts and to rewrite Eq. 2.37 as

$$U_\mu(x) \rightarrow u_0 e^{iagA_\mu^{IR}} \approx u_0 \left(1 + iagA_\mu(x)\right), \tag{2.38}$$

where the mean field parameter, u_0, is the averaged ultraviolet contribution. u_0 depends on the parameters of the theory and can be easily measured in a simulation. One common choice uses the plaquette expectation value:

$$u_0 = \left(\frac{1}{3}\langle \mathrm{Tr} U_\mathrm{P} \rangle\right)^{\frac{1}{4}}. \tag{2.39}$$

Other possible definitions include setting u_0 equal to the expectation value of the link operator in the Landau gauge are based on such things as the expectation value for long Wilson lines or the critical hopping parameter for Wilson quarks.

In order to incorporate tadpole-improvement into a simulation, one must simply make the substitution,

$$U_\mu^{'}(x) = \frac{1}{u_0} U_\mu(x), \tag{2.40}$$

wherever a link U_μ appears in a lattice operator. The factors u_0 may alternatively be absorbed into couplings or masses. The new fields are much closer to their continuum values since this simple rescaling cancels out much of the tadpole effects. It was shown in Ref. [37] that tadpole-improved actions could give good results even on relatively coarse lattices. A comparison of a tadpole-improved action with a non-tadpole-improved action can be seen in Ref. [38].

Other improvements for gauge actions

An alternative to the tree-level and one-loop improvements introduced by Symanzik (Sec. 2.6.1) is an approach based on the renormalisation group (RG) [39, 40]. Blocking transformations are used to transform the action. These transformations change the lattice cut off but leave the long range properties of the system intact. In the space of coupling constants, the blocking transformation makes a transition for a point S to a new point S'. By repeating this transformation, trajectories are obtained through coupling space. These trajectories define what is known as the renormalisation group flow. There is a special trajectory which starts at the ultraviolet fixed point. This is denoted the renormalised trajectory. On this renormalised trajectory, the information corresponding to the continuum physics is preserved. This leads to the concept of the so-called "perfect action" [41]. If one can find a renormalised trajectory which corresponds to blocking transformation, it provides an action which gives accurate results corresponding to the continuum limit. However these actions do not parametrise well and are expensive to simulate. A comprehensive introduction to perfect actions can be found in Ref. [42]. The Iwasaki Action [43] defines a distance from an action to the renormalised trajectory and then uses perturbation theory to choose an action which is closest to that trajectory. The DBW2 (Double Blocked Wilson) action [44] estimates the renormalised trajectory using the Schwinger-Dyson method. These actions use 1×1 and 1×2 Wilson loops in their construction i.e. are of the form

$$S[U] = \beta \sum_{\mu<\nu,x} \left[c_0 \mathrm{Tr} W_{\mu\nu}^{1\times 1}(x) + c_1 \mathrm{Tr} W_{\mu\nu}^{1\times 2}(x) \right], \tag{2.41}$$

and differ from each other by choice of the coefficient c_1. The choices for the three actions mentioned above are

$$c_1 = \begin{cases} \frac{1}{2} & \text{Symanzik} \\ -0.331 & \text{Iwasaki} \\ -1.409 & DBW2 \end{cases} \tag{2.42}$$

The universality of the Iwasaki and DBW2 actions were discussed in Ref. [45].

Other formulations use 1×1 and 2×2 Wilson loops e.g Beinlich-Karsch-Laermann. This tree level improved action was shown to reduce finite cut-off effects in the thermodynamics of SU(N) gauge theories [46].

2.7 Improved Quark Actions

It was shown above in Sec. 2.5.1 how to eliminate the problem of doublers by adding a dimension-five lattice-laplacian operator. Following on from the discussion of Symanzik improvement, it is possible to achieve $\mathcal{O}(a)$ improvement by including all possible gauge invariant, local dimension-five operators which respect the symmetries of QCD. However, it turns out that the only dimension-five operator explicitly needed [47] to improve the Wilson action to $\mathcal{O}(a)$ is the "clover" term,

$$\mathcal{O}_1 = -\frac{igaC_{SW}r}{4}\bar{\psi}\,\sigma_{\mu\nu}\,F_{\mu\nu}\,\psi. \tag{2.43}$$

The addition of this term to the Wilson action given above results in the Sheikholeslami-Wohlert action [47]

$$S_{SW} = S_W - \frac{igaC_{SW}r}{4}\sum_x \bar{\psi}(x)\sigma_{\mu\nu}F_{\mu\nu}\,\psi(x), \tag{2.44}$$

where S_W is given above in Eq. 2.36. C_{SW} is the clover coefficient which can be tuned to completely remove $\mathcal{O}(a)$ artifacts.

Further improvement is given by the "D234" action [48]. This action also includes the clover term from the Sheikholeslami-Wohlert action along with second, third and fourth order derivative terms. The tadpole-improved form is given by

$$\begin{aligned} m_0 + \sum_\mu \Big(& \gamma_\mu \Delta_\mu^{(1)} - ba^2 \gamma_\mu \Delta_\mu^{(1)} \Delta_\mu^{(2)} \\ & - \frac{ra}{2}\Big(\Delta_\mu^{(2)} + \frac{1}{2}\sum_\nu \sigma_{\mu\nu}F_{\mu\nu}\Big) + ca^3 \Delta_\mu^{(2)} \Delta_\mu^{(2)} \Big), \end{aligned} \tag{2.45}$$

where $b = 1/6, r = 2/3, c = 1/12$,

$$\begin{aligned}\Delta_\mu^{(1)}\psi(x) &= \frac{1}{2a}\Big(\tilde{U}_\mu(x)\psi(x+\mu) \\ &\quad - \tilde{U}_{-\mu}(x)\psi(x-\mu)\Big), \qquad (2.46)\\ \Delta_\mu^{(2)}\psi(x) &= \frac{1}{a^2}\Big(\tilde{U}_\mu(x)\psi(x+\mu) \\ &\quad + \tilde{U}_{-\mu}(x)\psi(x-\mu) - 2\psi(x)\Big), \qquad (2.47)\end{aligned}$$

and $\tilde{U} = U/u_0$, where $(u_0)^4$ is the tadpole-improved link variable. Classically the D234 action has $\mathcal{O}(a^3)$ errors.

2.8 Anisotropic Actions

The use of anisotropic lattices [49] offers further scope for improvements in designing lattice actions. As mentioned above in Sec. 2.6.1, it is possible to reduce the systematic errors associated with any action to any given order, $\mathcal{O}(a^n)$. If there are different temporal, a_t, and spatial, a_s, spacings present then it may be beneficial to concentrate on improving the action to a higher order in a_s in the case where $a_s > a_t$. The signal to noise ratio of correlation functions decays exponentially. This will be further expanded upon in Sec. 2.10. With a finer temporal lattice spacing, there are more points to fit a signal to over a given distance, resulting in a more accurate fit. This is particularly important for particles with bad signal to noise ratios such as glueballs. Anisotropic lattices also alleviate potential problems due to unphysical branches in the quark dispersion relation. These unphysical branches or "ghosts" are generic to all actions improved beyond $\mathcal{O}(a)$. The energies of these ghosts are at the scale of the temporal cutoff. Therefore using a lattice with $a_t < a_s$ will push up the energy of the ghosts and decouple them. Independent derivatives with respect to temperature and volume are needed in order to fully determine thermodynamic quantities. The easiest way to achieve this is to have independent spatial and temporal spacings. Due to Euclidean invariance, the fine lattice spacing can be considered as a spatial direction. This can be beneficial for studying large spatial momenta which

are phenomenologically important for form factors for example.

The new coefficients of the action must be tuned to restore Euclidean invariance. The anisotropic actions used in the course of this study are given below.

2.8.1 Anisotropic gluon action

The isotropic Wilson action given above in Eq. 2.32 must be modified for the anisotropic case, $a_s \neq a_t$. Defining the anisotropy ratio, ξ_g,

$$\xi_g = \frac{a_s}{a_t}, \tag{2.48}$$

and the plaquette operator $P_{\mu\nu}$ as

$$P_{\mu\nu}(x) = \frac{1}{N}\mathrm{ReTr}W^{1\times 1}_{\mu\nu}, \tag{2.49}$$

then the action can be written as

$$S_G[U] = \beta\left(\xi_g\Omega_t + \frac{1}{\xi_g}\Omega_s\right). \tag{2.50}$$

The new terms in Eq. 2.50 are discretisations of the magnetic and electric field strengths

$$\Omega_s = \sum_x\sum_{i,j}(1 - P_{ij}(x)) = \frac{\xi_g}{\beta}\int d^4x\mathrm{Tr}B^2 + \mathcal{O}(a^2), \tag{2.51}$$

and

$$\Omega_t = \sum_x\sum_{i}(1 - P_{i0}(x)) = \frac{1}{\xi_g\beta}\int d^4x\mathrm{Tr}E^2 + \mathcal{O}(a^2), \tag{2.52}$$

where i, j are spatial indices.

The specific gauge action used in the course of this project is a two-plaquette Symanzik-improved action [50] previously developed for high-precision glueball stud-

ies and given by

$$
\begin{aligned}
S_G =& \frac{\beta}{\xi_g^0}\left\{\frac{5(1+\omega)}{3u_s^4}\Omega_s - \frac{5\omega}{3u_s^8}\Omega_s^{(2t)} - \frac{1}{12u_s^6}\Omega_s^{(R)}\right\} \\
&+ \beta\xi_g^0\left\{\frac{4}{3u_s^2u_t^2}\Omega_t - \frac{1}{12u_s^4u_t^2}\Omega_t^{(R)}\right\},
\end{aligned}
\tag{2.53}
$$

where Ω_s and Ω_t are spatial and temporal plaquettes. Ω_s^R and Ω_t^R are 2×1 rectangles in the (i,j) and (i,t) planes respectively. Ω_s^{2t} is constructed from two spatial plaquettes separated by a single temporal link. u_s and u_t are the mean spatial and temporal gauge link values respectively. The factor ξ_g^0 is the input anisotropy for the gluon sector. The action has leading discretisation errors of $\mathcal{O}(a_s^4, a_t^2, \alpha_s a_s^2)$.

2.8.2 Quark Action

Following on from the isotropic actions mentioned above in Sec. 2.7, their anisotropic equivalents are given as

$$
M_{\mathrm{SW}} = m_c(1+\frac{1}{2}ra_0m_c) + \not{\nabla} - \frac{1}{2}ra_0\sum_\mu \Delta_\mu - \frac{1}{4}ra_0\,\sigma\cdot F\,, \tag{2.54}
$$

for the Sheikholeslami-Wohlert action and

$$
\begin{aligned}
M_{\mathrm{D234}} =& \; m_c(1+\frac{1}{2}ra_0m_c) + \sum_\mu \gamma_\mu\nabla_\mu\left(1 - b_\mu a_\mu^2\Delta_\mu\right) \\
&-\frac{1}{2}ra_0\Big(\sum_\mu \Delta_\mu + \frac{1}{2}\sigma\cdot F\Big) + \sum_\mu c_\mu a_\mu^3\Delta_\mu^2,
\end{aligned}
\tag{2.55}
$$

with $b_\mu = \frac{1}{6}, c_\mu = \frac{ra_0}{24a_\mu}$ for the generic D234 anisotropic action.

The fermionic action used in the course of this study is a D234-type action which has been specifically designed for large anisotropies. The usual Wilson term removes doublers in the temporal direction whereas spatial doublers are removed by the addition of a Hamber–Wu [51] term. The action has been described in detail in Ref. [52] and has leading classical discretisation errors of $\mathcal{O}(a_t m_q)$. In terms of continuum

operators, it can be written

$$S_q = \int d^4x\, \bar{\psi}(\not{D} + m_0)\psi - \frac{r a_t}{2} \int d^4x\, \bar{\psi}\left(D_0^2\right)\psi + s a_s^3 \int d^4x\, \bar{\psi} \sum_i D_i^4 \psi, \qquad (2.56)$$

which highlights the different treatment of temporal and spatial directions. r is the usual Wilson coefficient which is applied in the temporal direction only in this action and is set to unity. The analogous parameter in the spatial directions is s $(= \frac{1}{8})$, which parameterises a term that is irrelevant in the continuum limit. In terms of lattice parameters this action can be written as

$$\begin{aligned} M\psi = \frac{1}{a_t}\Bigg\{ \left(m_0 a_t + r + \frac{18s}{\xi_q^0}\right)\psi(x) + \frac{1}{2u_t}\Big[(\gamma_0 - r)U_t(x)\psi(x+\hat{t}) - (\gamma_0 + r)U_t^\dagger(x-\hat{t})\psi(x-\hat{t})\Big] \\ + \frac{1}{\xi_q^0}\frac{1}{u_s}\sum_i \Bigg[\left(\frac{2}{3}\gamma_i - 4s\right)U_i(x)\psi(x+\hat{i}) - \left(\frac{2}{3}\gamma_i + 4s\right)U_i^\dagger(x-\hat{i})\psi(x-\hat{i}) \\ - \frac{1}{u_s}\left(\left(\frac{1}{12}\gamma_i - s\right)U_i(x)U_i(x+\hat{i})\psi(x+2\hat{i}) - \left(\frac{1}{12}\gamma_i + s\right)U_i^\dagger(x-\hat{i})U_i^\dagger(x-2\hat{i})\psi(x-2\hat{i})\right)\Bigg]\Bigg\}. \end{aligned} \qquad (2.57)$$

Eq. 2.57 is obtained from Eq. 2.56 using finite difference schemes analogous to those discussed in Sec. 2.2.2. As this action is intended to be used on lattices with $a_s > a_t$, the improved lattice derivative, (see E.q. 2.22), is used to discretise the $\gamma_i D_i$ terms in order to improve the action to $\mathcal{O}(a_s^2)$. Unimproved central difference lattice derivatives are used for the remainder of the terms. The link variables $U_\mu(x)$ are included to preserve gauge invariance of the derivatives. The factors u_s, u_t are the tadpole improvement coefficients in the spatial and temporal directions respectively.

2.9 Numerical simulations of QCD

The QCD partition function has the form

$$\mathcal{Z} = \int DU D\bar{\psi} D\psi e^{-S}, \qquad (2.58)$$

where ψ and $\bar{\psi}$ are the fermionic and anti-fermionic fields respectively and U are the background gauge fields. The expected value of any measurement is given by

$$\langle \mathcal{O} \rangle = \frac{1}{\mathcal{Z}} \int DU D\bar{\psi} D\psi \mathcal{O} e^{-S}. \tag{2.59}$$

The QCD action can be split up into gluon and quark parts, $S = S_g + S_q$. The quark action will be of the form

$$S_q = \bar{\psi} M \psi,$$

where M is the fermion matrix. The fermion fields ψ are Grassman variables and because of this the S_q part of Eq. 2.58 can easily be integrated out analytically to give

$$\mathcal{Z} = \int DU \det(M(U)) e^{-S_g}. \tag{2.60}$$

The integral in Eq. 2.60 can be approximated by the usual method of Monte Carlo integration. The Monte Carlo technique for estimating the expected value of $f(x)$ is simply to randomly choose N variables x_i and take

$$\mathbb{E}(f(x)) = \lim_{N \to \infty} \frac{1}{N} \sum_{i=1}^{N} f(x_i) P(x_i). \tag{2.61}$$

Where $P(x_i)$ is the probability that a given x_i will occur. This method can be very wasteful as often time is wasted exploring areas of phase space which have very low probability of occurring. A more economic way of estimating a quantity is to use the method of importance sampling. For the simple example given above, the method is modified in that the random x_i are no longer taken from a flat distribution. Instead the procedure is modified so that random x_i' are taken from a probability distribution $P(x)$. Then the estimate to a straight average over $f(x_i')$. To apply this technique to the numerical estimate for an integral, one can let $h(x)$ be the probability density for the random variable X so that $\int h(x)dx = 1$. Then

$$\int g(x)dx = \int \frac{g(x)}{h(x)} h(x)dx = \mathbb{E}\left(\frac{g(X)}{h(X)}\right) = \lim_{N \to \infty} \frac{1}{N} \sum_{i=1}^{N} \frac{g(X_i)}{h(X_i)}. \tag{2.62}$$

In practice, to solve Eq. 2.59, a set of gauge configurations U are generated with a probability distribution given by

$$P(U) = \det(M(U))e^{-s_g}. \tag{2.63}$$

The quantity $\det(M(U))$ in Eq. 2.63 is a highly non-local term and as such is very expensive to compute when updating the gauge configurations. M has dimension $NT \times NX \times NY \times NZ \times NSPIN \times NCOL$ (= 491520 for a $8^3 \times 80$ lattice). NT is the number of lattice sites in the temporal direction. NX, NY, NZ are the number of sites in their respective spatial directions. $NSPIN$ = the number of spins and $NCOL$ = the number of colours). For this reason the vast majority of LQCD simulations were, until recently, done in the so called quenched approximation. This involved setting the value of $\det(M(U))$ to be equal to a constant (usually unity). This removed the influence of quarks on the distribution of the gauge fields. Physically this is equivalent to neglecting the sea quarks which means that vacuum polarisation effects are omitted in the quenched approximation. From a formal viewpoint, quenched simulations correspond to introducing an equal mass "ghost" fermion for each light quark, so that disconnected loop contributions from the light quarks and the ghosts exactly cancel. Neglecting the determinant can also lead to the problem that wildly varying or exceptional configurations can be generated, particularly for small quark masses. These exceptional configurations are caused by unphysical poles of valence propagators which occur as eigenmodes of the Wilson-Dirac operator in a quenched simulation. These exceptional configurations can adversely affect the result of any measurement done on an ensemble unless steps are taken to remove these artifacts [53].

A comparison of quenched and unquenched simulations is given in Ref. [54] where unquenched calculations using staggered quarks were shown to agree with the experimental values of a number of standard quantities within statistical and systematic errors of 3% or less.

2.10 Correlation Functions

The two point correlation function is given by

$$C(t,\mathbf{p}) = \sum_{\mathbf{x}} e^{-i\mathbf{p}.\mathbf{x}} \langle \Omega | \mathcal{O}(\mathbf{x},t) \mathcal{O}^{\dagger}(\mathbf{0},0) | \Omega \rangle, \tag{2.64}$$

i.e.

$$C(t,\mathbf{p}) = \sum_{n} \frac{1}{2E_n} \left| \langle \Omega | \mathcal{O} | n \rangle \right|^2 e^{-E_n(p)t}, \tag{2.65}$$

where $\sum_n$ is a sum over the complete set of energy-momentum eigenstates $|n\rangle$.

As t increases, contamination from the higher-order states dies off and only the ground state contributes

$$C(t,\mathbf{p}) \overset{t\to\infty}{\sim} \frac{1}{2E_0} \left| \langle \Omega | \mathcal{O} | n_0 \rangle \right|^2 e^{-E_0(p)t}. \tag{2.66}$$

So to extract the ground state energy, E_0, we need only to look at the correlation function at times large enough that the contribution from higher order states is negligible. For increasing distance in the t direction, the statistical noise becomes large relative to the signal being measured, thus rendering useless any attempt to perform a fit through these points. This can be particularly true for simulations where techniques such as smearing (Sec. 2.13) are used which can increase statistical noise. A method which is frequently employed to estimate ground state energy levels is to use a so-called "effective mass plot". This method follows from the observations that, for a given momentum p,

$$E_0(p) = \lim_{t\to\infty} \ln\left(\frac{Ae^{-E_0 t}}{Ae^{-E_0(t+1)}}\right) = \lim_{t\to\infty} \cosh^{-1}\left(\frac{Ae^{-E_0(t+1)} + Ae^{-E_0(t-1)}}{2Ae^{-E_0 t}}\right), \tag{2.67}$$

or

$$E_0(p) = \lim_{t\to\infty} \ln\left(\frac{C(t,\mathbf{p})}{C(t+1,\mathbf{p})}\right) = \lim_{t\to\infty} \cosh^{-1}\left(\frac{C(t+1,\mathbf{p}) + C(t-1,\mathbf{p})}{2C(t,\mathbf{p})}\right). \tag{2.68}$$

To use either of the formulae in Eq. 2.68 the result is computed for each timeslice and

the value of E_0 is taken to be the value where a "plateau" is found in the resulting effective mass plot. A timeslice is simply a "slice" of time i.e. a particular value of t. An alternate strategy would be to directly fit the function

$$C(t) = A(e^{-E_0 t}), \tag{2.69}$$

to the correlation function. Using this method, the parameter E_0 is extracted directly from the fit to the raw data. In this study, because of periodic boundary conditions the function that is fitted is

$$C(t) = A(e^{-E_0 t} + e^{-E_0(T-t)}), \tag{2.70}$$

where T is the extent of the lattice in the temporal direction.

For the purpose of this study, all effective masses were measured directly from correlation functions. Effective mass plots were only used as a preliminary guide to appropriate fit ranges and as visual aids for comparing fitted values to the data. Where effective mass plots are presented, the plotted values are in terms of $E(t)$, where $E(t)$ is the value obtained at a particular value of t using either the log or inverse cosh method given in Eq. 2.67 above; i.e. not taking the limit $t \to \infty$. Note however that $E_0(p) = \lim_{t\to\infty} E(t)$. All fits were done using a χ^2-minimisation algorithm which is detailed in Sec. 2.11.1 below.

2.10.1 Propagators

From standard field theory, the basic building block for fermionic quantities is the Feynman propagator which is given by the inverse of the Dirac operator

$$S_F(y, j, b; x, i, a) = \left(M^{-1}\right)^{y,j,b}_{x,i,a}. \tag{2.71}$$

A given element of this matrix $(M^{-1})^{y,j,b}_{x,i,a}$ is the amplitude for the propagation of a quark from site x with spin i and colour a to site y with spin j and colour b.

The correlation function in Eq. 2.64 with two operators taking the general form

$$\mathcal{O}^A = \bar{\psi}_1 \Gamma^A \psi_2 \quad , \quad \mathcal{O}^B = \bar{\psi}_1 \Gamma^B \psi_2, \tag{2.72}$$

can be written as

$$\begin{aligned} C(\mathbf{p}, t) &= \sum_{\mathbf{x}} e^{-i\mathbf{p}.\mathbf{x}} \langle 0 | \bar{\psi}_2(\mathbf{x}, t) \Gamma^B \psi_1(\mathbf{x}, t) \bar{\psi}_1(0,0) \Gamma^A \psi_2(0,0) | \rangle 0 \\ &= -\sum_{\mathbf{x}} e^{-i\mathbf{p}.\mathbf{x}} \langle \mathrm{Tr}(S_{F2}(0; \mathbf{x}, t) \Gamma^B (S_{F1}(\mathbf{x}, t; 0) \Gamma^A) \rangle. \end{aligned} \tag{2.73}$$

The hermiticity property $S_F(0; \mathbf{x}, t) = \gamma_5 S_F(\mathbf{x}, t; 0)^\dagger \gamma_5$, can be used to write this expression in terms of $S_f(\mathbf{x}, t; 0)$ only. This in turn means that propagators from the origin to all other points on the lattice are sufficient to calculate the meson correlation function. These are so-called *point propagators*. In practice, one needs to calculate just 12 columns of the matrix M^{-1} given above. Each column corresponds to a spin-colour degree of freedom.

All-to-all propagators

The only physical quantities that may be studied with point propagators are those which can be extracted from hadron two point functions or multi-point functions that can be reduced to connected two point functions. Other quantities such as flavour singlet mesons, condensates and any phenomena which require quark loops necessitate propagators from all points in space to all other points in space. These are so-called *all-to-all* propagators.

Another important point is that the generation of gauge configurations is computationally expensive. By considering only propagators from a single point to all other points, one is discarding a large amount of valuable information which could be extracted from the simulation. The translational invariance of the QCD ground

state means that one should be able to average over all points on the lattice i.e.

$$C(\mathbf{p}, \Delta t) = -\frac{1}{L^3 T} \sum_{\mathbf{x},\mathbf{y},t} e^{-i\mathbf{p}.(\mathbf{x}-\mathbf{y})} \left\langle \mathrm{Tr}(S_{F2}(\mathbf{y}, t; \mathbf{x}, t + \Delta t)\Gamma^B (S_{F2}(\mathbf{x}, t + \Delta t; \mathbf{y}, t)\Gamma^A) \right\rangle. \tag{2.74}$$

The factor of L^3T outside the summation is just the number of points on the lattice. However as mentioned previously in Section 2.9, the matrix M is generally a very large matrix. It is usually far too expensive to compute exactly for typical lattice sizes. A number of stochastic estimation techniques for the inversion of M have been attempted. See for example Ref. [55]. Another technique is the use of a truncated spectral decomposition [56] in which the lowest lying eigenvectors are determined. It is expected that the long-range physics of QCD will be contained in these eigenvectors and as such they will dominate the spectral representations of the mesonic correlator.

This study uses both point and all-to-all propagators. For the all-to-all propagators a general technique which combines the truncated spectral decomposition with a noisy stochastic estimator is used. The stochastic estimator utilises a sub-space thinning technique, *dilution*, to reduce noise. This dilution can be applied to any combination of the space, time, spin, or colour components of the noise vectors used in the stochastic process. Ref. [57] contains a detailed description of the method.

2.11 Numerical techniques

In any numerical simulation there are two sources of error which are always present. There are statistical errors and systematic errors. For LQCD the systematic errors are due to errors in the model being used, finite difference errors (Sec. 2.2.2), finite volume errors (Sec. 2.2.2) and also errors due to the absence of certain modes which are not permitted on the lattice due to the restriction in allowable momenta, $p_n = \frac{2\pi n}{N a_s}$. The statistical errors are a result of the actual simulations. For example, performing a Monte Carlo estimate of an integral involves approximating the integral by a finite sum. As the number of samples being measured approaches infinity, the sum approaches the exact answer. For any finite set of data however, there are

statistical errors associated with the simulation. It is important that a measure of these errors is obtained for each simulation. For a given raw dataset it is possible to simply average over all the values to get a mean value. However, the only possible measure of error would be to use a 68% confidence interval on the raw set. A simple way to increase the statistics is to use the method of "bootstrapping"[58]. Bootstrapping involves creating artificial sets of data from the original single set by re-sampling by random choice with replacement. The method of "jackknifing" can also be used to estimate the standard error on a sample. Like the bootstrap it estimates the variability of a sample by measuring the variability between subsamples. The procedure for the jackknife method for a sample of N measurements is to disregard the j^{th} measurement in a set and then compute m_j as the mean of the set of the $N-1$ measurements. m is the mean of the full set. Then the variance is given by $\sigma_{\text{mean}} = (N-1)\sum_{i=1}^{N} \frac{(m_j - m)^2}{N}$.

2.11.1 χ^2 fitting

In many experiments or simulations it is desirable to construct a model of how a system should behave. Once the model is decided upon, the available data is fitted to the model and the fit parameters and "goodness-of-fit" can be determined. A standard method of obtaining the best fit to a model is to minimise what is known as the *chi-square* or

$$\chi^2 = \sum_{i=1}^{N} \left(\frac{y_i - y_m}{\sigma_i} \right), \tag{2.75}$$

where y_i are the measurements of the experiment and y_m is the expected value due to the model. N is the number of measurements and σ_i is the standard deviation. The index i denotes the different "points" at which the experiment is measured.

If one assumes that each data point y_i has a normally distributed error around the model value y_m then the probability of an individual measurement y_i occurring within an interval Δy around y_m is given by

$$P_i \propto exp\left\{ -\frac{1}{2} \left(\frac{y_i - y_m}{\sigma_i} \right)^2 \right\} \Delta y. \tag{2.76}$$

Thus the probability of a particular set of measurements occurring is given by the product

$$P \propto \prod_{i=1}^{N} exp\left\{-\frac{1}{2}\left(\frac{y_i - y_m}{\sigma_i}\right)^2\right\}\Delta y. \tag{2.77}$$

The best fit to the data occurs by maximising the probability that a set of data can occur given a particular model. This is equivalent to minimising

$$\left\{\sum_{i=1}^{N}\frac{(y_i - y_m)^2}{2\sigma_i}\right\} - N\log\Delta y. \tag{2.78}$$

This is equivalent again to minimising Eq. 2.75 above.

All of the fits done in the course of this thesis were made using the Marquardt-Levenberg algorithm. This method is a combination of two other methods, the inverse-Hessian (or Newton) method and the method of steepest descent. The method of steepest descent suffers from the problem of slow convergence close to the actual minimum. The inverse-Hessian method is liable to fail if the initial guess is far away from the final minimum. Thus the Marquardt-Levenberg algorithm switches smoothly between the two methods, utilising the method of steepest descent when far away from the minimum and then switching to the inverse-Hessian. The method is explained in detail in Ref. [58]. A brief summery is given below.

Method of steepest descent

The method of steepest descent is a very naive method of finding a local minimum. The idea is to start with a point $\mathbf{a}_{\text{current}}$ as an approximation to the minimum of a function $\chi^2(\mathbf{a})$. A new approximation is then given by moving from point $\mathbf{a}_{\text{current}}$ to point $\mathbf{a}_{\text{next}}$ in the direction of steepest descent i.e. $-\nabla\chi^2(\mathbf{a}_{\text{current}})$.

$$\mathbf{a}_{\text{next}} = \mathbf{a}_{\text{current}} - \mu\nabla\chi^2(\mathbf{a}_{\text{current}}), \tag{2.79}$$

where μ is a constant which sets how far down the gradient the step is taken. The choice of μ is very important. μ needs to be small if the curvature of χ^2 is rapidly varying. However a value of μ which is too small means it can take too many iterations

to converge to the local minimum. Methods such as the Davidon-Fletcher-Powell (DFP) [59] and Broyden-Fletcher-Goldfarb-Shanno (BFGS) [60] methods incorporate techniques to find an optimal μ for each step of the procedure.

Inverse Hessian Method

The χ^2 function of M unknown parameters a_i can be approximated to second order by a quadratic form

$$\chi^2(\mathbf{a}) \approx \gamma - \mathbf{d} \cdot \mathbf{a} + \frac{1}{2}\mathbf{a} \cdot \mathbf{D} \cdot \mathbf{a}. \tag{2.80}$$

where $d_i = \frac{\partial \chi^2}{\partial a_i}$, $D_{ij} = \frac{\partial^2 \chi^2}{\partial a_i \partial a_j}$ and γ is a scalar value. If the current χ^2 value is close to the minimum one then the minimising parameters are determined by

$$\mathbf{a}_{\text{min}} = \mathbf{a}_{\text{current}} - \mathbf{D}^{-1} \cdot \left[\nabla \chi^2(\mathbf{a}_{\text{current}})\right]. \tag{2.81}$$

Using the notation that

$$\beta_k \equiv -\frac{1}{2}\frac{\partial \chi^2}{\partial a_k} \alpha_{kl} = \frac{1}{2}\frac{\partial^2 \chi^2}{\partial a_k \partial a_l}, \tag{2.82}$$

the above Eqs 2.79 and 2.81 can be written respectively as

$$\delta a_l = \mu \beta_l, \tag{2.83}$$

$$\sum_{l=1}^{M} \alpha_{kl} \delta a_l = \beta_k, \tag{2.84}$$

where $\delta \mathbf{a} = \mathbf{a}_{\text{next}} - \mathbf{a}_{\text{current}}$. Marquardt's insight was to modify Eq. 2.83 to take some account of the magnitude of the Hessian matrix by writing

$$\lambda \alpha_{ll} \delta a_l = \beta_l, \tag{2.85}$$

and by defining

$$\alpha'_{jj} \equiv \alpha_{jj}(1+\lambda),$$
$$\alpha'_{jk} \equiv \alpha_{jk}(j \neq k). \tag{2.86}$$

The result of this is that Eqs. 2.84 and 2.85 can be combined as

$$\sum_{l=1}^{M} \alpha'_{kl}\delta a_l = \beta_k. \tag{2.87}$$

The net result is that for a large value of λ, Eq. 2.87 becomes identical to Eq. 2.85 but for a very small value of λ it becomes identical to Eq. 2.84. Thus by varying the value of λ it is possible to switch continuously between the two methods. If the χ^2 value of a new estimate of parameters is greater than the χ^2 for the old parameter then the value of λ is increased, so that the algorithm tends more towards the method of steepest descent and the step is repeated. However if the new χ^2 is less than the old χ^2 then the new value is kept and the procedure is repeated, with the value of λ reduced.

Sliding window fits

The use of sliding window fits is a technique which was used extensively during the course of this project. In a sliding window fit, the measured effective mass from a fit is plotted as a function of the lower bound of the fit range. As described above in Sec. 2.10 the ground state effective mass can be extracted from the correlation function for large times. For a small temporal separation, the correlation function still has significant contributions from higher order states. However, too far out along the lattice, the signal can become too noisy to accurately fit. To make a sliding window fit, a maximum timeslice t_{max} is chosen and the minimum timeslice, t_{min} is varied. The measured effective mass for each fit range is determined and the result is plotted with t_{min} along the horizontal axis and the extracted effective mass plotted along the vertical axis. What one is looking for from a fit such as this is stability in the determination of the effective mass over a number of values of t_{min} i.e. a plateau.

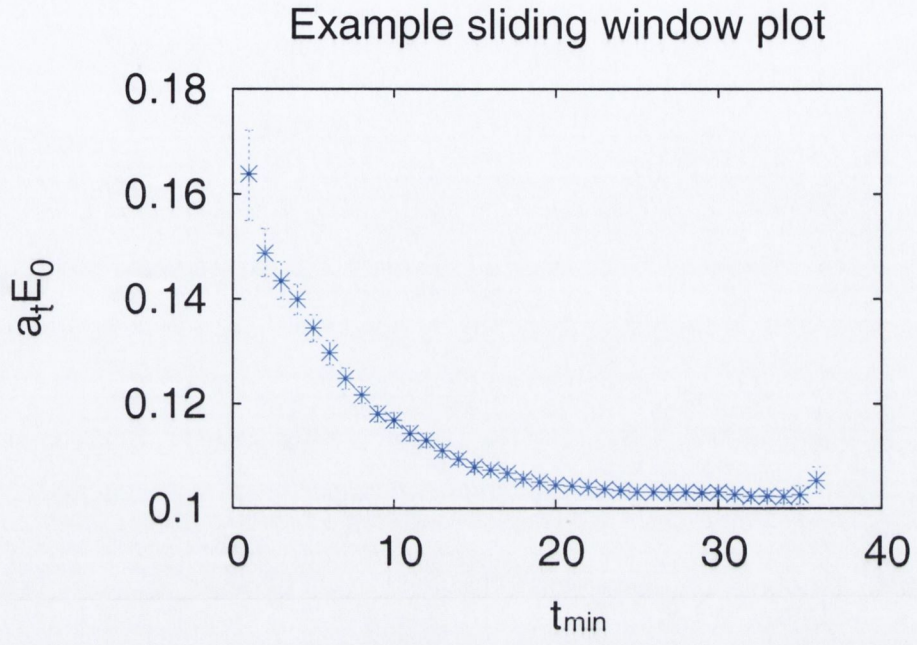

Figure 2-2: An example of a sliding window fit. This fit is taken from RUN 1 for momentum $p^2 = 0$. For further details see Sec 3. For this fit, $t_{\max} = 40$ and the x-axis of the plot corresponds to the value for $t_{\min}$. The y-axis corresponds to the measured value of $a_t E_0$ obtained when fitting in the range $[t_{\min}, 40]$. The x-axis is given in units of a_t

.

Such a fit should also be considered in conjunction with the respective $\chi^2/N_{d.f}$ values to maximise the quality of any extracted results. An example of a sliding window fit is shown in Fig. 2-2. In practice for this study, $t_{\max}$ was set to be at the midpoint of the lattice.

2.12 Generation of Configurations

All of the configurations used in the course of this project were generated using the *hybrid Monte Carlo* (HMC) method. The hybrid Monte Carlo method is a combination of Monte Carlo techniques with molecular dynamics (MD) methods. Monte Carlo methods usually only involve local updates and have low acceptance rates for multiple attempted updates at a single step. MD methods involve global updates but the scheme is prone to instabilities due to the finite time-step. HMC allows for

global updates but does not suffer from the instabilities of MD methods.

2.13 Smearing

Smearing is a technique which is used to enhance the measurements made in a simulation. In particular it can greatly reduce the ultraviolet divergences due to tadpole diagrams, (See Sec. 2.6.2). Smearing can be done on both quark and gluon fields. The two types of gauge smearing used in the course of this project are discussed below. Other approaches include the hypercubic "fat link" smearing transformation [61]. The effects of different smearing procedures on simulations using a range of different actions can be found in Ref. [62]

2.13.1 Gluon Smearing

Link smearing [63] refers to the procedure whereby a link is substituted by itself plus a weighted sum of neighbouring spatial plaquettes.

$$U_i \rightarrow U_i + \epsilon \sum_{\eta=+1,-1} \sum_{j \neq i} P_{ij}^{\eta}, \tag{2.88}$$

where the RHS of Eq. 2.88 must be projected back onto the $SU(3)$ group since the combination of links is not itself an element of $SU(3)$. This procedure is then repeated n times to obtain the final smeared link variables. The purpose of smearing is to try to eliminate or reduce unphysical short-distance fluctuations present on the lattice. Smearing leads to a stronger signal but introduces a strong distortion at short distances from the source.

The projection onto $SU(3)$ is neither analytic nor unique and must be carefully defined in order to preserve all symmetry properties of the link variables. The projection of a matrix V into $SU(3)$ is often taken to be the matrix $U \in SU(3)$ which maximises $\mathrm{ReTr}(UV^{\dagger})$. Alternatively it can be defined by $U = V(V^{\dagger}V)^{-\frac{1}{2}}\det(V^{-1}V^{\dagger})^{\frac{1}{6}}$.

Stout Links

An analytic method of smearing the link variables was given in Ref. [64]. The resulting variables from this method are called "stout links". The method consists of creating the Hermitian and traceless matrix $Q_\mu(x)$ defined by,

$$Q_\mu(x) = \frac{i}{2}\left(\Omega_\mu^\dagger(x) - \Omega_\mu(x)\right) - \frac{i}{2N}\mathrm{Tr}\left(\Omega_\mu^\dagger - \Omega_\mu(x)\right), \tag{2.89}$$

where

$$\Omega_\mu(x) = \left[\sum_{\nu\neq\mu}\rho_{\mu\nu}\left(U_\nu(x)U_\mu(x+\hat{\nu})U_\nu^\dagger(x+\hat{\mu}) + U_\nu^\dagger(x-\hat{\nu})U_\mu(x-\hat{\nu})U_\nu(x-\hat{\nu}+\hat{\mu})\right)\right]U_\mu^\dagger, \tag{2.90}$$

and $\rho_{\mu\nu}$ are the weighting parameters. The smearing procedure is then defined by

$$U_\mu^{(n+1)}(x) = e^{(iQ_\mu^{(n)}(x))}U_\mu^{(n)}(x). \tag{2.91}$$

As $Q_\mu(x)$ is Hermitian and traceless, $e^{(iQ_\mu^{(n)}(x))} \in SU(N)$ which means that $U_\mu^{(n+1)}(x) \in SU(N)$ and thus there is no need to project the final link variables back into $SU(N)$. Ref. [64] showed that results from using "stout links" agreed with results using standard smearing procedures but that this method was more sensitive to the weighting parameters.

2.13.2 Quark Smearing

Quark smearing is a procedure which essentially replaces point-like quark-sources on the lattice with a more realistic quark source with finite size. Smeared operators constructed from these more realistic sources increase the overlap with the lower energy states and as such are particularly useful in determining ground state energies. In order to do this, the short-wavelength, high-momentum modes are dampened out. A simple way of doing this is to apply a gauge-covariant scheme in which the smeared quark field at a given site is replaced by a Gaussian weighted average of the

surrounding sites on the same time slice [48]

$$\tilde{\psi}(x) \sim \int d^3r e^{-r^2/(4\sigma_s^2)} \psi(\mathbf{x}+\mathbf{r}) \sim e^{\sigma_s^2 \Delta/4} \psi(\mathbf{x}). \tag{2.92}$$

For the lattice this expression is approximated by

$$\tilde{\psi}(x) = \left(1 + \frac{\sigma_s^2}{4n_\sigma}\Delta\right)^{n_\sigma} \psi(x), \tag{2.93}$$

where Δ is the three-dimensional gauge covariant laplacian

$$\Delta\psi(x) = \sum_{n=\pm1,\pm2,\pm3} \left(U_n(x)\psi(x+\hat{n}) - \psi(x)\right). \tag{2.94}$$

σ_s is the smearing radius and n_σ denotes the number of times the smearing procedure is iterated.

2.14 Other formulations of the quark action.

Although Wilson fermions were exclusively used in this thesis, a short synopsis of other fermion discretisations are given here also.

2.14.1 No-go theorem

The "No-Go" theorem was first described by Nielsen and Ninomiya [65]. This theorem stated that given the three assumptions

- Locality of interaction, i.e the Hamiltonian satisfies $H(x-y) \to 0$ as $|x-y| \to \infty$
- Translational invariance on the lattice
- Hermiticity of the $N \times N$ matrix Hamiltonian H

then the appearance of equally many right-handed and left-handed species of Weyl particles with given quantum numbers in the continuum limit is an unavoidable consequence of a lattice theory. The conclusion of this theorem was that the weak interaction cannot be put on the lattice.

A consequence of that theorem is that it is not possible, in strong interaction models to solve the species doubling problem of Dirac fermions on a lattice in a chirally invariant way. In the Weinberg-Salam electroweak model mass terms are due to spontaneously broken gauge symmetries of the weak interaction. A Dirac particle can be thought of as a left-handed Weyl particle pairing up with a right-handed particle with a mass term in the Hamiltonian in order to cause a transition between the two. Karsten and Smit [66] gave a weaker version of this theorem which showed that the absence of doublers with full chiral symmetry on the lattice was inconsistent with the Adler-Bell-Jackiw Anomaly and that the appearance of the doublers was to compensate for the strict chiral symmetry imposed by lattice regularisation.

The Nielsen Ninomiya theorem can be expressed in a form more suitable for lattice QCD [67, 68]. Considering the free field action,

$$S_F = a^4 \sum_x \bar{\psi}(x) D \psi(x), \tag{2.95}$$

where as usual, a is the lattice spacing and D is the lattice Dirac operator. D is assumed to be invariant under translations so that

$$D e^{ipx} u = \tilde{D}(p) e^{ipx} u \tag{2.96}$$

The theorem now states that the following properties cannot hold simultaneously.

- $\tilde{D}(p)$ is an analytic periodic function of the momenta p_μ with period $2\pi/a$.
- For momenta far below the cutoff π/a, $\tilde{D}(p) = i\gamma_\mu p_\mu$ up to terms of order ap^2.
- $\tilde{D}(p)$ is invertible at all non-zero momenta (mod $2\pi/a$).
- D anti-commutes with γ_5.

Note that whereas Wilson and staggered fermions suppress doublers with explicit breaking of chiral symmetry, the use of a random lattice does so by spontaneous chiral symmetry breaking [69].

2.14.2 Staggered Fermions

Kogut-Susskind or Staggered Fermions [70] were developed as an attempt to overcome the fermion doubling problem detailed above. The basic idea behind staggered fermions is to double the effective lattice spacing and reduce the Brillioun Zone by a factor of $\frac{1}{2}$. This is achieved in practice by distributing the fermionic degrees of freedom over the lattice. The naive continuum limit of any action used must reduce to the continuum action. In constructing a lattice action for staggered fermions it turns out that the spin and flavour indices must become mixed. Staggered fermions do however preserve a remnant U(1) chiral symmetry. The extra species present due to doubling are reduced from 16 down to "4 tastes" for staggered fermions. In order to recover a theory with a single fermion, the usual procedure is to take the fourth root of the fermion determinant. This however leads to the problem that the resulting action is non-local. The issue of locality with staggered fermions is discussed in Ref. [71]. Non-local theories are unphysical and lack unitarity. The rooted action is not invalid as long as the non-local terms are irrelevant and scale away in the continuum limit. Ref. [72] showed that this was the case in the 2-dimensional Schwinger model and proved that the rooting procedure was justified for that case. Lattice QCD with unrooted staggered fermions does have the correct continuum limit (however with the four degenerate tastes mentioned above). Staggered fermions can be calculated much more rapidly than Wilson fermions and as such, it is possible to simulate at much lower bare quark mass values.

2.14.3 Ginsparg-Wilson Relation

For an action to be chiral, its Dirac operator D must anti-commute with the chirality operator γ_5.

$$\{D, \gamma_5\} = 0. \tag{2.97}$$

Ginsparg and Wilson introduced a modified lattice form of this relation called the

Ginsparg-Wilson relation [73]

$$\{D, \gamma_5\} = 2(D\gamma_5 RD), \tag{2.98}$$

where R is a local term with $\{R, \gamma_5\} \neq 0$. A fermion obeying the Ginsparg-Wilson relation will have an exact chiral symmetry at finite lattice spacing. However, GW fermions may not exhibit the correct scaling behaviour. There are so-called "perfect actions", (See Sec. 2.6.2), which show a scaling identical to the continuum at any lattice spacing but their construction is almost as difficult as solving the model analytically. GW fermions cannot have the property of "ultra-locality". GW fermion couplings will decay exponentially but they cannot drop to zero beyond a finite number of lattice spacings [74].

2.14.4 Domain Wall Fermions

Kaplan [75] showed that a lattice theory of massive interacting fermions in $2n+1$ dimensions could be used to simulate the behaviour of massless chiral fermions in $2n$ dimensions if the fermion mass had a step function shape in the extra dimension. The Nielsen Ninomiya theorem is satisfied in the $2n+1$ theory as a chiral fermion living on a certain domain wall has a corresponding chiral fermion of opposite chirality living on a domain wall of opposite orientation. Following on from the explanation for doublers for Wilson fermions, Sec. 2.5.1, there are 2^{2n+1} massless modes in the continuum. The addition of a Wilson term removes all but one of the 2^{2n+1} zero modes bound to the domain in the continuum limit with only a single positive chirality mode remaining. The currents of the $2n+1$ dimensional lattice are exactly conserved but there is an anomalous current violation in the $2n$ dimensional effective theory due to charge flowing in from the extra dimension. However the addition of the extra dimension greatly increases the computational costs involved in using domain wall fermions.

2.14.5 Overlap Fermions

Narayanan and Neuberger [76] showed that the effect of the massless chiral fermion can be represented as an overlap of two fermionic states. A simpler formula for the effective action was derived in [77], [78]. The overlap operator can be written as

$$D_0 = \frac{1+V}{2}, \tag{2.99}$$

with

$$V = \frac{D_W}{\sqrt{D_W^\dagger D_W}} = \gamma_5 \text{sign}(H). \tag{2.100}$$

and D_W is the Wilson lattice operator and H is the Hamiltonian. This formulation does not contain an explicit fifth dimension, however the addition of the sign operator makes the simulation procedure difficult.

2.14.6 Twisted Mass Fermions

Simulations in the quenched approximation can lead to so-called exceptional configurations. These are due to large fluctuations which arise from the contribution of a small eigenvalue to the fermionic correlator which is not balanced due to the omission of the fermionic determinant. Exceptional configurations are particularly problematic for simulations at smaller quark masses, particularly below the strange quark mass. A method to prevent exceptional configurations is the use of twisted mass fermions. For this approach [79], a chirally twisted mass term is added to the Dirac operator

$$D_{tw} = D + i\mu\gamma^5\tau^3,$$

where the Pauli matrix τ^3 acts in flavour space. This Dirac operator is protected from zero modes for any finite value of μ as

$$\det D_{tw} = \det[D^\dagger D + \mu^2] > 0,$$

which protects against exceptional configurations.

Chapter 3

Non-perturbative determination of action parameters

The use of an anisotropic lattice introduces new parameters into the actions, ξ_q being introduced as the quark anisotropy parameter in the quark action, Eq. 2.56 and ξ_g as the gluon anisotropy parameter into the gluon action, Eq. 2.53. At tree level, these anisotropy parameters are given by the ratio of the lattice spacing in the spatial direction to the lattice spacing in the temporal direction i.e. $\xi_q = \frac{a_s}{a_t}$ for the quark sector and similarly for ξ_g. In practice the bare input parameters are renormalised in a simulation and therefore the measured physical quantity will not be equal to the input parameters. As such, the input parameters must in general be tuned to give the desired target renormalised value. In the case of the anisotropy, the determination of the renormalised anisotropy from both the quark and gluon sector should correspond with the target anisotropy.

As discussed in Sec. 2.9 the technique of importance sampling applied to QCD simulations leads to background configurations being generated with probability distribution

$$P(U) = \det(M(U))e^{-S_g}. \tag{3.1}$$

The fermion matrix M contains all information relating to the quark sector. As mentioned in Sec. 2.9 the so called "quenched" approximation involves setting the value $\det M$ equal to a constant. Thus, changing the value of ξ_q has no effect on the

generation of the gauge configurations within the quenched approximation. On the other hand, S_g contains all the information from the gluon sector. Changing the input value ξ_g affects the generation of configurations for both the quenched and dynamical (unquenched) cases. For the quenched case then it is a simple matter to first tune an input value ξ_g and generate the required configurations. The value of ξ_q can then be independently tuned to restore Lorentz invariance after the configurations have been generated. In the unquenched or dynamical case however, $\det M$ is taken into account in the generation of the gauge configurations and changing ξ_q will necessitate the regeneration of the configurations according to the new distribution. If ξ_g is tuned to the required renormalised value and then an attempt is made to tune ξ_q, the gauge configurations must be regenerated to take into account the new ξ_q. The previous value for ξ_g is invalid for the new set of configurations and must be measured again. In order to solve this problem the two parameters ξ_g and ξ_q must be tuned simultaneously.

3.1 Quenched Case

The tuning procedure for the quenched case is described in detail in earlier work [52]. To summarise, a target renormalised anisotropy value of 6 was chosen. ξ_g was first tuned to the required target anisotropy and ξ_q was subsequently tuned. The main results of the paper were that the tuning of the input anisotropies was a straightforward procedure and that the mass dependence of the tuned value was small across a large range of masses varying from the mass of the strange quark to the charmed quark.

3.2 Dynamical Case

The dynamical gauge configurations used in the course of this study were generated with two quark flavours. As mentioned above, in the case of a dynamical simulation, ξ_q and ξ_q must be simultaneously tuned [80]. In order to do this, the dependence of the renormalised values on the input values for any simulation was taken to be linear

as a first approximation. Writing

$$\xi_q^r = A\xi_q^0 + B\xi_g^0 + C, \tag{3.2}$$

$$\xi_g^r = D\xi_q^0 + E\xi_g^0 + F. \tag{3.3}$$

(ξ_q^r, ξ_g^r) are the renormalised values measured from the simulation. Three sets of input parameters (ξ_g^0, ξ_q^0) are needed to solve these equations for A, B, C, D, E, F. Once these variables are known it is simply a matter of solving the simultaneous equations

$$\xi^t - C = A\xi_q^* + B\xi_g^*, \tag{3.4}$$

$$\xi^t - F = D\xi_q^* + E\xi_g, \tag{3.5}$$

for ξ_q^* and ξ_g^*, the tuned input anisotropies. ξ^t is the target anisotropy.

3.3 Measuring output anisotropies

The renormalised anisotropy measurements must be determined by a physical probe of the system after the simulation. Two different methods are presented here, one for the gluon sector and one for the quark sector. The purpose of this tuning is that one should be able to determine what input values ξ_q^0 and ξ_g^0 should be used so that both determinations coincide with the target anisotropy value.

3.3.1 Measuring ξ_g^r

The renormalised gluon anisotropy ξ_g^r is determined by the method of "sideways potential" [49, 81]. The static source propagation is chosen to be along a coarse direction and interquark potentials are extracted from Wilson loops in both the fine and a coarse direction via the relations,

$$a_s V_s(\mathbf{x}, z) = \ln\left(\frac{W_{ss}(\mathbf{x}, z)}{W_{ss}(\mathbf{x}, z+1)}\right), \tag{3.6}$$

$$a_s V_t(\mathbf{t}, z) = \ln\left(\frac{W_{ts}(t, z)}{W_{ts}(t, z+1)}\right), \tag{3.7}$$

where V_s is the static interquark potential, $W_{ss}(\mathbf{x}, z)$ and $W_{ts}(\mathbf{t}, z)$ are Wilson loops with the subscripts s and t referring to spatial and temporal lattice directions respectively. $\mathbf{t}$ is the fine direction and $\mathbf{x}, \mathbf{z}$ are two coarse directions. The potential $V(|\mathbf{x}|)$ is then extracted from

$$\lim_{z\to\infty} V_s(\mathbf{x}, z) \to V_s(|\mathbf{x}|), \tag{3.8}$$

$$\lim_{z\to\infty} V_t(\mathbf{t}, z) \to V_t(|\mathbf{t}|). \tag{3.9}$$

The static interquark potential should be the same over the same physical distance. In practice, for a target anisotropy of 6, the fine direction is blocked so that the product of 6 links in the fine direction is taken to be equivalent to one link in a coarse direction. V_s and V_t should give the same result if the anisotropy is tuned correctly. For a given input anisotropy ξ_g^0 and target anisotropy ξ^t the mismatch parameter $c_g = V_s(x)/V_t(t/\xi)$ can be determined. $V(x)$ can be assumed to be approximated by the Cornell potential $V(x) = -\frac{\alpha}{x} + \sigma x$. If x is in the régime where the potential is nearly linear, the mismatch parameter is approximately related to the actual gauge anisotropy, $c_g \approx \xi_g/\xi$.

3.3.2 Measuring ξ_q^r

The value of ξ_q^r was measured from the pseudoscalar dispersion relation. On the anisotropic lattice

$$E_0(p)^2 = E_0(0)^2 + \frac{4\pi^2}{L^2}\frac{1}{\xi_q} n^2 + \mathcal{O}(p^4), \tag{3.10}$$

with $\vec{p} = \frac{2\pi n}{La_s}\hat{n}$, L is the length of the lattice. $E_0(p)$ is the ground state energy for momentum p. Thus for low momenta ξ_q can be determined from the inverse of the slope of the dispersion relation. Fig. 3-20 shows typical dispersion relations for

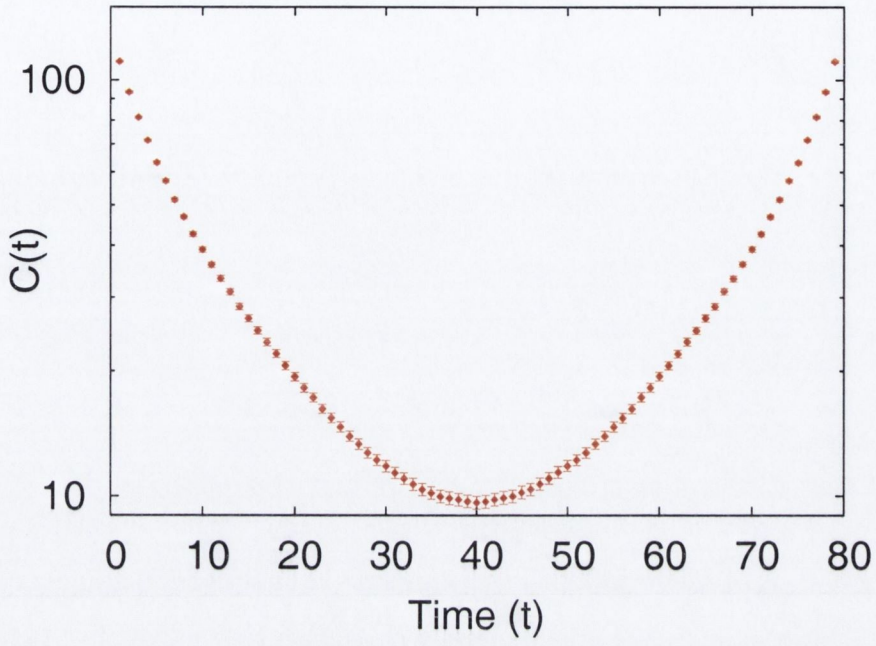

Figure 3-1: This plot shows a typical correlation function for the pseudoscalar with momentum $p^2 = 0$ on a $8^3 \times 80$ lattice. All-to-all propagators were used. The data were generated by averaging over correlation functions measured on a set of 250 configurations. The error bars are given by a 68% confidence interval over the measured values. Note that the y-axis of this plot is shown on a log scale and the x-axis is presented in units of a_t.

the ensembles used in this study. The process first involves extracting the effective pseudoscalar mass from the decay of correlation functions; from Sec. 2.10, $C(t) = \sum_n C_n(e^{-tE_n} + e^{-(T-t)E_n})$. A typical correlation function can be seen at Fig. 3-1. For reasons explained previously, the fit must be performed far enough across the lattice so that there is no contribution from the higher order states. However as can be seen from Fig. 3-1, the correlation function can become noisy further out along the lattice. In order to increase the statistics, the correlation function is "folded" before the analysis is performed. In other words, $C(t)$ and $C(T-t)$ are averaged. The resulting energies were used to determine the energy-momentum dispersion relations.

Run	1	2	3	4	5	6	7
β	1.51	1.528	1.514	1.544	1.522	1.514	1.508
ξ_q^0	6.0	7.5	7.5	8.72	8.83	7.52	7.43
ξ_g^0	8.0	7.0	8.0	6.65	7.44	8.06	8.42

Table 3.1: Input parameters for the five dynamical simulations performed in this tuning procedure. The bare quark mass is $a_t m_q = -0.057$ for all runs.

3.4 Simulation Details

This study was carried out on $8^3 \times 48$ and $8^3 \times 80$ anisotropic lattices with a spatial lattice spacing $a_s \approx 0.2$fm and a target anisotropy $\xi = 6$. The bare sea quark mass was set to $a_t m_q = -0.057$ in all runs. This particular bare input parameter leads to quarks with mass of the order of the strange quark. A set of 250 gauge configurations, distributed across ten independent Markov chains, was generated for each set of input parameters (ξ_g^0,ξ_q^0). See Table 3.1. Valence quark propagators were generated with the same mass as the sea quarks.

To determine the statistical uncertainties, 1000 bootstrapped sets of configurations were taken and analysis was done on these bootstrapped sets. A common bootstrap ensemble was used for all measurements. This was necessary to ensure the consistency of the tuning procedure. Both point and all-to-all propagators [57] were used. The ground state energy E_0 was determined for a range of momenta, $n^2 \in \{0, 1, 2, 3, 4, 5, 6, 9, 12\}$, where $p_n = \frac{2\pi n}{La_s}$ and equivalent momentum values were averaged over. The two-point correlator data were modelled with single exponentials and a χ^2-minimisation was used to determine the best-fit ground state. These resulting values for E_0 were used to generate an energy-momentum dispersion relation.

When more than three simulation points were available a plane was defined using a constrained-χ^2 fit.

All observables were estimated using the Monte Carlo method. An ensemble of 250 gauge field configurations divided across 10 Markov chains was generated using the Hybrid Monte Carlo (HMC) algorithm [82].

Stout-link smearing [64] was used for the gauge fields in the fermion matrix. Two stoutening iterations were used, with a parameter $\rho = 0.22$. This was fixed for

all simulations, and chosen to approximately maximise the expectation value of the spatial plaquette on the stout links.

3.4.1 Simulation times

$8^3 \times 48$ lattices

The first $8^3 \times 48$ gauge configurations were generated for a glueball project on a cluster in Carnegie Mellon University and took approximately 6500 CPU hours to generate a set of 250 configurations. The point propagators were initially generated on single Pentium 4 workstations and took approximately two to three weeks to generate on a single machine. The point propagators were generated for 24 different momenta given in Table A.1.1. $8^3 \times 48$ lattices for Runs 3, 4, 5 were generated using 10 separate Monte Carlo chains on the TCHPC "Moloch" cluster. Sec. A.1 contains the technical specifications of this cluster. Approximately 4000 CPU hours were needed to generate 250 configurations on this cluster.

$8^3 \times 80$ lattices

The $8^3 \times 80$ configurations were generated on the TCHPC "IITAC" cluster, see Sec. A.1 for technical specifications. Approximately 6000 CPU hours were needed to generate 250 configurations on "IITAC". It took a total of 240 CPU hours to generate the point propagators for 24 momenta for each set of configurations.Approximately 4800 CPU hours were needed to construct correlation functions from all-to-all propagators using time and colour dilution for 41 momenta on the 250 configurations using only the "IITAC" cluster (19 CPU hrs per config) and approximately 7000 CPU hours using only the "Moloch" cluster (28 CPU hrs per config). Using only time dilution took under approximately 1250 CPU hours to generate the required noise vectors using the faster IITAC cluster. It took approximately 2200 CPU hours using the Moloch cluster.

3.5 Results

The study was initially attempted using point propagators on lattices with 8 sites in each of the spatial directions and 48 sites in the temporal direction. Three initial sets of input parameters were chosen in the region in which it was believed that the tuned point would lie. These input parameters, numbered 1, 2,and 3, are given in Table 3.1.

3.5.1 $8^3 \times 48$ lattice

Some preliminary results using point propagators on $8^3 \times 48$ lattices were presented in Ref. [83].

ξ_g

The gluon anisotropy is determined from the static quark potential at a selected distance R and time T. It is important to choose values of R and T where the potential is well determined and the value obtained for $c_g = \frac{V_s(x)}{V_t(t/\xi)}$ is stable with respect to small variations in R and T. The same values of R and T must then be used for all runs in order to have a consistent procedure.

c_g was measured for all of the lattices for different separations in the temporal and spatial directions. Figs. 3-2, 3-3 shows the values for $a_s V_s(\mathbf{x}, z)$ and $a_s V_t(\mathbf{t}, z)$ measured for spatial separations $R = 3, 4$ for Run 1. The error bars on these plots are generated using a 68% confidence interval over 1000 bootstrapped sets generated from the initial 250 background gauge configurations. The same bootstrapping order was maintained for computing c_g as for computing ξ_q in order to preserve consistency. $(T, R) = (2, 3)$ were chosen as the parameters used in the measurement of c_g for the final analysis.

ξ_q

Point propagators were measured with sources at four different timeslices and the resulting data were averaged. Equivalent momenta were also averaged over, for ex-

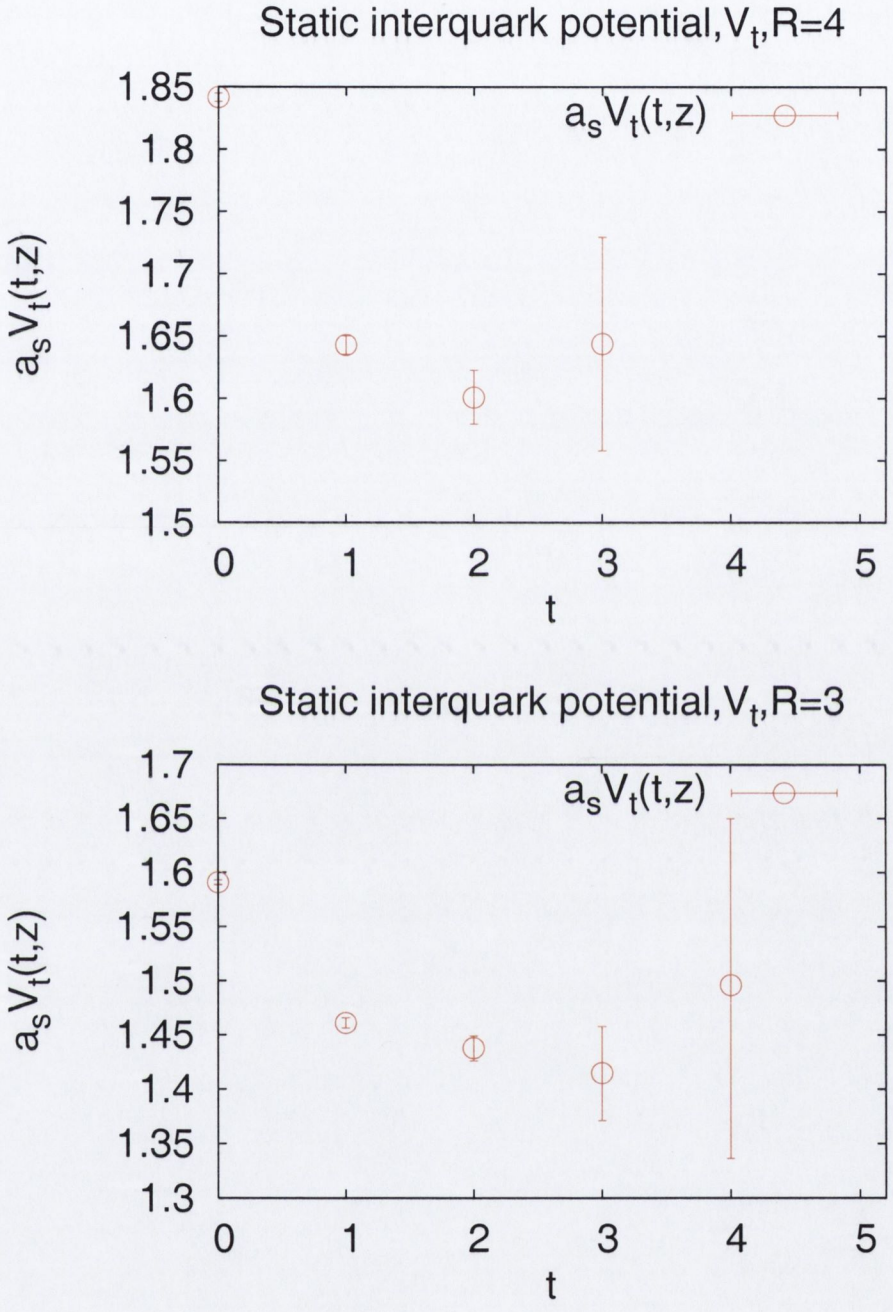

Figure 3-2: These plots show the measured static quark inter-potential for Run 1 on an $8^3 \times 48$ lattice. These plots are from Wilson loops measured in the (t, z) direction. The top plot is for a spatial separation $R = 4$ and the bottom plot is for separation $R = 3$. The horizontal axis shows the temporal spacing in blocked lattice units i.e. in units of $6a_t \approx a_s$.

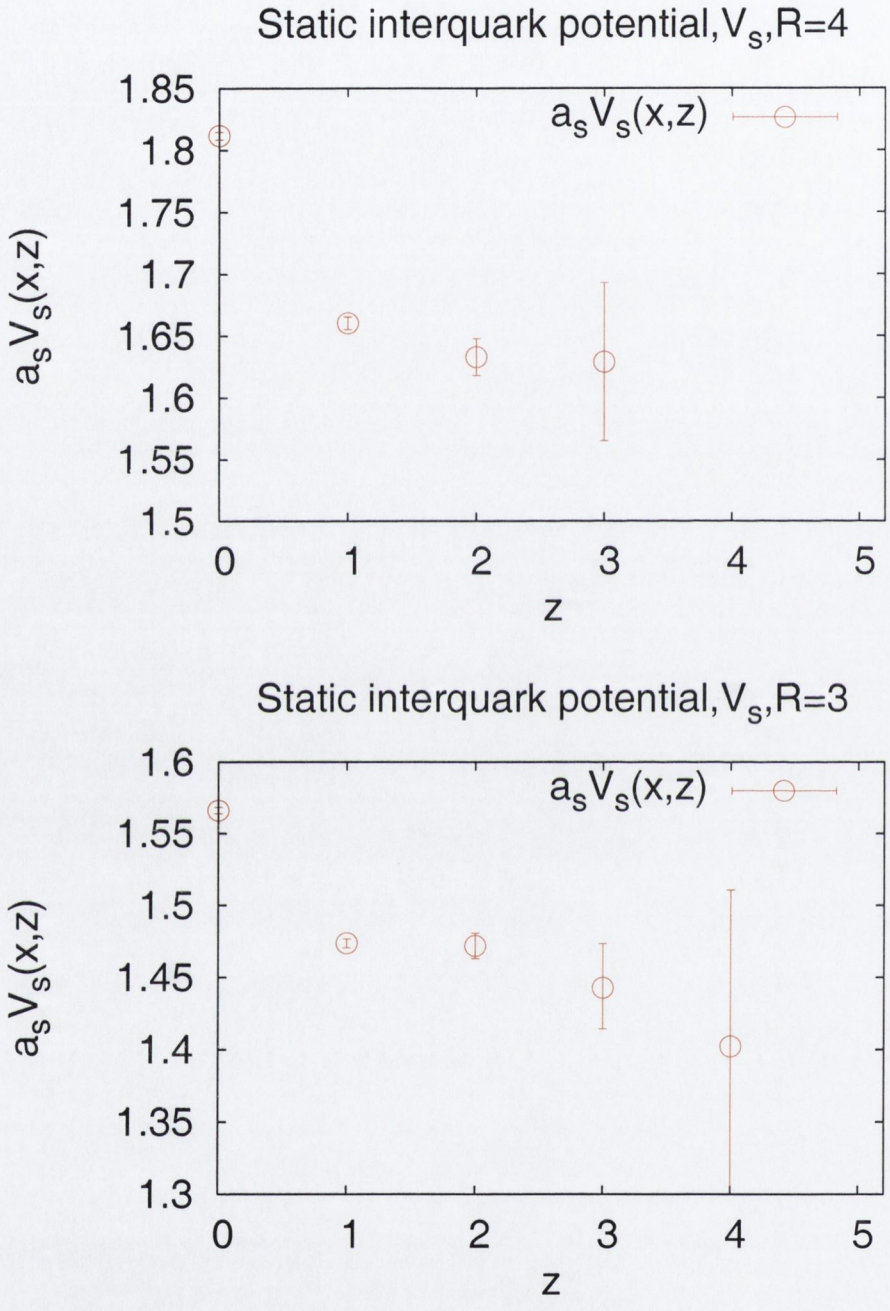

Figure 3-3: These plots show the measured static quark inter-potential for Run 1 on an $8^3 \times 48$ lattice. These two plots are from Wilson loops measured in the (x, z) direction. The top plots is for a spatial separation $R = 4$ and the bottom plot is for separation $R = 3$. Again the horizontal axis shows the spacing in lattice units a_s.

ample $\{0,0,1\},\{0,1,0\},\{1,0,0\}$. The quark fields were not smeared for the initial measurements. The quark anisotropy was measured from the pseudoscalar dispersion as described in Sec. 3.3.2. Measurements of $a_t E_0$ were taken for Run 1 for momenta $n^2 = 0,1,2,3,4,5,6,9,12$. The resulting dispersion relation can be seen in Fig. 3-5. This procedure was repeated for Runs 2 and 3. The dispersion relations from Run 2 and Run 3 can be seen in Fig. 3-6. However the data for Run 3 was extremely noisy and any attempts at a straight line fit resulted in large χ^2 values. It was decided to repeat the procedure using smeared quark fields in an attempt to reduce contamination from higher order states.

Smeared vs Unsmeared

The smearing procedure is described above in Sec. 2.13.2. The quark fields were smeared with five iterations using a weighting of 0.1 in each spatial direction. The effect of the smearing procedure can be seen in Fig. 3-4 which compares an effective mass plot from unsmeared quark fields with one from smeared quark fields. Fig. 3-7 also shows the difference in the form of a sliding window fit for momentum $n^2 = 3$. This plot also shows the effect of smearing on the resulting $\chi^2/N_{d.f}$ values. Some of the lower $\chi^2/N_{d.f}$ for the smeared data can be attributed to the extra noise in the correlation functions from the smeared fields. An attempt was made to fit over an increased number of timeslices by fitting the correlation function to a double exponential rather than a single exponential function, $C(t) = Ae^{-E_0 t} + Be^{-E_1 t} + Ae^{-E_0(T-t)} + Be^{-E_1(T-t)}$. However it was found that the resulting fits were very sensitive to the choice of fit range and the number of timeslices that could be fitted over to give a reasonable χ^2 value was not much greater than for the single exponential fit. For example, an attempt to fit momentum $p^2 = 0$ on Run 1 with a double exponential fit between timeslices $[8,14]$ gave a value of $a_t E_0 = 0.069 \pm 0.006$ with a $\chi^2/N_{d.f} = 0.86$ whereas a fit between timeslices $[9,15]$ gave a value of $a_t E_0 = 0.522 \pm 0.005$ and a $\chi^2/N_{d.f} = 0.44$. These fits further out the lattice were not consistent with a visual inspection of the effective mass plot. When the fitted parameters were substituted back into the model for $C(t)$, the result differed significantly from the

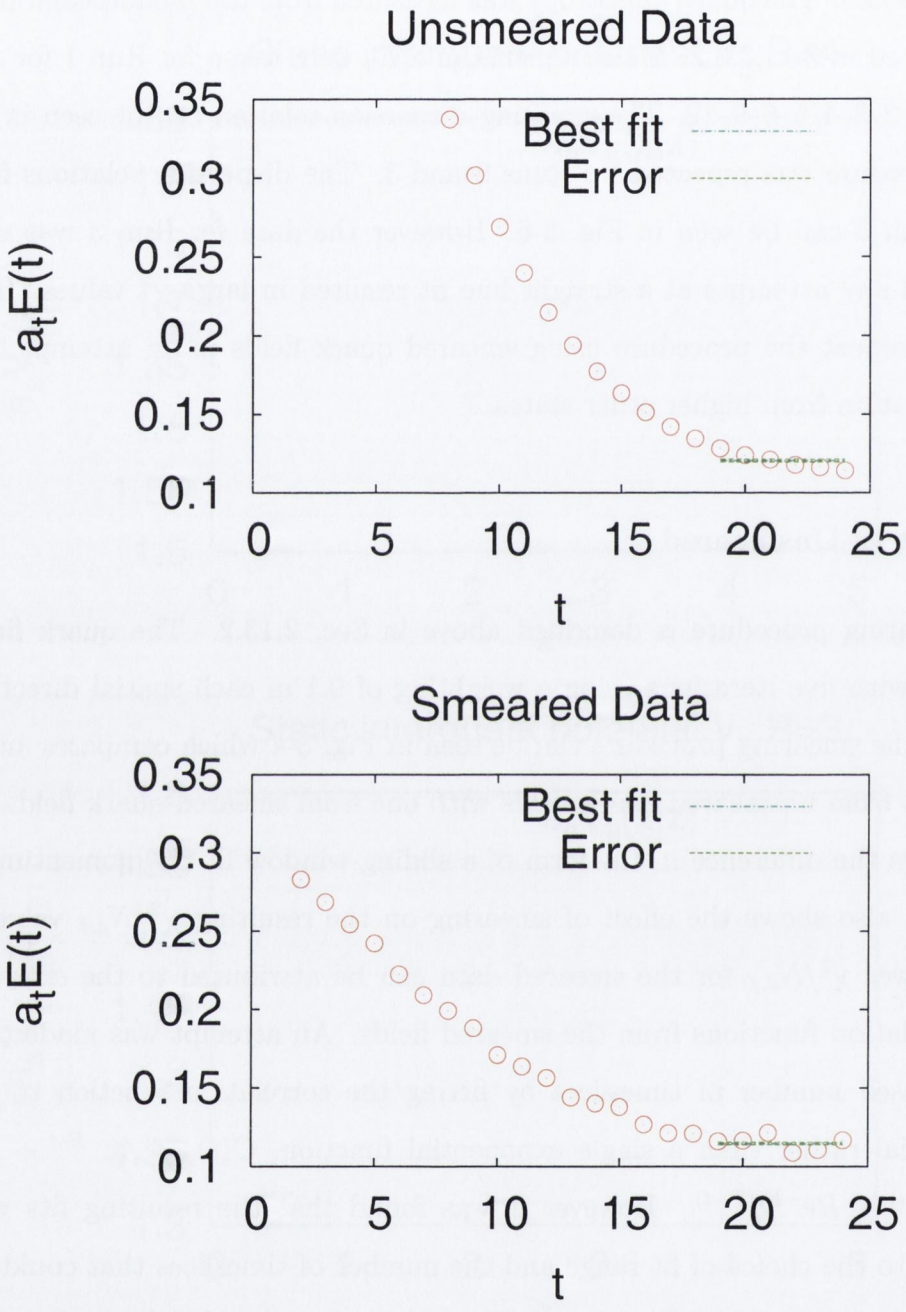

Figure 3-4: These plots show the effects of smearing on effective mass plots. A fit was attempted on both smeared and raw data sets between timeslices 19 and 24. The results for the smeared data was 0.114 ± 0.001 with a large $\chi^2/N_{d.f} \approx 12$.For the unsmeared data the fit was 0.121 ± 0.001 with a $\chi^2/N_{d.f} \approx 3$. Both these fits were attempted on $8^3 \times 48$ lattices for momentum $n^2 = 0$ and with input values corresponding to Run 1 in Table 3.1. The horizontal axis is given in units of a_t.

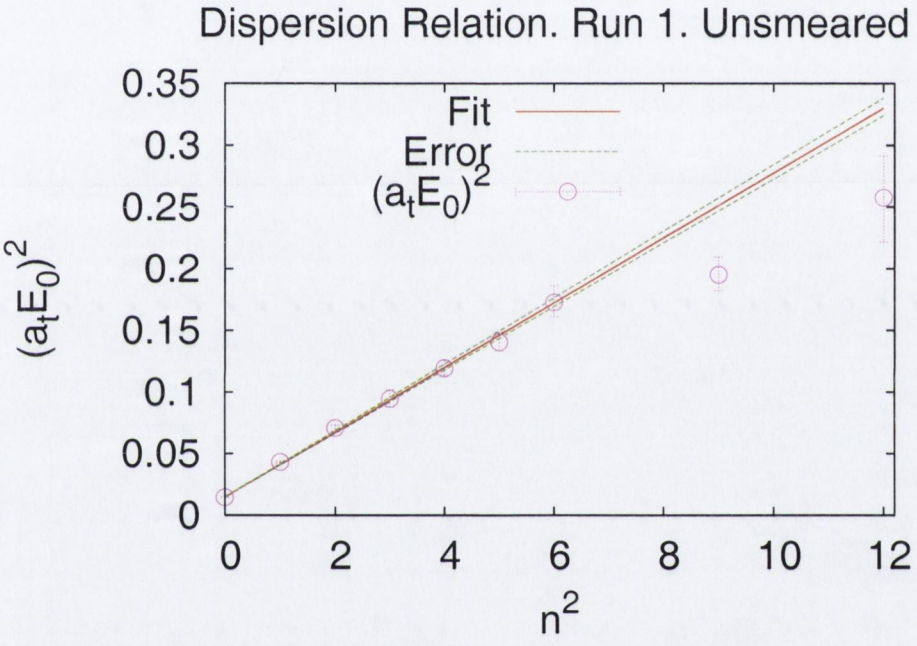

Figure 3-5: This plot is an initial attempt to measure ξ_q for Run 1. The quark fields were unsmeared and momenta to $n^2 = 12$ were measured. A straight line fit was attempted to all of the points. Note that this plot was only a preliminary plot and later fits were performed to only the first three momenta. The result from this particular fit was a value of $\xi = 4.84 \pm 0.06$ with a $\chi^2/N_{d.f} = 4.14$.

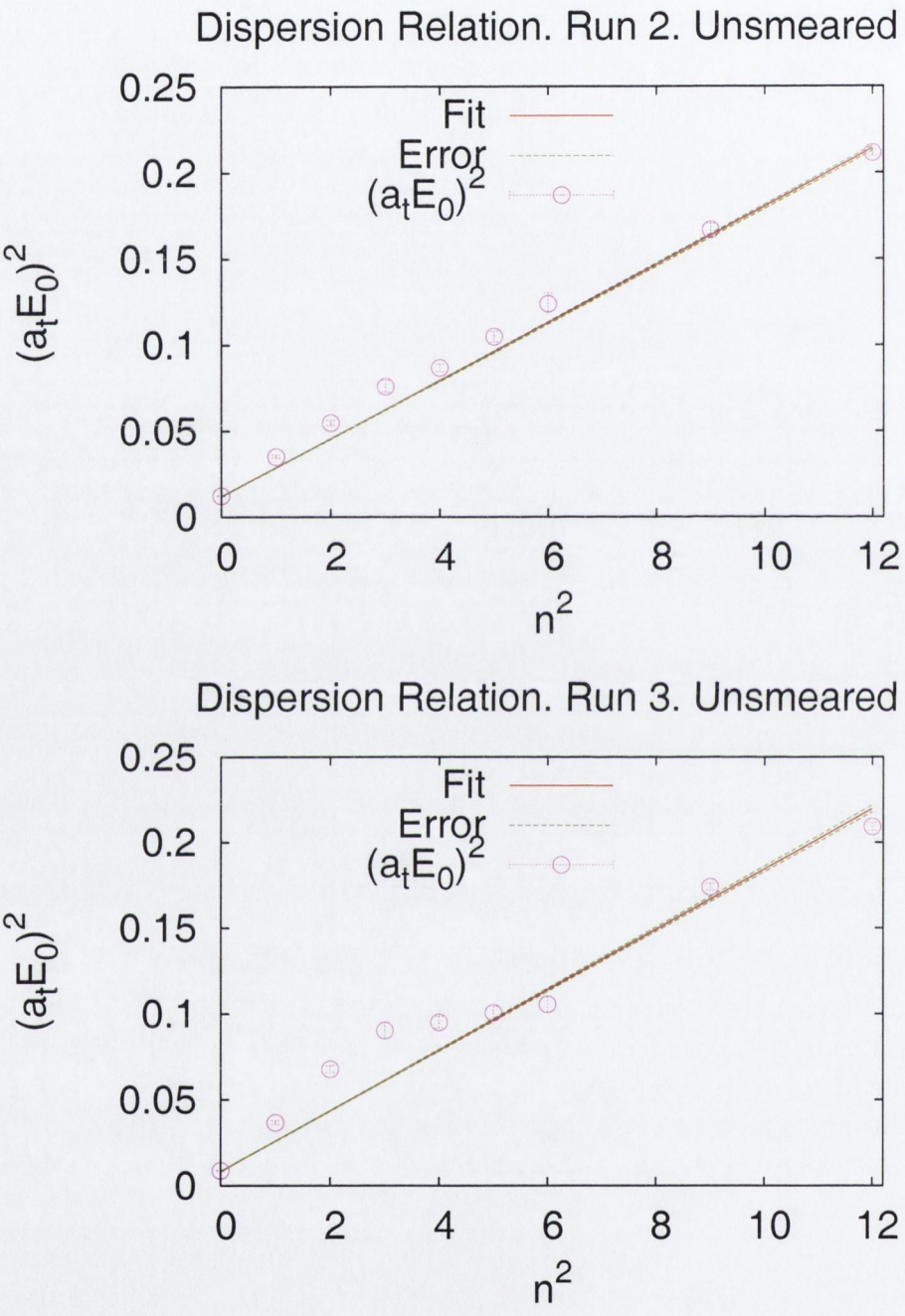

Figure 3-6: Pseudoscalar dispersion relations for Runs 1 & 2. These plots show momenta up to $n^2 = 12$. The results from these fits were discarded due to the high χ^2 values and new fits were made using smeared correlators.

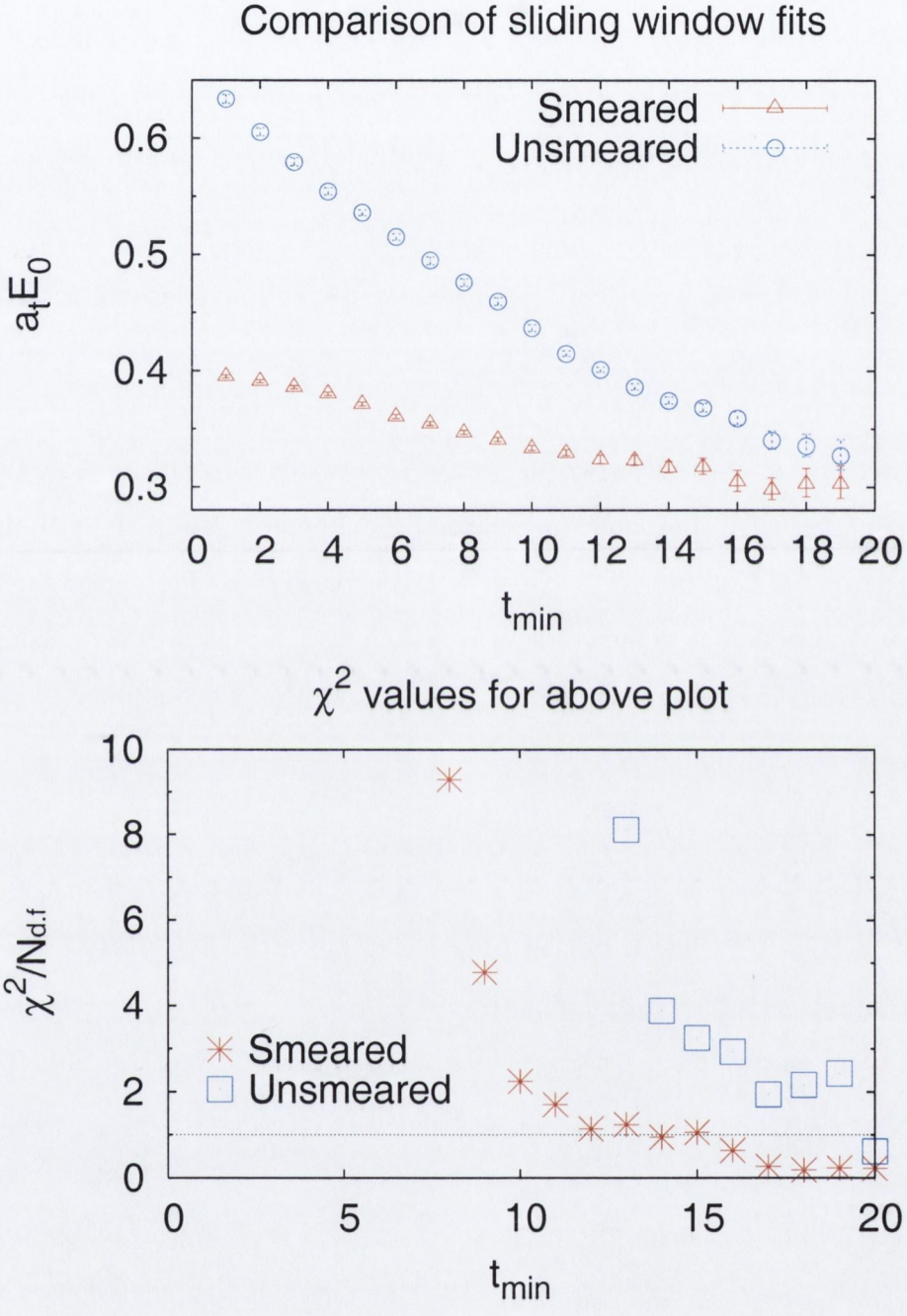

Figure 3-7: These plots show the effects of smearing on sliding window fits and on the associated χ^2 value for each effective mass fit. The top plot shows the effect of smearing on the sliding window fit obtained for an $8^3 \times 48$ lattices for momentum $n^2 = 3$ and with input values corresponding to Run 1 in Table 3.1. The bottom plot compares the corresponding $\chi^2/N_{\text{d.f}}$ values for each fit for the smeared and unsmeared cases. The dotted is included to highlight $\chi^2/N_{\text{d.f}}$. The horizontal axis is given in units of a_t.

original data out towards the centre of the lattice. It was found that choosing a fit range close to the origin of the lattice, for example, choosing a range of $[2, 8]$ gave $a_t E_0 = 0.111 \pm 0.005$ with $\chi^2/N_{d.f} = 4.9/5$ which agreed with the value for the single exponential fit. Due to the sensitivity of the fitted parameters to the fit range it was decided to continue using single exponential fits. The single and double exponential fits for Run 1 for $p^2 = 0$ are shown in Fig. 3-8.

Figs. 3-11 and 3-12 show four pseudoscalar dispersion relations resulting from analysis of the smeared quarkfields for Runs 1, 2 and 3. The first three plots are preliminary plots in which fits were attempted up to a momentum of $n^2 = 12$. The fits that were used to obtain the anisotropy were made only up to a momentum of $n^2 = 3$. A more accurate dispersion relation for momenta up to $n^2 = 6$ along with the effective mass plot for $n^2 = 4$ can be seen in Fig. 3-10. Measurements of ξ_q used in the eventual tuning procedure were taken from more precise fits using ground state masses extracted from momenta $n^2 = \{0, 1, 2, 3\}$, for example the last plot in Fig. 3-12. The resulting values for ξ_q are given in Table 3.4. The simulation closest to the "tuned point" corresponded to Run 2.

The measurements of ξ_g and ξ_q for the first three runs were then combined as explained in Sec. 3.2. The resulting scatterplot shown in Fig. 3-14(i) is extremely noisy. Another set of gauge configurations were generated with input parameters (ξ_q^0, ξ_g^0) corresponding to the central values obtained from the scatterplot. This point is denoted as Run 4 in Fig. 3-14(i) and in Table 3.1. (ξ_q^r, c_g) were again measured over the bootstrapped samples for Run 4 and were found to be 6.47 ± 0.05 and 0.985 ± 0.005 respectively. A constrained-χ^2 fit was made using values all four available runs (Runs 1, 2 3 4). The resulting scatterplot is shown in Fig. 3-14(ii). This gave simulation point for Run 5. The procedure was repeated again and the renormalised output values were found to be $(\xi_q^r, c_g) = (5.80 \pm 0.05, 0.995 \pm 0.003)$. Another constrained-$\chi^2$ fit using all five simulations was made and again this can be seen in Fig. 3-15(iii). This scatterplot was not vastly different from the scatterplot obtained using only the previous four runs. The spread of points has become somewhat smaller but was still significantly large. To get a measure of the spread of the intersection

point, histograms were obtained by projecting the points into the respective axes and binning the data, see Fig. 3-16. At this point it was decided that 48 timeslices were not sufficient to allow contributions from higher order states to die off in the correlation functions so it was decided to go back and repeat the procedure for lattices with 80 sites in the temporal extent. A rough plot was later made using the unsmeared quark data and it is included here in Fig. 3-9 for the sake of comparison with the results from the smeared quarks data e.g Fig. 3-14.

3.5.2 $8^3 \times 80$ lattice

A simulation was performed on $8^3 \times 80$ lattices at point 5 in Table 3.1. Both point and all-to-all propagators, [57], were used for the initial run. All-to-all propagators were determined for a total of 41 momenta up to $n^2 = 6$, See Table A.1.1 for a list of these momenta. The propagators were first generated with 50 eigenvectors for Run 5 and then with no eigenvectors. It was determined that the extra computation involved in the generation of the eigenvectors did not justify the very small change in the quality of the resulting signal. Subsequent runs did not utilise any eigenvectors. The noise vectors were first generated using only time dilution and then by using both time and colour dilution. Fig. 3-17 shows the effect of the different dilutions for an individual correlator. Fig. 3-18 shows the effect of the different dilution levels on a resulting effective mass plot. It can be easily seen that addition of colour dilution significantly reduces the noise. Time and colour dilution with no eigenvectors was used for the remaining measurements.

An immediate improvement in the quality of the fit due to the longer temporal extent of the lattice was observed. Sliding window fits were used to determine the optimal fit ranges to the correlator data. An example of such a plot is given in Fig. 3-19. The fit ranges chosen are given in Table 3.3. The ground state energy was determined from fits over at least 15 timeslices and was stable with respect to changes in t_{min}. The effect of the longer lattice is illustrated in Figure 3-20. It shows that the values of $a_t E_0$ extracted from the shorter lattice are overestimated due to contamination from higher order states. The stability of the sliding window plots

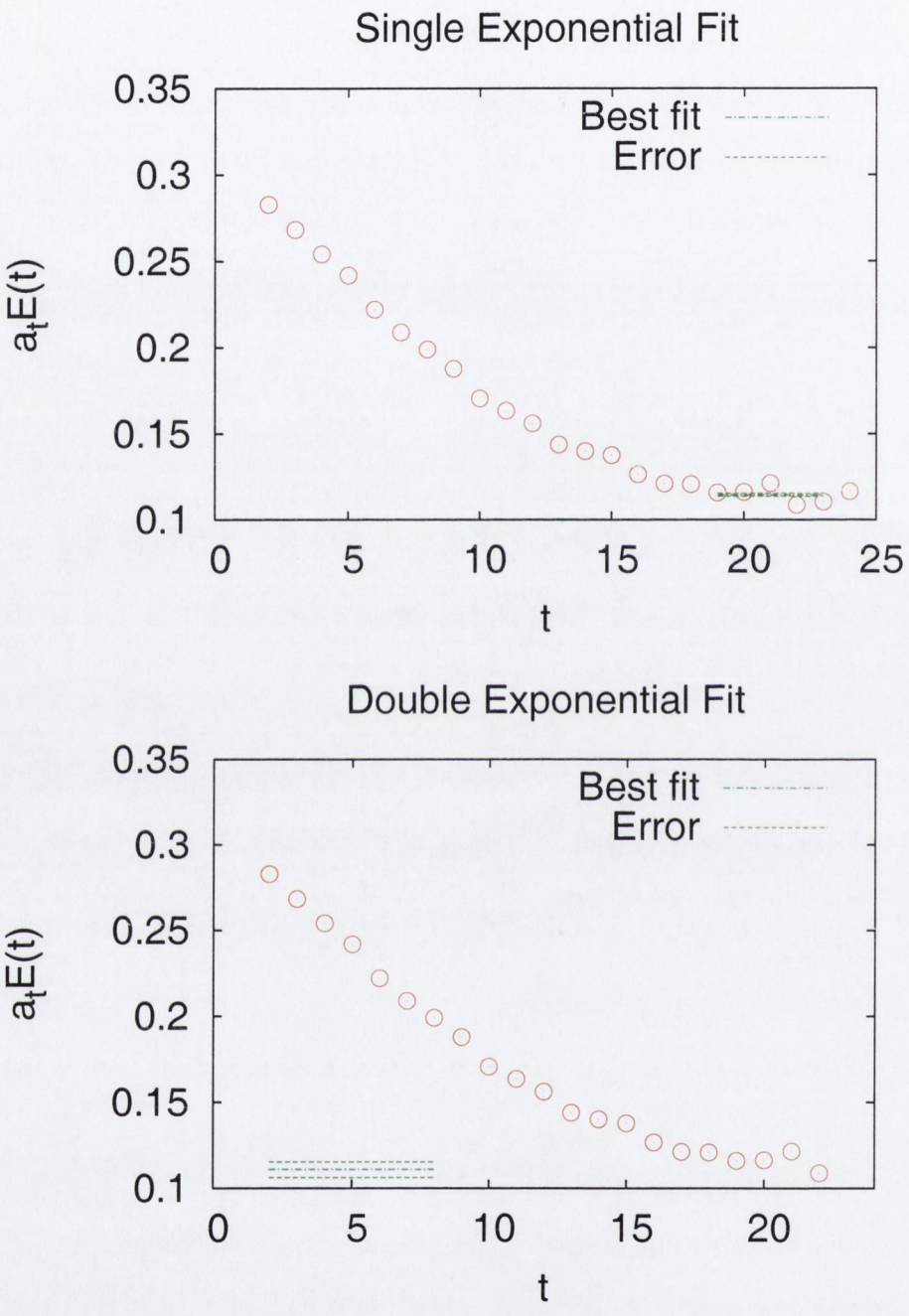

Figure 3-8: Effective mass plots for Run 1. Quark smearing has been used. For the single exponential fit a fit range of [19,23] was used and the resulting value $a_tE_0 = 0.115 \pm 0.001$ was extracted with a $\chi^2/N_{d.f} = 13/3$ for the fit. For the double exponential fit, the fit range used was [2,8], $a_tE_0 = 0.111 \pm 0.005$ with $\chi^2/N_{d.f} = 4.9/5$. The horizontal axis is given in units of a_t.

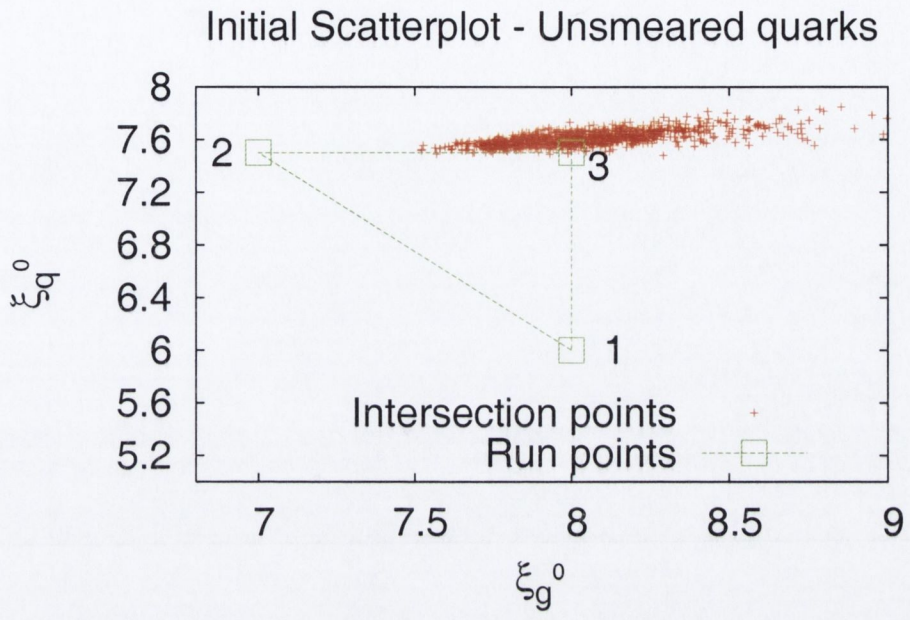

Figure 3-9: This plot shows the resulting scatterplot from the first three runs. Each point on the graph represents an intersection point from the two unconstrained planar fits with the target anisotropy ξ^t for a particular bootstrap.

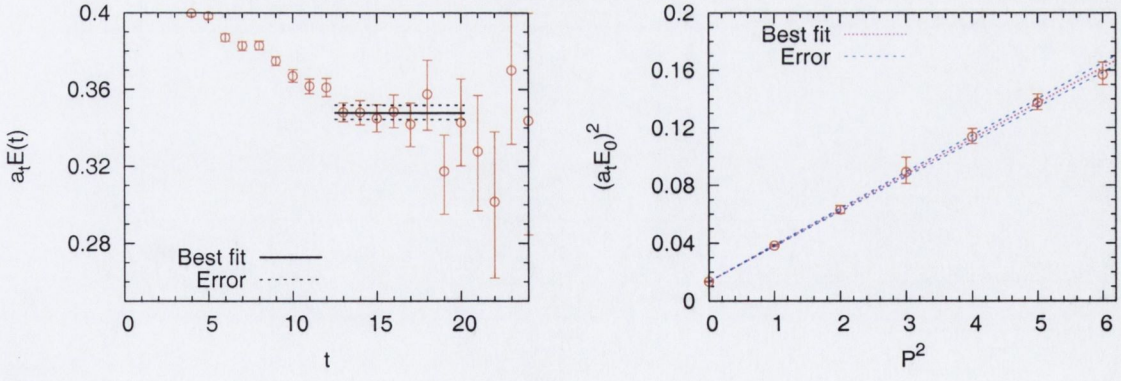

Figure 3-10: The left plot shows the effective mass for degenerate quark mass $a_t m_q = -0.057$ momentum $n^2 = 4$. The fit range is [14:20] with a $\chi^2/N_{d.f} = 0.81$. The horizontal axis is given in units of a_t. The right plot is a pseudoscalar dispersion relation with a $\chi^2/N_{d.f} = 0.14$. Both come from simulation parameters at point 1 on Fig. 3-14 using point propagators and smeared quark fields.

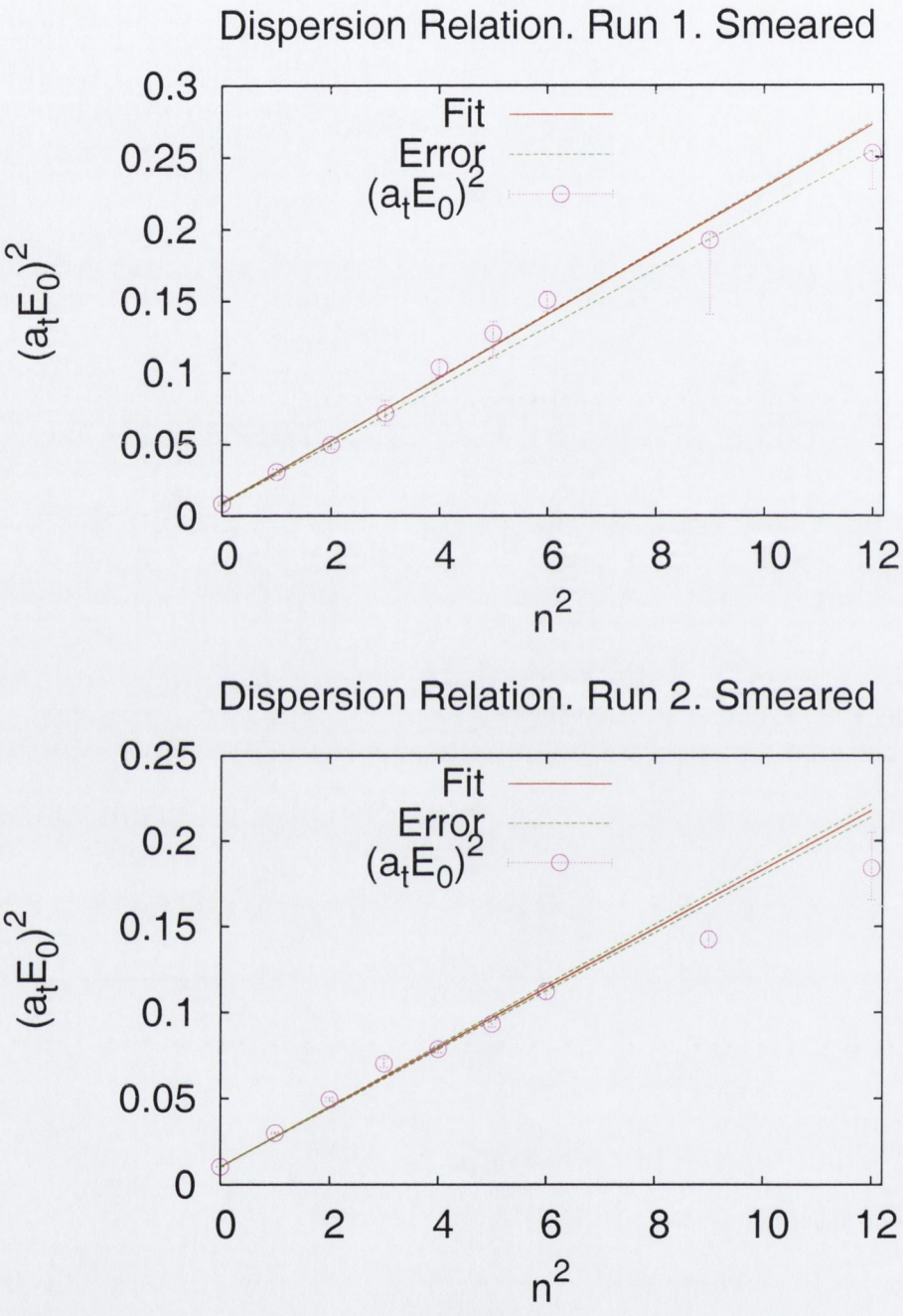

Figure 3-11: These plots show initial attempts at plotting dispersion relations obtained from the smeared quarks on Runs 1 and 2 on the $8^3 \times 48$ lattices. Note that the values of ξ_q used in the generation of the scatterplots were taken from more precise fits using only momenta $n^2 = \{0, 1, 2, 3\}$.

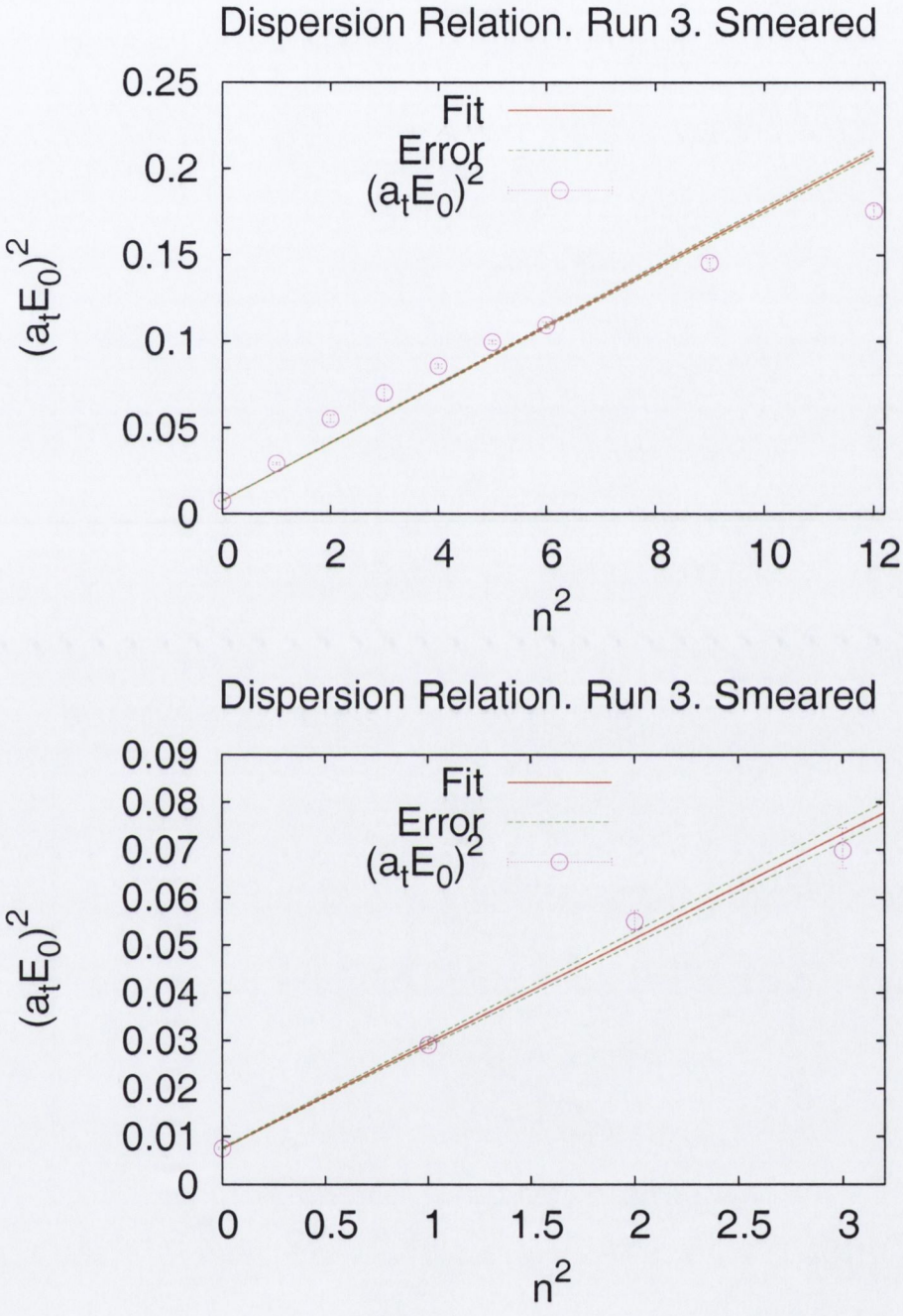

Figure 3-12: These plots show initial attempts at plotting dispersion relations obtained from the smeared quarks on Run 3 on the $8^3 \times 48$ lattices. The bottom plot shows a fit for Run 3 using only the first 4 momenta. This fit gives a value of $\xi_q = 5.18 \pm 0.08$ with a $\chi^2/N_{d.f} = 2.6$. The plot on the top shows a fit on momenta up to $n^2 = 12$ and the value obtained is $\xi_q = 6.05 \pm 0.03$ but with a $\chi^2/N_{d.f} = 45.7$.

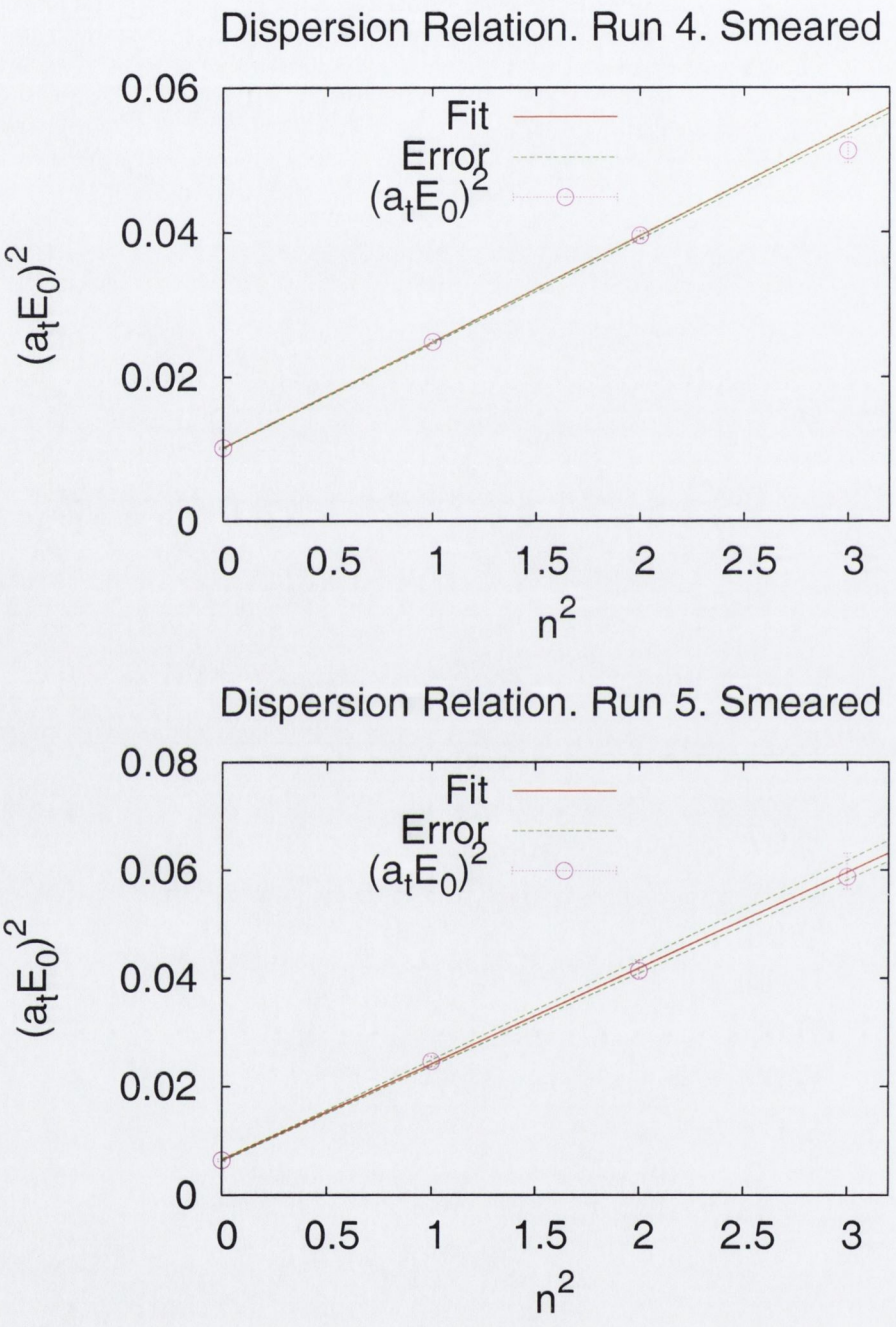

Figure 3-13: Dispersion relations for Runs 4 and 5. The measured value for ξ_q is 6.48 ± 0.05 with a $\chi^2/N_{d.f} = 2.25$ for Run 4 and 5.88 ± 0.10 with a $\chi^2/N_{d.f} = 0.19$ for Run 5.

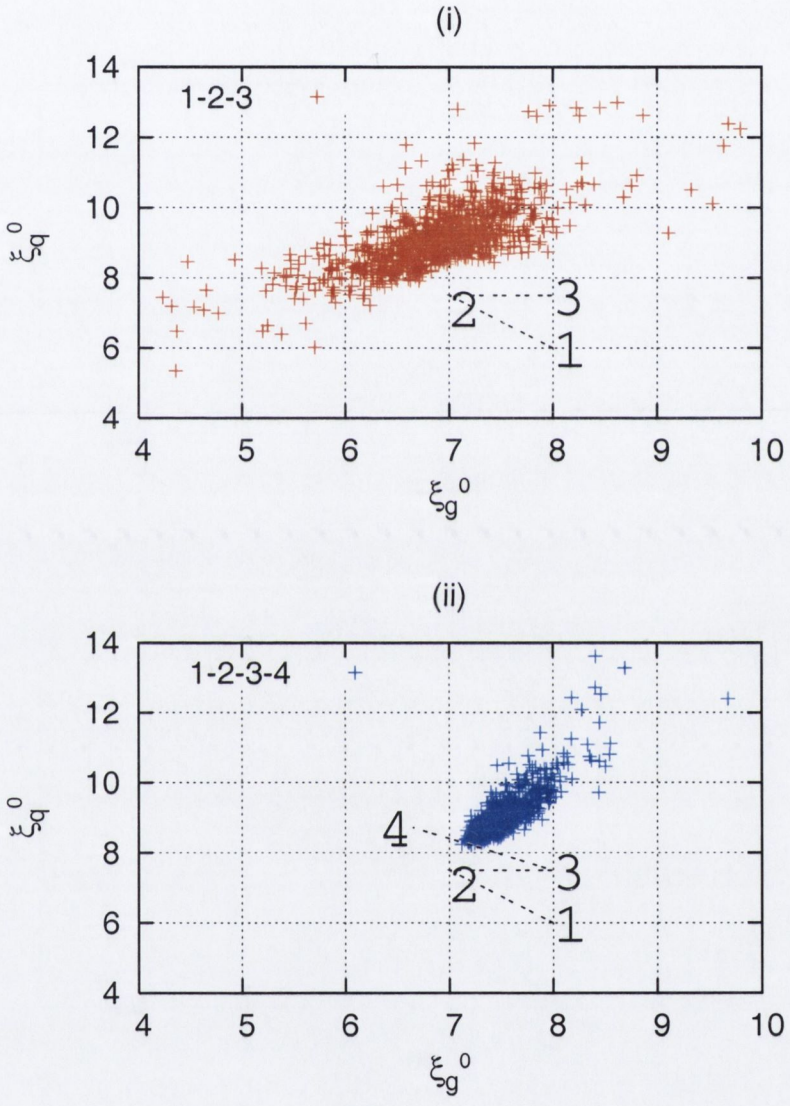

Figure 3-14: This figure shows the first two steps in the progression of the tuning procedure. (i) shows the scatterplot for a fit to the first 3 sets of configurations. (ii) shows a χ^2 fit for the first four points. Each point on a scatterplot shows an estimate of a tuned point from different bootstrapped samples.

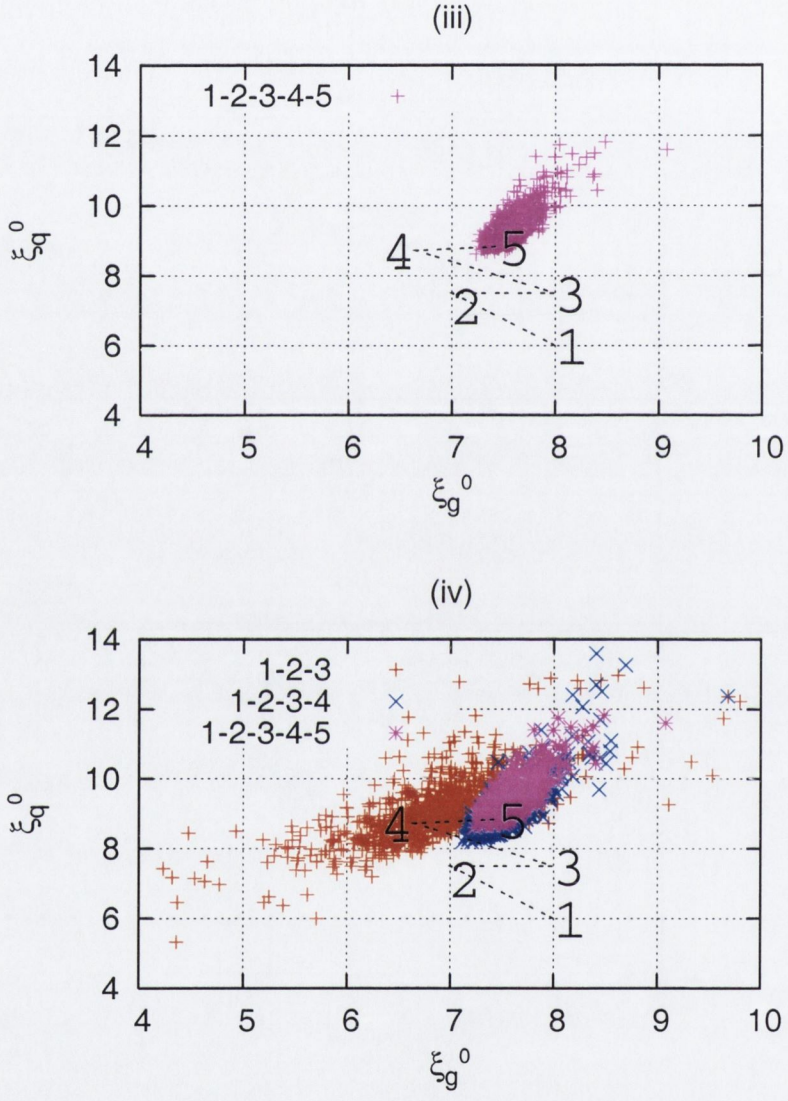

Figure 3-15: This figure shows the next stage in the progression of the tuning procedure. Plot (iii) shows a χ^2 fit for 5 sets. (iv) shows all 3 scatterplots together.

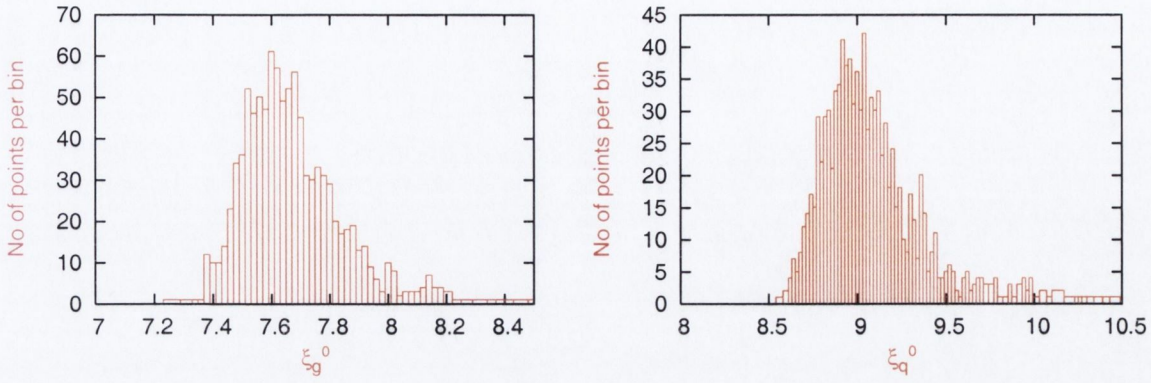

Figure 3-16: Histogram of coordinates for 5-run scatterplot from Figure (3-15). The plot on the left is the x-coordinate, ξ_g, plot on the right is for the y-coordinate ξ_q.

however leads to the conclusion that the $8^3 \times 80$ lattices are sufficient to measure $a_t E_0$ accurately. This plot also compares simulations using point and all-to-all propagators. The all-to-all propagators lead to improved precision in the fitted energies however at an increased computational cost. The central values are in agreement with the energies determined using point propagators but the statistical error is smaller. The renormalised anisotropies measured for Run 5 gave $(c_g, \xi_q^R) = (0.991(7), 6.95(8))$. The same tuning procedure used on the $8^3 \times 48$ lattices was repeated for the longer lattices by simulating again at points 1 and 4 as together these spanned the largest area of the plane. Consistently good fits are found for all runs for the first four momenta considered ($n^2 = 0, 1, 2$ and 3). The renormalised quark anisotropy is therefore determined from fits to these momenta. Fig. 3-21 shows the resulting pseudoscalar dispersion relations for Runs at points 1 4 and 5. When combined with the values for c_g from these runs, the resulting scatterplot is shown in Fig. 3-22 by the plot marked $R = 3, T = 2$.

3.5.3 ξ_g

As a check on the stability of the tuning procedure, c_g was again measured using different values of R and T in the determination of the gluon anisotropy for the $8^3 \times 80$ lattices. Table 3.2 shows the resulting c_g for different R and T. It can be seen that the values are generally quite consistent for each run. Looking more closely at

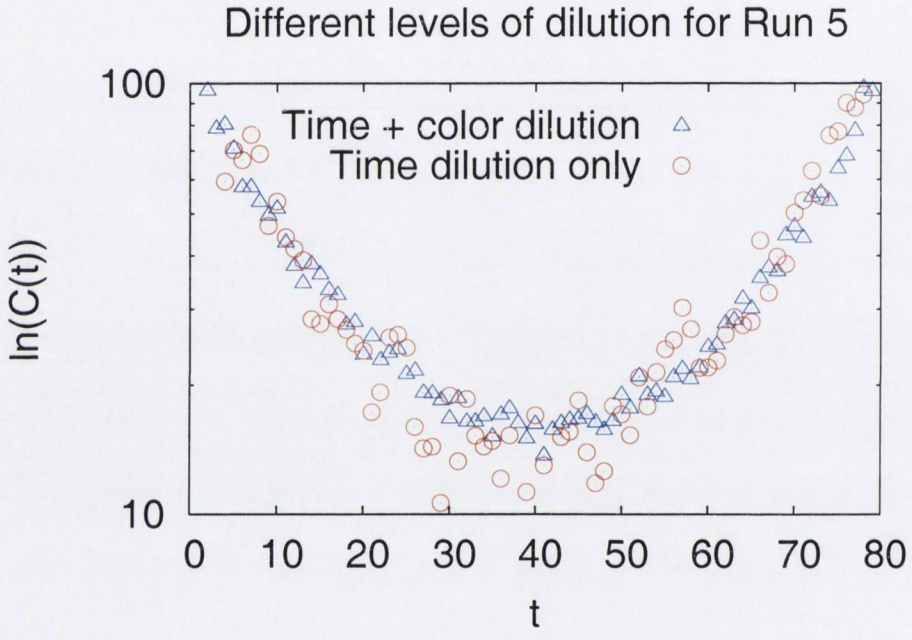

Figure 3-17: This plot shows the effect of different dilution on the correlation function measured on a single background configuration. These are pseudoscalar (pion) correlation functions for momentum $n^2 = 0$ from Run 5. See Table 3.1. Again the x-axis is given in units of a_t.

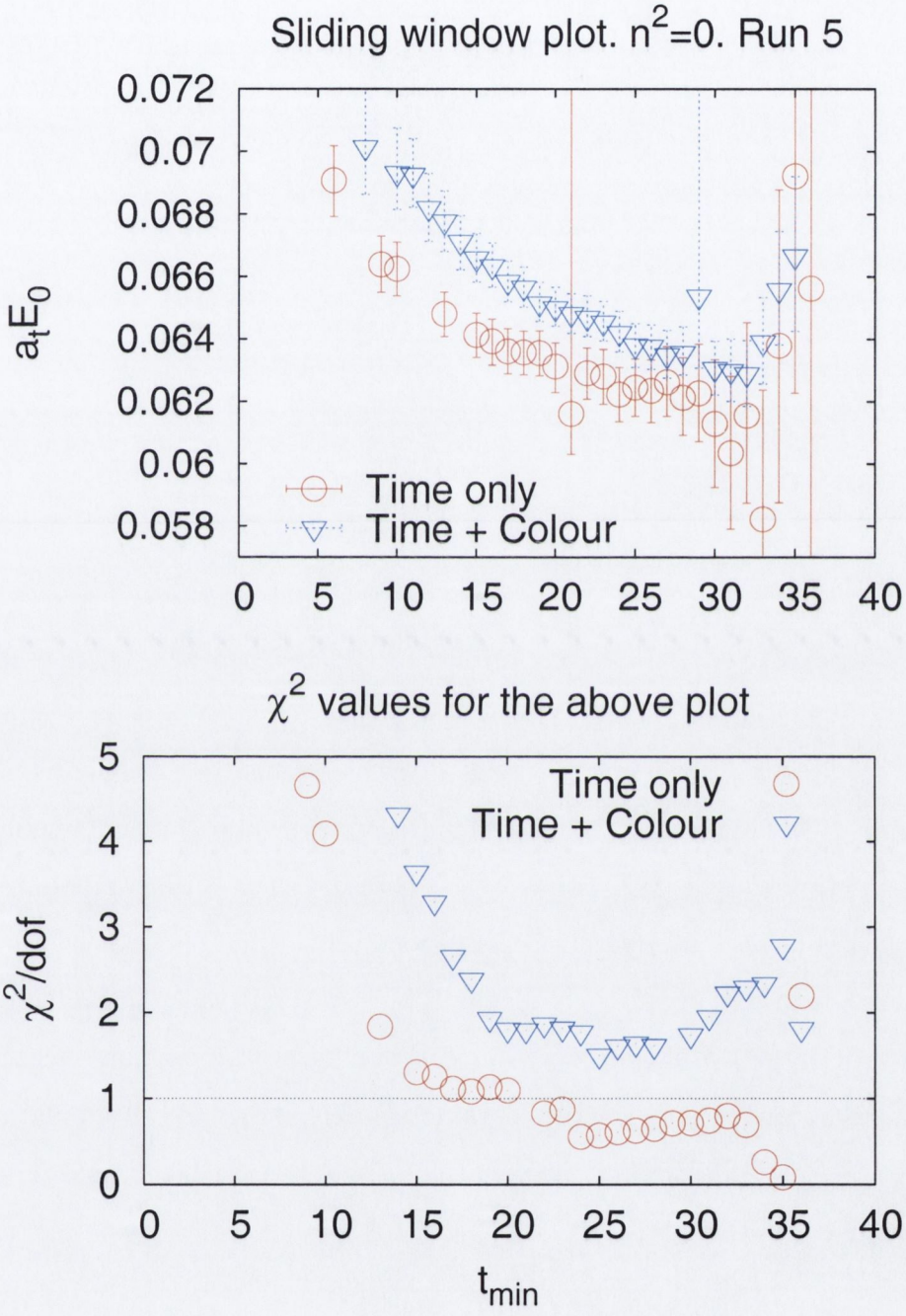

Figure 3-18: The top plot shows a fit to 173 configurations using noise generated with time dilution only. The bottom plot shows a fit using noise generated with time and colour dilution but on 250 configurations. In both plots, the left vertical axis denotes $a_t E_0$ and the right vertical axis gives the $\chi^2/N_{d.f}$ value for a fit back to a particular timeslice. t_{max} was set to 40 in both cases. The x-axis is presented in units of a_t

	$c_g = V_s(x)/V_t(t/\xi)$ at different (T,R)					
Run	(1,3)	(1,4)	(2,3)	(2,4)	(3,3)	(3,4)
1	0.972(2)	0.959(3)	0.972(7)	0.965(13)	0.991(25)	1.13(8)
4	0.951(2)	0.941(4)	0.945(8)	0.926(18)	0.942(34)	0.89(9)
5	0.994(2)	0.990(3)	0.991(7)	0.998(13)	0.965(25)	1.01(7)
6	1.004(2)	0.997(3)	0.983(6)	0.994(12)	1.014(19)	1.04(6)
7	1.010(1)	1.005(2)	1.006(4)	1.003(5)	1.033(12)	1.038(22)

Table 3.2: The gluon anisotropy parameter c_g for different separations, R and times, T. The final results were determined from data at $T = 2$ and $R = 3$.

n^2	t_{min}	t_{max}
0	25	40
1	24	40
2	21	40
3	19	40

Table 3.3: Fit ranges.

the effective potential for each R as a function of T, it can be seen that it has not yet reached a plateau at $T = 1$, while the value for $T = 3$ is consistent within errors with that for $T = 2$. $(T, R) = (2, 3)$ were again chosen as the parameters, since this combination yields reasonably small statistical errors, while R is large enough to be in the linear régime. Figs. 3-22 and 3-23 compare the effect of the different choices of R, T on the resulting scatterplot for the unconstrained fit. The plot shows that the anisotropies are insensitive to a change in R but that increasing the value of T from 2 to 3 leads to large statistical uncertainty, particularly in the gluon anisotropy.

The same fit ranges and smearing parameters were chosen for all simulation points in order to obtain a consistent determination of the dispersion relation. The final fit ranges are given in Table 3.3.

3.5.4 Simulation with tuned parameters

Applying the plane fit procedure of Sec. 3.2 to a subset of configurations of Runs 1, 4 and 5 preliminary, tuned parameters $\xi_g^0 = 8.06^{+7}_{-7}, \xi_q^0 = 7.52^{+21}_{-15}$ were obtained. This point is denoted as Run 6 on the relevant plots. 250 configurations were then generated with these parameters, and c_g and ξ_q determined using the same values for

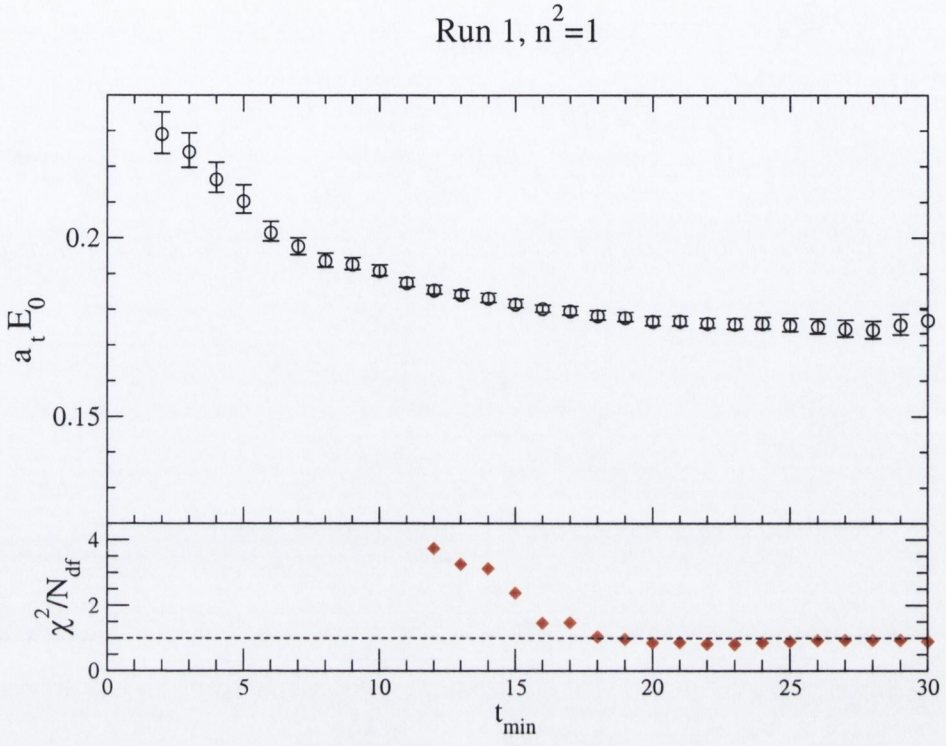

Figure 3-19: A typical t_{min} plot, showing the energy for momentum $n^2 = 1$ on run 1, $8^3 \times 80$ lattices from fits to time ranges $t_{\text{max}} = 40$ for various t_{min}. A stable ground state energy determination, with a good χ^2, is achieved for $22 \leq t_{\text{min}} \leq 30$.

R, T and fit ranges as in Sections 3.3.1 and 3.3.2. It was found that $c_g = 0.983^{+6}_{-6}, \xi_q = 6.21^{+9}_{-9}$). It was found that both quark and gluon anisotropies were within 3% of the target value of 6. Although the anisotropies were not equal within statistical errors, it was noted that there are still systematic uncertainties at the percent level, in particular for ξ_g, as shown in Table 3.2. For example, if $R = 3, T = 3$ was chosen it was found that $c_g = 1.01(2)$.

The plane fit procedure was repeated to include the new information from Run 6. Figure 3-24 shows the resulting scatterplot determined on the $8^3 \times 80$ lattice from runs 1, 4, 5 and 6. A new scatterplot, Fig. 3-24 was obtained. The intersection points shifted in a direction to move c_g and ξ_q even closer to the target anisotropy. The corresponding histograms are presented in Fig. 3-25. A final two input parameters of $\xi_q^0 = 7.43$ and $\xi_g^0 = 8.42$ were chosen. and this point is denoted as Run 7 in the relevant tables. The renormalised values measured at simulations at this point were $c_g = 1.006(4)$ and $\xi_q = 5.68(4)$.

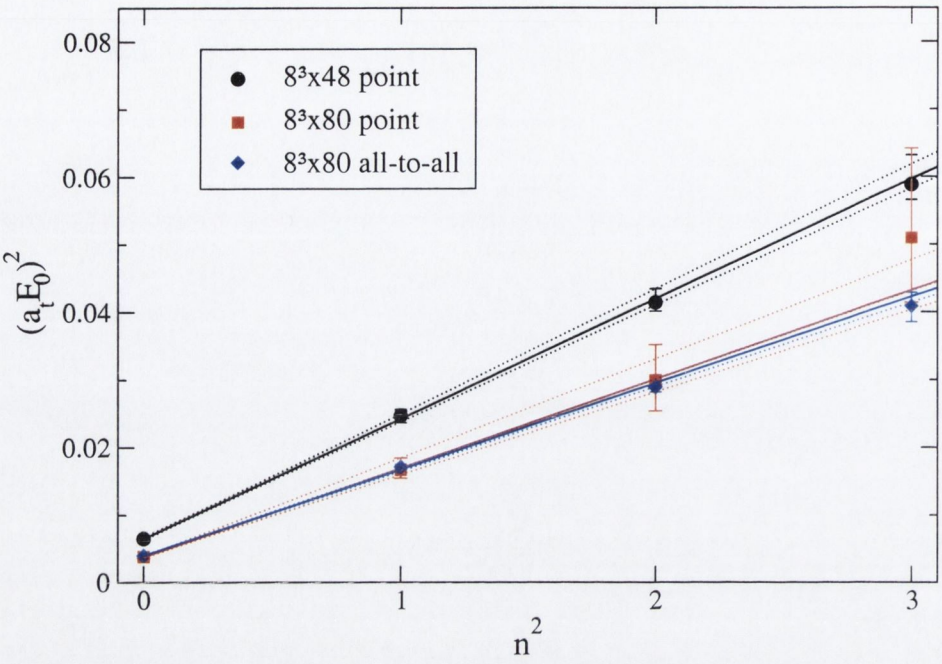

Figure 3-20: A comparison of the dispersion relations determined from an $8^3 \times 48$ lattice and an $8^3 \times 80$ lattice. The solid lines are the best fits and the dotted lines are the 68% confidence levels. The figure also shows a comparison of all-to-all propagators and point propagators on the same (longer) lattice. The plot shows that the ground state energies have not reached a plateau on the shorter lattice. On the longer lattice the all-to-all and point data agree, while higher precision is achieved with all-to-all propagators. These measurements were done for the Run 5 parameters.

The information from the simulation at point 7 was combined with the other four point $(1, 4, 5, 6)$ to determine the scatterplot presented at the top of Fig. 3-26. The measurement obtained from this scatterplot gave a new set of input parameters $(\xi_g^0, \xi_q^0) = (8.22^{+0.05}_{-0.05}, 7.64^{+0.09}_{-0.09})$. Two unconstrained fits were also attempted using the nearest points in order to compare the resulting scatterplots. These are shown at the bottom of Fig. 3-26 for $(1, 6, 7)$; and the top of Fig. 3-27 for $(5, 6, 7)$. It can be seen that the results from all three fits coincided with each other. All three scatterplots are plotted on top of each other for the bottom plot of Fig. 3-27.

It was decided that the fitting procedure had resulted in input parameters that were sufficiently tuned and further simulation was not performed at the values obtained from the new scatterplot.

In order to get a rough idea of the physical scales of these lattices, the pion mass, the rho mass and the string tension were computed. For Run 6, the measured

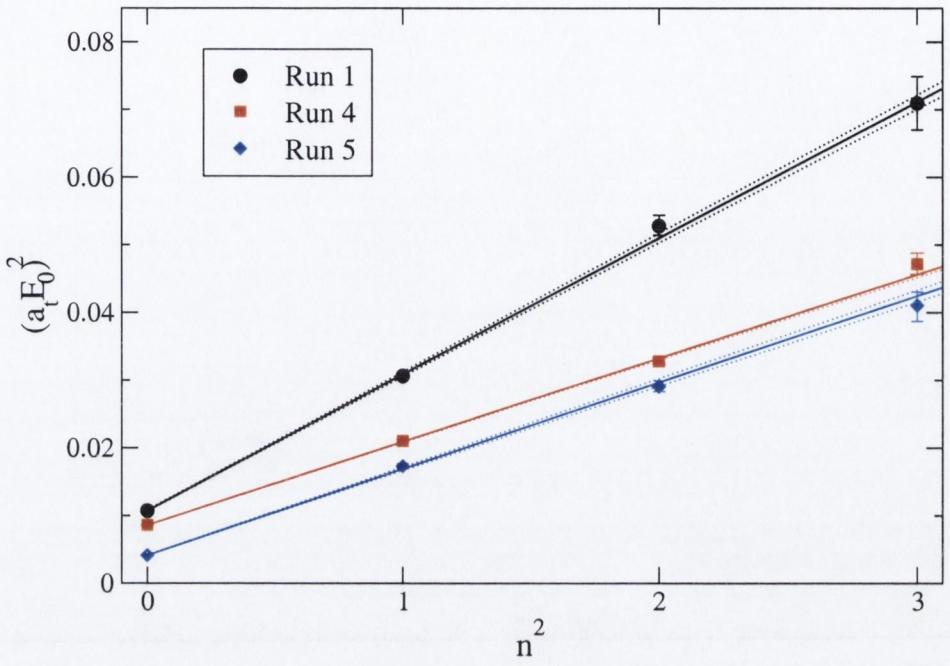

Figure 3-21: Dispersion relations from runs 1, 4 and 5 on $8^3 \times 80$ lattices using all-to-all propagators. The solid line is a fit to the four points and the dotted lines are the 68% confidence levels. The quality of all three fits is very good with $\chi^2/N_{d.f.} = 2.0/2, 1.9/2, 2.0/2$ for runs 1,4 and 5 respectively.

values obtained were $a_t m_\pi = 0.066(1)$ and $a_t m_\rho = 0.120(5)$, which gives $m_\pi/m_\rho = 0.54$, while a crude measurement of the string tension from the gives $a_s = 0.2$fm. This crude measurement was performed by measuring the interquark potential for large separations and fitting it to the linear part of the Cornell Potential. More precise measurements of the lattice spacings were performed in the study of Karsch Coefficients in Chapter 4 and the method will be discussed further in Section 4.2.

3.6 Conclusions

It was found that the original ($8^3 \times 48$) lattices used were too short in the time direction to allow a reliable determination of ground state energies, which were found to be systematically high, in particular for higher momenta. This led in turn to systematically high values for ξ_q. The adoption of lattices with longer time extent was a crucial step in the procedure. As Table 3.3 shows, the optimal fit ranges were generally found to be beyond the range of the shorter lattice.

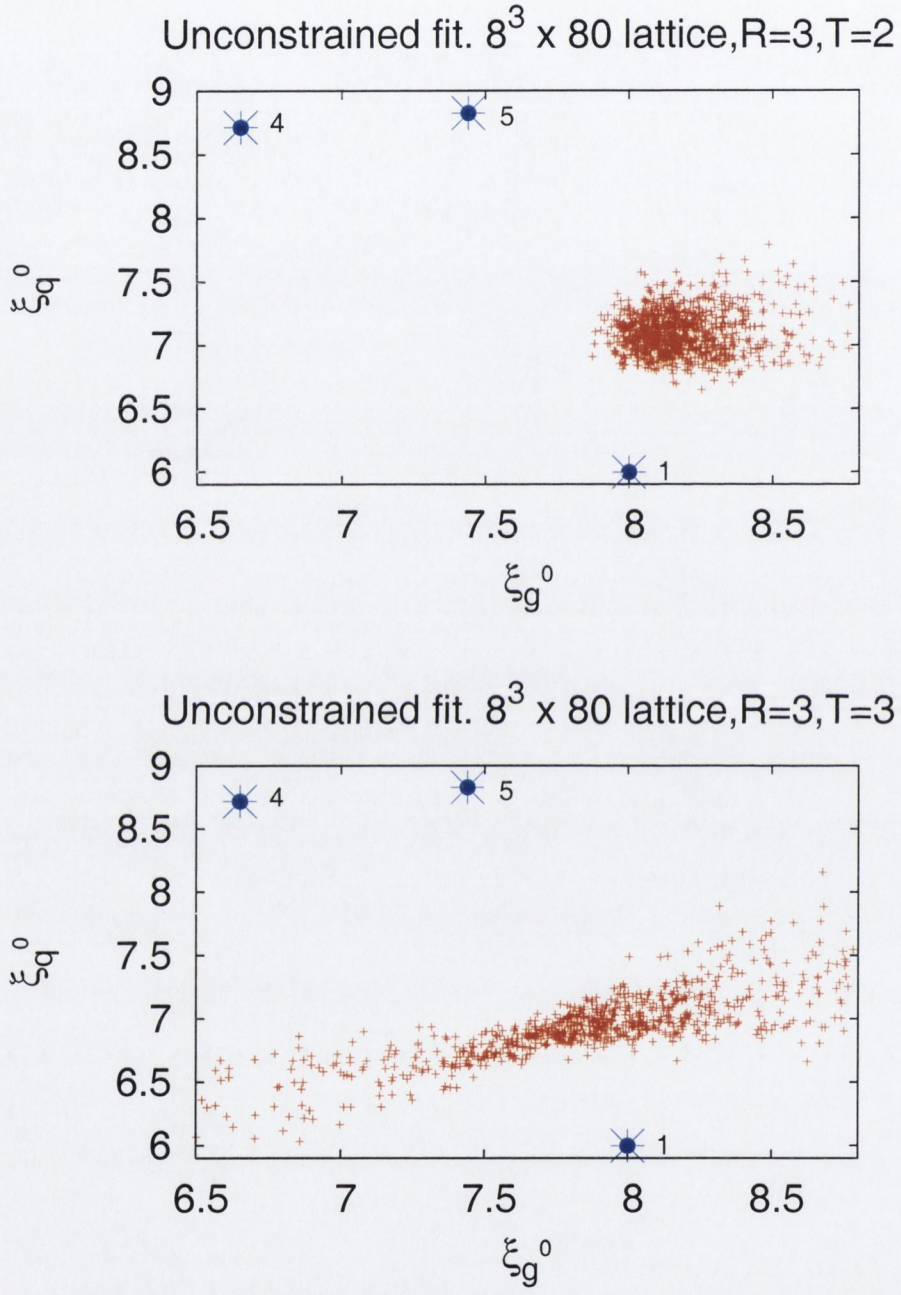

Figure 3-22: Tuned values of input parameters (ξ_g^0, ξ_q^0) determined from the plane fit procedure on the $8^3 \times 80$ lattice. The plots show the results for different values of T used to determine the gluon anisotropy when $R = 4$. Each point corresponds to one bootstrap sample. A similar plot is shown for $R = 4$ in Fig. 3-23.

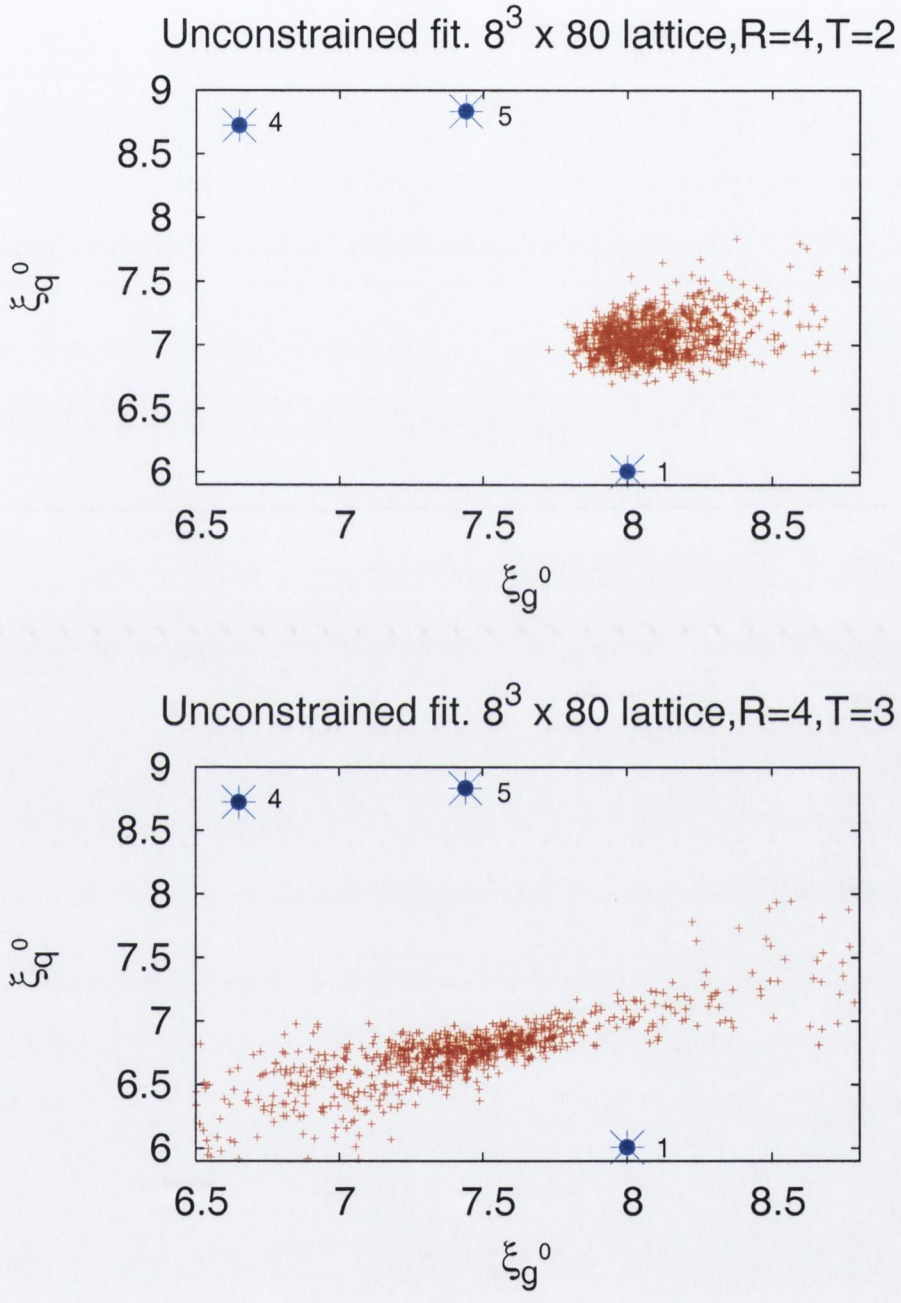

Figure 3-23: Tuned values of input parameters (ξ_g^0, ξ_q^0) determined from the plane fit procedure on the $8^3 \times 80$ lattice. The plots show the results for different values of T used to determine the gluon anisotropy when $R = 3$. A similar plot is shown for $R = 3$ in Fig. 3-22.

	$8^3 \times 48$		$8^3 \times 80$	
Run	c_g	ξ_q	c_g	ξ_q
1	0.991(3)	4.98(6)	0.972(7)	5.54(6)
2	0.986(3)	6.27(4)		
3	1.001(3)	5.18(6)		
4	0.985(5)	6.47(5)	0.945(8)	7.08(5)
5	0.995(3)	5.80(5)	0.991(7)	6.95(8)
6			0.983(6)	6.2(1)
7			1.006(4)	5.78(4)

Table 3.4: Table of measured output anisotropies at each of the run points. The errors are statistical only.

The first attempted tuned point was found to lie marginally outside the triangle used for the plane fit procedure, so the end result was based on an extrapolation rather than an interpolation. This increases both the statistical and systematic uncertainties of the determination. To avoid this problem, it is important to choose a large enough triangle to start with, so that successive parameter determinations are always based on interpolations.

The tuned parameters (ξ_g^0, ξ_g^0) were determined with a statistical uncertainty of 1% and 3% respectively from the ensembles of 250 configurations. In addition, there are three main sources of systematic uncertainties:

1. The R and T values used in the determination of the sideways potential, and the fit ranges used in the determination of the pseudoscalar dispersion relation. Since the fit ranges are chosen to give stable ground state energies, it can safely be assumed that the latter is a small effect. The effect of varying R is also small, as shown in Figs. 3-22 and 3-23. There may be a systematic error arising from the choice of T, but this is obscured by the larger statistical uncertainties in the $T = 3$ data, particularly in the ξ_g^0 direction.

2. Lattice sizes. The pion dispersion relation is unlikely to be strongly affected by the finite lattice volume, but the static quark potential may contain finite volume errors which affect our results. Simulations at the tuned point on larger volumes, could be used to determine whether this is a significant issue.

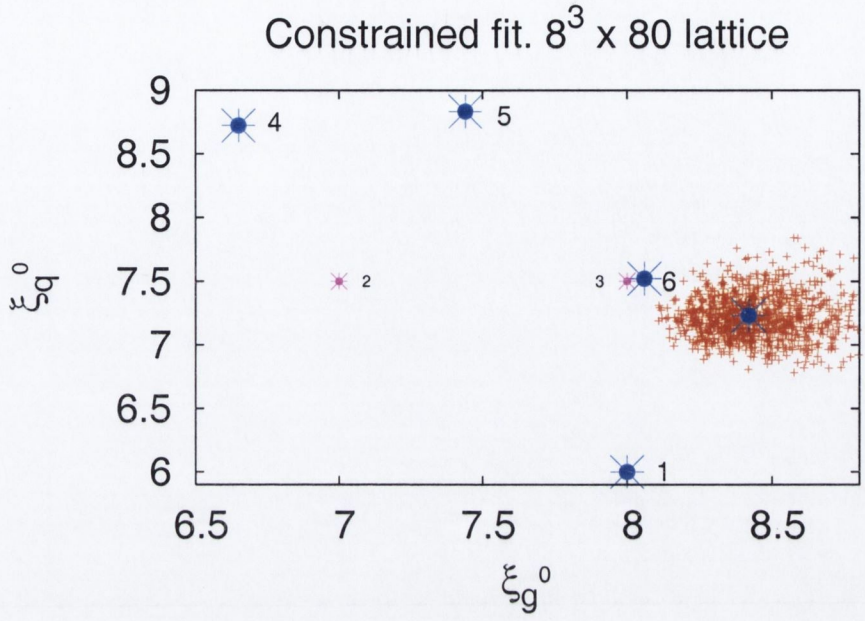

Figure 3-24: As in Fig 3-23. The figure shows the results from a plane fit using parameters from runs 1, 4, 5 and 6. The point at the centre of the scatterplot, at $(\xi_g^0, \xi_q^0) = (8.42, 7.23)$, indicates the result of the best fit.

3. Nonlinearities in the dependence of (ξ_g, ξ_q) on (ξ_g^0, ξ_q^0). The final fit to five points shows no evidence of any significant nonlinearity. If this were found to be a serious issue in any future simulation, a two-step procedure may be adopted where a smaller triangle centred on the preliminary tuned point is used in the second step.

Some preliminary results using the parameters corresponding to point 6 in Fig. 3-24 were presented in Ref. [84, 85, 86]. Further results using the more accurately tuned Run 7 were presented in Ref. [87].

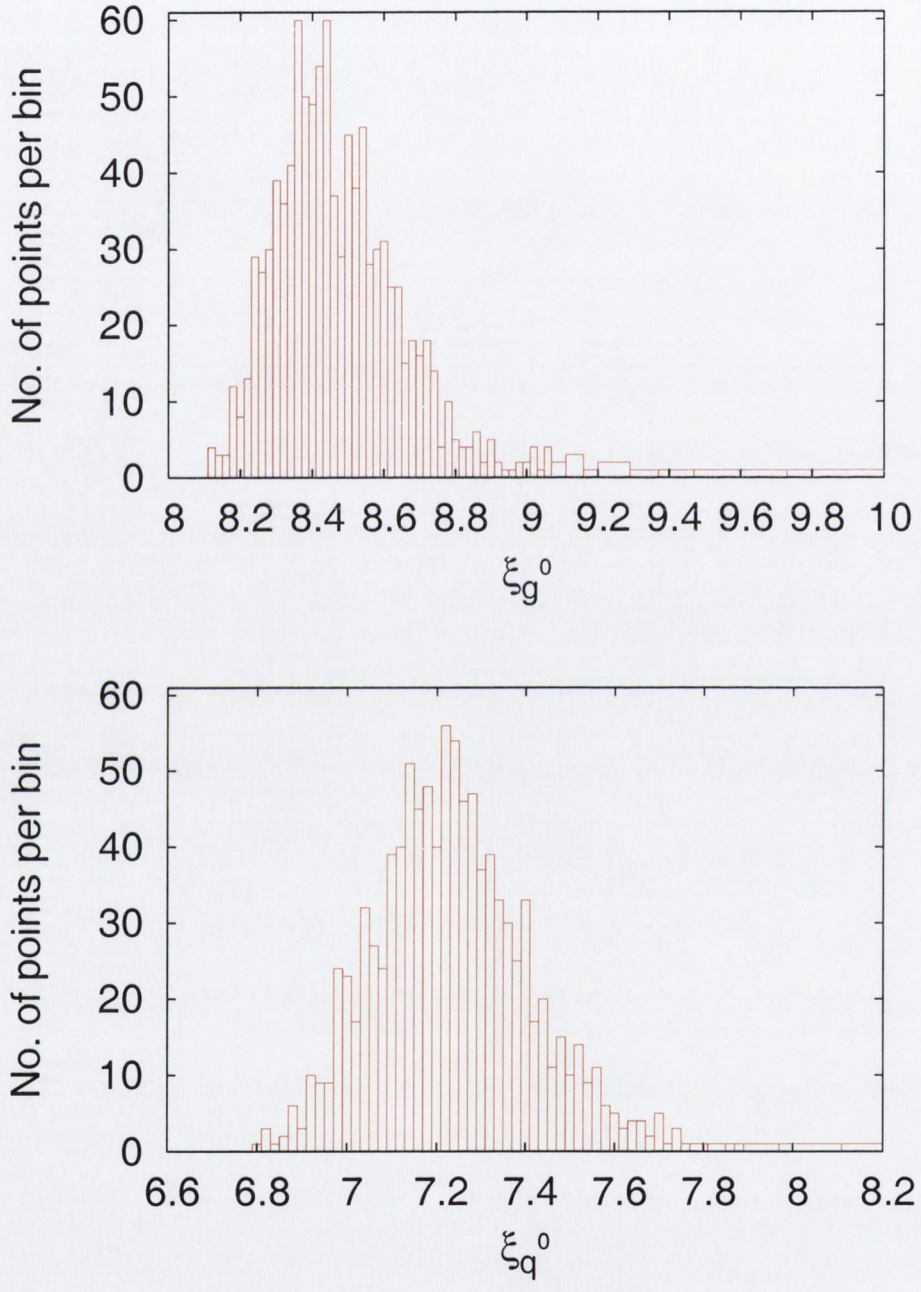

Figure 3-25: Histograms for point 7

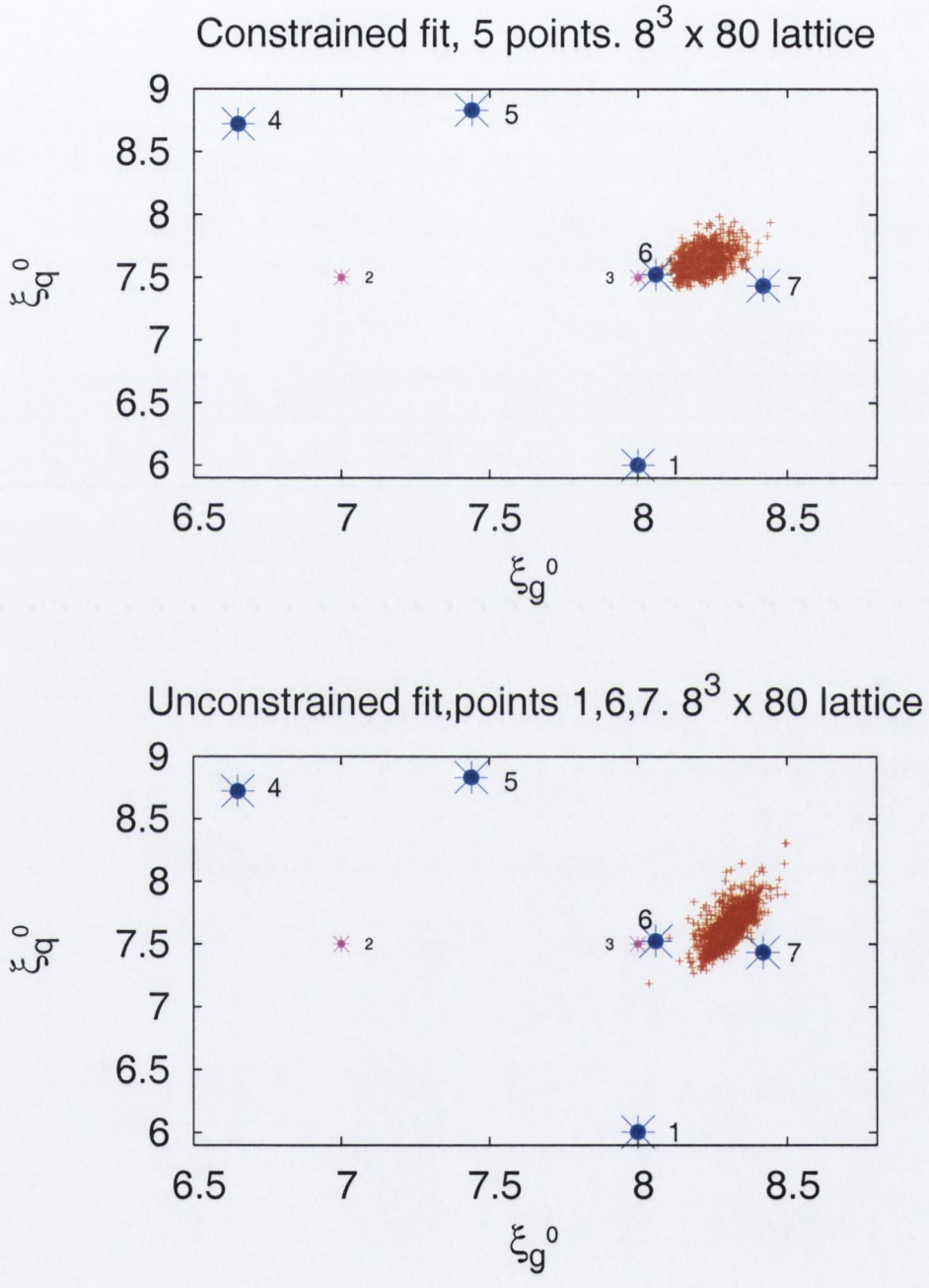

Figure 3-26: The top figure shows the results from a plane fit using parameters from runs 1, 4, 5, 6 and 7. The other plot is an unconstrained fit to a sets of three points, namely $(1, 6, 7)$. Two similar plots are shown in Fig. 3-27.

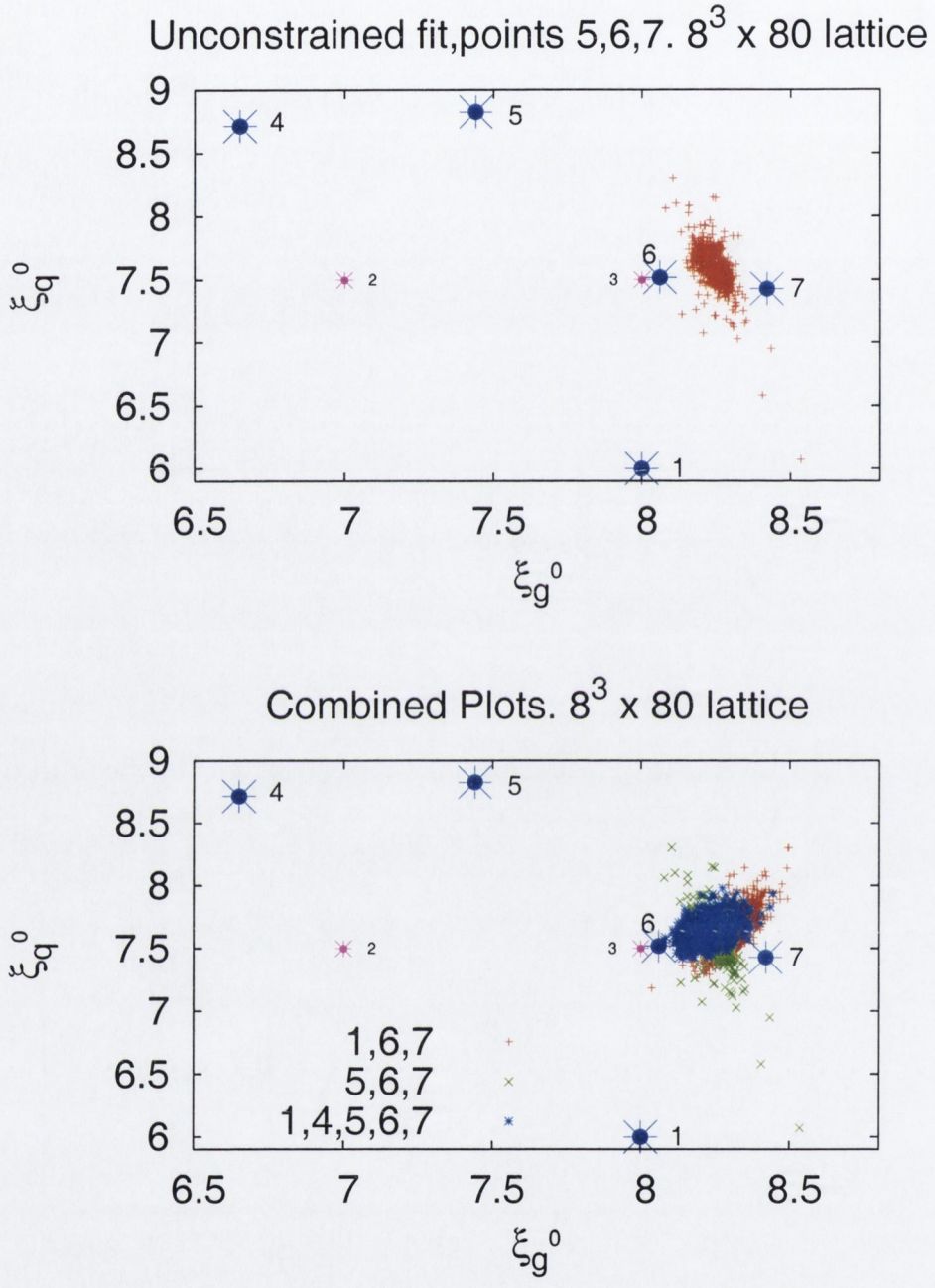

Figure 3-27: The top figure shows the results from an unconstrained plane fit using parameters from runs $(5, 6, 7)$. The bottom plot last plot is a superposition of the top plot and the two plots from Fig. 3-26. The fact that the unconstrained fit using point 1 agrees with the unconstrained fit using point 5 gives an indication that the linear model approximation used is valid.

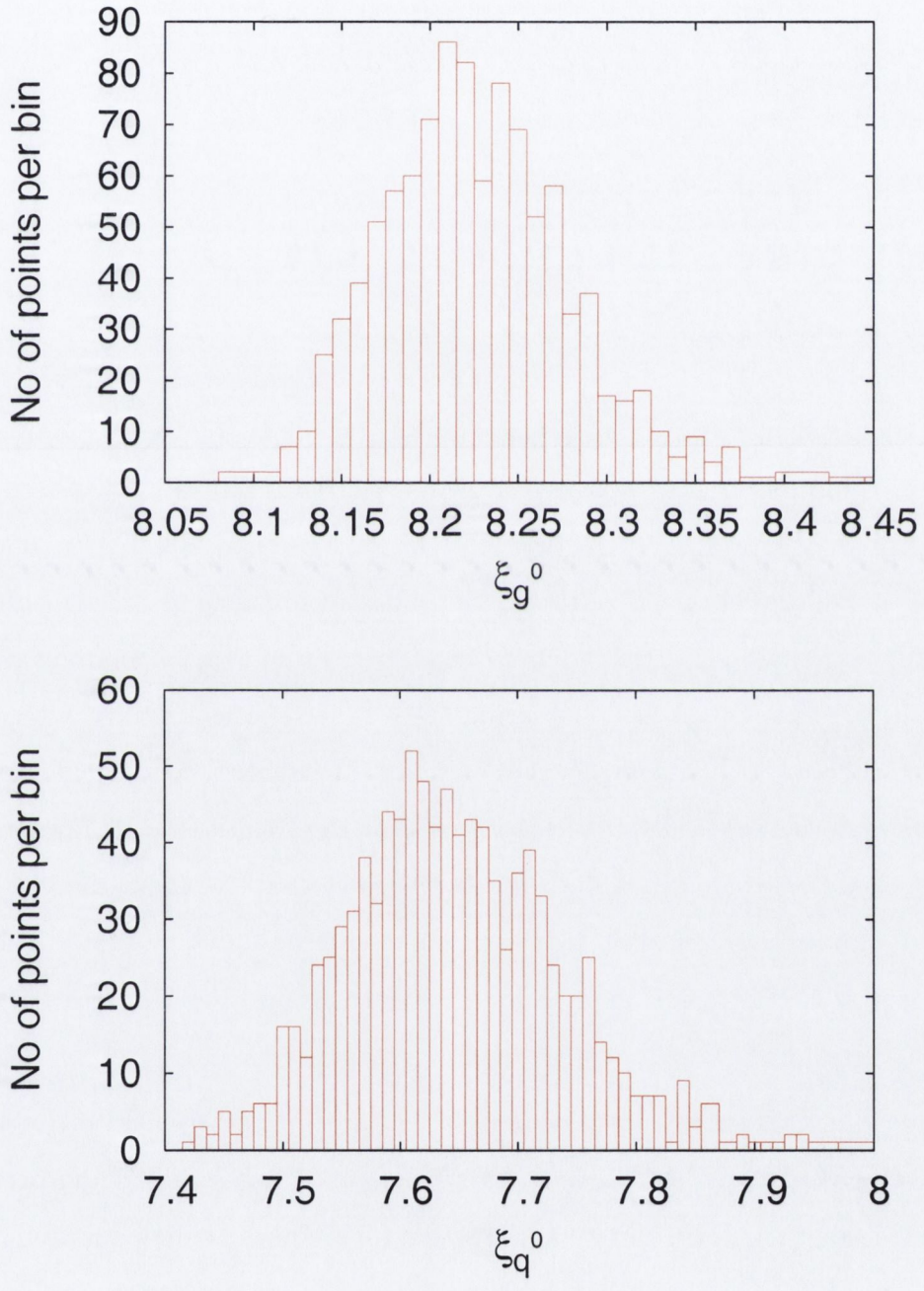

Figure 3-28: Histograms for constrained fit for Fig. 3-26.

Chapter 4

Finite Temperature QCD

One of the most challenging issues in particle physics is to study QCD in extreme conditions. Soon after the discovery of QCD, asymptotic freedom was used to argue that matter at high energy density will be weakly coupled [88]. Thus, under these conditions, hadronic matter will deconfine into an amorphous soup of gluons and quarks. Under the Standard Model of Cosmology, all matter in the universe existed in the form of this Quark Gluon Plasma (QGP) until $\sim 1\mu s$ after the big bang. It is also considered that this state may exist at the extreme conditions found inside the cores of dense neutron stars. Experiments at the Relativistic Heavy Ion Collider (RHIC) have been conducted and have been concluded by many theorists to have provided sufficient evidence as to the existence of the QGP [89, 90]. The ALICE experiment at CERN hopes to provide further probes into the properties of the QGP [91].

Finite temperature studies have developed into a large subfield of Lattice QCD [92]. One reason for this is that phase transitions can only be studied non-perturbatively. Another reason is that the non-perturbative nature of non-Abelian quantum field theories means that the physics is non-perturbative beyond the length scales $1/g^2(T)$, where $g^2(T)$ is the gauge coupling [93]. As such, lattice QCD remains the only tool by which one can hope to make reliable predictions from first principles.

Finite temperature field theory is defined by the Matsubara formalism for finite temperature statistical systems. The temporal coordinate is replaced by $\frac{1}{T}$. This

coordinate is analogous to Euclidean time. The canonical partition function of such a system can be written as

$$Z = \mathrm{Tr} e^{-H/kT} = \int [d\phi] e^{-S[\phi]}, \tag{4.1}$$

where H is the Hamiltonian and $S[\phi] = \int_0^{1/T} dx_4 \int d^3\vec{x} L(\phi, \partial_\mu \phi)$. This is formally equivalent to the path-integral representation of a Euclidean field theory. Following on from this, it can be seen that the temperature will be defined by the temporal extent of the lattice, i.e.

$$T = \frac{1}{N_t a_t}, \tag{4.2}$$

where N_t is the number of timeslices and a_t is the temporal lattice spacing. The extraction of reliable information from numerical data for correlators becomes increasingly difficult with increasing temperature. Noisy temporal correlators are hampered further by the fact that the temporal extent of the system is physically limited by the inverse temperature. This can lead to difficulties in isolating the ground state contributions from the higher state contributions The Maximum Entropy Method [94] has been utilised in extracting the spectral density from such noisy correlators. It should also be noted that a single coloured quark state is allowed as a state with finite action in the deconfined phase and as such a "wraparound" quark propagator may yield a finite expectation value. Due to this contribution, the correlators of certain meson-like operators e.g. charmonia, my be drastically changed after the deconfinement transition [95]. There are two important factors when studying correlators at finite temperature: the granularity of the lattice in the temporal direction and the physical extent of the lattice in the temporal direction. It can be easily seen from Eq. 4.2 that reducing the lattice spacing a_t allows one to simulate at higher temperatures while keeping N_t fixed. Increasing the number of lattice points while keeping the lattice dimension fixed results in a substantial increase in computational cost. Anisotropic lattices allow one to decrease the lattice-spacing in the temporal direction only in order to reduce this cost.

In full QCD with two flavours of dynamical quarks, thermodynamic quantities on

coarse lattices have been found to show a large lattice spacing dependence [96, 97, 98, 99]. Isotropic lattices were used in the quoted studies.

Anisotropic lattices provide an efficient calculation method for thermodynamic quantities.

4.1 Equations of state

The equations of state for the QGP must be determined in order to understand its underlying properties. Perturbation theory is not entirely suitable in the required regime due to the large strong gauge coupling. There are two separate approaches in lattice theory to solving these equations. One method requires the use of *Karsch Coefficients* [100, 102]. The measurement of these coefficients is the subject of this study. The second method is the integral method [101]. This method has a number of disadvantages in that scaling violations exist and it is also computationally expensive. A number of different simulations are required for each quark mass for a given temperature.

The calculation of the energy density ϵ and pressure p is of central importance to the investigation of the phase transition from hadronic matter to the QGP. These observables are defined as derivatives of the partition function Z with respect to temperature, T, and volume, V

$$\epsilon(T) = -\frac{1}{V_s}\left.\frac{\partial \ln Z}{\partial(\frac{1}{T})}\right|_{V_s}, \qquad p(T) = T\left.\frac{\partial \ln Z}{\partial V_s}\right|_{T}. \tag{4.3}$$

Following on from Eq. 4.3, the temperature and volume must be independent variables. This is achieved by keeping the temporal and spatial lattice spacings independent so that

$$V_s = (N_s a_s)^3, \qquad T = \frac{1}{N_t a_t}. \tag{4.4}$$

Using

$$\frac{\partial}{\partial(\frac{1}{T})} = -\frac{\xi}{N_t a_t}\frac{\partial}{\partial \xi} \quad \text{and} \quad \frac{\partial}{\partial V_s} = -\frac{a_s}{3(N_s a_s)^3}\frac{\partial}{\partial a_s} \tag{4.5}$$

and

$$Z = \int d\psi d\bar{\psi} dU e^{-S[U]}, \tag{4.6}$$

Eqs 4.3 can be re-written in the form

$$\epsilon(T) = -\frac{\xi}{N_s^3 N_t a_s^3 a_t} \left\langle \left. \frac{\partial S}{\partial \xi} \right|_{a_s} \right\rangle, \tag{4.7}$$

and

$$p(T) = -\frac{a_s}{3N_s^3 N_t a_s^3 a_t} \left\langle \left. \frac{\partial S}{\partial a_s} \right|_{a_t} \right\rangle, \tag{4.8}$$

where, as usual, $\langle \quad \rangle$ denotes the average over the ensemble. Using the transformation

$$\left. \frac{\partial}{\partial a_s} \right|_{a_t} = \left. \frac{\partial}{\partial a_s} \right|_{\xi} + \frac{1}{a_t} \left. \frac{\partial}{\partial \xi} \right|_{a_s}, \tag{4.9}$$

Eq. 4.8 can be written as

$$\begin{aligned} p(T) &= -\frac{\xi}{3N_s^3 N_t a_s^3 a_t} \left\langle \left. \frac{\partial S}{\partial \xi} \right|_{a_s} \right\rangle - \frac{a_s}{3N_s^3 N_t a_s^3 a_t} \left\langle \left. \frac{\partial S}{\partial a_s} \right|_{\xi} \right\rangle \\ &= \frac{\epsilon(T)}{3} - \frac{a_s}{3N_s^3 N_t a_s^3 a_t} \left\langle \left. \frac{\partial S}{\partial a_s} \right|_{\xi} \right\rangle. \end{aligned} \tag{4.10}$$

Note that although the renormalised anisotropy measured from the pure gauge sector, ξ_g, will coincide with the renormalised quark anisotropy, ξ_q, for any tuned run; in general they will not coincide. Therefore, for the remainder of this study $\xi^+ = \frac{1}{2}(\xi_q + \xi_g)$ is taken as the renormalised anisotropy value. The gluonic and fermionic parts of the action may be studied separately, i.e. $S = S_g + S_q$. The relevant actions from Eqs. 2.57 and 2.53 are repeated here for convenience.

$$\begin{aligned} S_g =& \frac{\beta}{\xi_g^0} \left\{ \frac{5(1+\omega)}{3u_s^4} \Omega_s - \frac{5\omega}{3u_s^8} \Omega_s^{(2t)} - \frac{1}{12u_s^6} \Omega_s^{(R)} \right\} \\ &+ \beta \xi_g^0 \left\{ \frac{4}{3u_s^2 u_t^2} \Omega_t - \frac{1}{12u_s^4 u_t^2} \Omega_t^{(R)} \right\}, \end{aligned} \tag{4.11}$$

and $S_q = \bar{\psi} M \psi$ with

$$
\begin{aligned}
M\psi = & \frac{1}{a_t} \left\{ \left(m_0 a_t + r + \frac{18s}{\xi_q^0} \right) \psi(x) \right. \\
& + \frac{1}{2u_t} \left[(\gamma_0 - r) U_t(x) \psi(x + \hat{t}) - (\gamma_0 + r) U_t^\dagger(x - \hat{t}) \psi(x - \hat{t}) \right] \\
& + \frac{1}{\xi_q^0} \frac{1}{u_s} \sum_i \left[(\frac{2}{3}\gamma_i - 4s) U_i(x) \psi(x + \hat{i}) - (\frac{2}{3}\gamma_i + 4s) U_i^\dagger(x - \hat{i}) \psi(x - \hat{i}) \right. \\
& \left. \left. - \frac{1}{u_s} \left((\frac{1}{12}\gamma_i - s) U_i(x) U_i(x + \hat{i}) \psi(x + 2\hat{i}) - (\frac{1}{12}\gamma_i + s) U_i^\dagger(x - \hat{i}) U_i^\dagger(x - 2\hat{i}) \psi(x - 2\hat{i}) \right) \right] \right]
\end{aligned}
\tag{4.12}
$$

When the fermion fields in the partition function are integrated out explicitly, an "effective" fermion action can be defined as

$$S_f = \ln \det[M], \tag{4.13}$$

or

$$S_f = \mathrm{Tr}[\ln M]. \tag{4.14}$$

The identity

$$\frac{\partial(\mathrm{Tr} \ln[M])}{\partial x} = \mathrm{Tr} M^{-1} \frac{\partial M}{\partial x} \tag{4.15}$$

leads to

$$\frac{\partial S_f}{\partial \xi^+} = \mathrm{Tr}[\frac{\partial M}{\partial \xi^+} M^{-1}], \tag{4.16}$$

and similarly for $\frac{\partial S_f}{\partial a_s}$.

From this point on the input mass is assumed to be the dimensionless quantity $m_0 \equiv m_0 a_t$. u_t is fixed to unity. Working in terms of dimensionless lattice units the derivatives in Eqs 4.7 and 4.8 involve the quantities $\frac{\partial M}{\partial a_s}$, $\frac{\partial M}{\partial \xi^+}$, $\frac{\partial S_g}{\partial \xi^+}$, $\frac{\partial S_g}{\partial a_s}$, which can be

written as

$$\begin{aligned}\frac{\partial M}{\partial a_s}\psi = &\left(\frac{\partial m_0}{\partial a_s} - \frac{18s}{(\xi_q^0)^2}\frac{\partial \xi_q^0}{\partial a_s}\right)\psi(x) \\ &- \frac{1}{(\xi_q^0)^2}\frac{1}{u_s}\frac{\partial \xi_q^0}{\partial a_s}\sum_i \Bigg[(\frac{2}{3}\gamma_i - 4s)U_i(x)\psi(x+\hat{i}) - (\frac{2}{3}\gamma_i + 4s)U_i^\dagger(x-\hat{i})\psi(x-\hat{i}) \\ &-\frac{1}{u_s}\left((\frac{1}{12}\gamma_i - s)U_i(x)U_i(x+\hat{i})\psi(x+2\hat{i}) - (\frac{1}{12}\gamma_i + s)U_i^\dagger(x-\hat{i})U_i^\dagger(x-2\hat{i})\psi(x-2\hat{i})\right)\Bigg] \\ &- \frac{1}{\xi_q^0}\frac{1}{u_s^2}\frac{\partial u_s}{\partial a_s}\sum_i \Bigg[(\frac{2}{3}\gamma_i - 4s)U_i(x)\psi(x+\hat{i}) - (\frac{2}{3}\gamma_i + 4s)U_i^\dagger(x-\hat{i})\psi(x-\hat{i}) \\ &+\frac{2}{u_s}\left((\frac{1}{12}\gamma_i - s)U_i(x)U_i(x+\hat{i})\psi(x+2\hat{i}) - (\frac{1}{12}\gamma_i + s)U_i^\dagger(x-\hat{i})U_i^\dagger(x-2\hat{i})\psi(x-2\hat{i})\right)\Bigg]\end{aligned} \tag{4.17}$$

and

$$\begin{aligned}\frac{\partial M}{\partial \xi^+}\psi = &\left(\frac{\partial m_0}{\partial \xi^+} - \frac{18s}{(\xi_q^0)^2}\frac{\partial \xi_q^0}{\partial \xi^+}\right)\psi(x) \\ &- \frac{1}{(\xi_q^0)^2}\frac{1}{u_s}\frac{\partial \xi_q^0}{\partial \xi^+}\sum_i \Bigg[(\frac{2}{3}\gamma_i - 4s)U_i(x)\psi(x+\hat{i}) - (\frac{2}{3}\gamma_i + 4s)U_i^\dagger(x-\hat{i})\psi(x-\hat{i}) \\ &-\frac{1}{u_s}\left((\frac{1}{12}\gamma_i - s)U_i(x)U_i(x+\hat{i})\psi(x+2\hat{i}) - (\frac{1}{12}\gamma_i + s)U_i^\dagger(x-\hat{i})U_i^\dagger(x-2\hat{i})\psi(x-2\hat{i})\right)\Bigg] \\ &- \frac{1}{\xi_q^0}\frac{1}{u_s^2}\frac{\partial u_s}{\partial \xi^+}\sum_i \Bigg[(\frac{2}{3}\gamma_i - 4s)U_i(x)\psi(x+\hat{i}) - (\frac{2}{3}\gamma_i + 4s)U_i^\dagger(x-\hat{i})\psi(x-\hat{i}) \\ &+\frac{2}{u_s}\left((\frac{1}{12}\gamma_i - s)U_i(x)U_i(x+\hat{i})\psi(x+2\hat{i}) - (\frac{1}{12}\gamma_i + s)U_i^\dagger(x-\hat{i})U_i^\dagger(x-2\hat{i})\psi(x-2\hat{i})\right)\Bigg]\end{aligned} \tag{4.18}$$

Similarly for the gluonic part of the action,

$$\begin{aligned}\frac{\partial S_g}{\partial \xi^+} = &\frac{\partial \xi_g^0}{\partial \xi^+}\left[-\frac{\beta}{(\xi_q^0)^2}\left\{\frac{5(1+\omega)}{3u_s^4}\Omega_s - \frac{5\omega}{3u_s^8}\Omega_s^{(2t)} - \frac{1}{12u_s^6}\Omega_s^{(R)}\right\}\right. \\ &\left. + \beta\left\{\frac{4}{3u_s^2}\Omega_t - \frac{1}{12u_s^4}\Omega_t^{(R)}\right\}\right] \\ &- \frac{\partial u_s}{\partial \xi^+}\left[\frac{\beta}{\xi_g^0}\left\{\frac{20(1+\omega)}{3u_s^5}\Omega_s - \frac{40\omega}{3u_s^9}\Omega_s^{(2t)} - \frac{1}{2u_s^7}\Omega_s^{(R)}\right\}\right. \\ &\left. + \beta\xi_g^0\left\{\frac{8}{3u_s^3}\Omega_t - \frac{4}{12u_s^5}\Omega_t^{(R)}\right\}\right],\end{aligned} \tag{4.19}$$

and

$$\begin{aligned}\frac{\partial S_g}{\partial a_s} =& \frac{\partial \xi_g^0}{\partial a_s}\left[-\frac{\beta}{(\xi_q^0)^2}\left\{\frac{5(1+\omega)}{3u_s^4}\Omega_s - \frac{5\omega}{3u_s^8}\Omega_s^{(2t)} - \frac{1}{12u_s^6}\Omega_s^{(R)}\right\}\right. \\ &\left. + \beta\left\{\frac{4}{3u_s^2}\Omega_t - \frac{1}{12u_s^4}\Omega_t^{(R)}\right\}\right] \\ &- \frac{\partial u_s}{\partial a_s}\left[\frac{\beta}{\xi_g^0}\left\{\frac{20(1+\omega)}{3u_s^5}\Omega_s - \frac{40\omega}{3u_s^9}\Omega_s^{(2t)} - \frac{1}{2u_s^7}\Omega_s^{(R)}\right\}\right. \\ &\left. + \beta\xi_g^0\left\{\frac{8}{3u_s^3}\Omega_t - \frac{4}{12u_s^5}\Omega_t^{(R)}\right\}\right].\end{aligned} \tag{4.20}$$

The coefficients, $\{\frac{\partial \xi_q^0}{\partial \xi^+}, \frac{\partial \xi_q^0}{\partial a_s}, \frac{\partial \xi_g^0}{\partial \xi^+}, \frac{\partial \xi_g^0}{\partial a_s}, \frac{\partial m_0}{\partial \xi^+}, \frac{\partial m_0}{\partial a_s}, \frac{\partial u_s}{\partial \xi^+}, \frac{\partial u_s}{\partial a_s}\}$, must be measured in order to determine the pressure and energy density of the system. These are the *Karsch Coefficients.*

4.2 Determination of lattice spacings

The Karsch coefficients contain terms which are derivatives of input quantities with respect to the measured spatial lattice spacing. Therefore it is necessary to determine the lattice spacing for all of the simulations. Two different methods were used. In the following sections a description of both methods used are presented. A number of tables and figures are presented in this chapter to assist in the explanation of the steps involved. The remainder of the relevant tables and figures are presented in Appendix B.

4.2.1 Interquark potential

The static $q\bar{q}$ potential can in principle be determined by calculating the limit [17]

$$V(R) = -\lim_{T\to\infty}\left[\frac{1}{T}\ln W(R,T)\right], \tag{4.21}$$

where $W(R,T)$ is the expectation value of the Wilson loop with spatial and temporal extension R and T respectively. The relationship between Wilson loops and the

ground state potential $V(R)$ can be written as

$$W(R,T) = C(R)e^{-V(R)T} + \text{“excited state contributions”}, \tag{4.22}$$

where $C(R)$ is the overlap with the “ground state”. The static potential can be obtained from

$$a_t V(R) = \lim_{T\to\infty} ln \frac{\langle W(R,T)\rangle}{\langle W(R,T+1)\rangle}, \tag{4.23}$$

where T is selected as the smallest time on which the excited states become negligible. Alternatively, a single exponential fit of the form

$$W(R,T) = Ae^{-Bt}, \tag{4.24}$$

can be made to the data across a number of timeslices order to extract the parameter $B \approx a_t V(x,t)$.

4.2.2 Cornell Potential

A first attempt was made to determine the lattice spacing via a fit to the static interquark potential. This phenomenologically QCD-motivated form of the potential consists of a $\frac{1}{R}$ term which is due to to the potential induced by one-gluon exchange between the quark and the anti-quark and a linear R term which is the confinement part of the potential. This *Cornell Potential* [103] can be written as

$$V(R) = \frac{\alpha}{r} + \sigma r + V_0. \tag{4.25}$$

Lattice artifacts in the potential due to the difference of the one-gluon exchange on the lattice and in the continuum are corrected by subtracting a term proportional to

$$\delta\hat{V}(\hat{R}) = \left(\left[\frac{1}{\hat{R}}\right] - \frac{1}{\hat{R}}\right). \tag{4.26}$$

Where $\left[\frac{1}{\hat{R}}\right]$ denotes the lattice one gluon exchange extrapolated to infinite volume [104, 105, 106]. Alternate proposals exist for potential models which incorporate

asymptotic freedom and linear quark confinement such as the Richardson Potential [107].

For the case of partially-quenched QCD, the interquark potential is "screened" by pair production. String breaking will occur when the potential energy needed to separate the quarks exceeds the energy needed for the production of a quark-antiquark pair. One would thus expect a flattening out of the measured potential for larger separation.

Using quenched data, one can obtain an upper bound for which string breaking should be observable [108]. A comparison of interquark potential for quenched vs unquenched QCD can be seen in [109]. No evidence for string breaking was seen in that study for a volume of $V \approx (1.5fm)^2$. The first observation of string breaking in 4-dimensional lattice QCD was observed in [113] from the energy level crossing [114]. [115] measured the distance for the string breaking to occur to be $a \approx 1.25fm$.

Thus, a fit of $V(R)$ to Eq. 4.25 from a lattice simulation with dynamical fermions will be less accurate. Finite spacing effects will affect the measurement of $V(R)$ for small values of R and string breaking will affect measurements for large values of R. The choice of fit range will have a significant effect on the resulting measured fit parameters. For the purpose of the "rough" determination of the lattice spacing which was done for the Tuning Project (Chapter 3), a linear fit to potential was made for large R and the slope was identified with the string tension.

Determining a_s using the Cornell potential

It is possible to measure a value for a_s from a fit of $V(R)$ to the Cornell potential by determining $a_s V(R)$ for a range of values of R and performing a fit to the resulting values. The quantity $a_t V(R)$ from equation 4.23 is simply multiplied by the anisotropy value ξ_g. The coefficient of the r term in Eq. 4.25 is called the "string tension" and this is the term used to set the scale from the potential.The standard value is generally taken to be $\sigma_{\text{standard}} = (440\text{MeV})^2$. The lattice version of Eq. 4.25 is given by

$$a_s V(R) = a_s \frac{\alpha}{\hat{R}} + \sigma \hat{R} + a_s V_0. \tag{4.27}$$

with $\tilde{\sigma} = a_s^2\sigma$ and $\hat{R} = \frac{r}{a_s}$. The lattice spacing can then be determined from

$$a_s = \frac{\sqrt{\tilde{\sigma}}}{0.44}\text{GeV}^{-1}, \tag{4.28}$$

and

$$1\text{GeV} = \frac{1}{0.197 \times 10^{-15}}\text{m}. \tag{4.29}$$

Steps involved in measuring Cornell potential

The first step in determining $V(R)$ consists of measuring the expectation value of Wilson loops in the $R-t$ plane. $V(R,T)$ was then extracted from a plot of $W(R,t)$ against t as described in Eq. 4.24. Fig. 4-1 shows a log plot of $W(R,t)$ for $R = 3$ for Run 6. It also shows the corresponding "effective mass" plot for $V(R,t)$. Note again that the $V(R,t)$ in practice is not determined from the effective mass plot but is fitted directly to $W(R,t)$. From Eq. 4.22 it can be seen that $a_t V(R)$ can be taken to be $V(R,t)$ in the large t limit. Sliding window fits were again employed in order to determine the optimum fit range. Fig. 4-2 shows an example of such a sliding window fit and the corresponding $\chi^2/N_{\text{d.f}}$. It can be seen from the plots in Fig. 4-1 that the signal becomes noisy out near the centre of the lattice. For this reason, a number of different values of t_{max} were tried. Fig. 4-3 shows sliding window fits for a fit to $V(R,t)$ for a range of different values of t_{max} for Run 7 with $R = 4$. Fig. 4-4 shows the corresponding $\chi^2/N_{\text{d.f}}$ for the fits. This procedure is repeated for values of $R = 1-7$. For the purpose of illustration, a set of sliding window plots for Run 1 with $t_{\text{max}} = 40$ for values of $R = 1-6$ are shown in Fig. 4-5. Table 4.2.2 shows the chosen values of t_{min} and t_{max} which were used for all of the Runs. The resulting values of $V(R)$ were plotted against R; an example is shown in Fig. 4-6. Finally, these plots of $V(R)$ are fitted against the Cornell potential $V(R)$, Eq. 4.25. All possible values of R_{min} and R_{max} are considered. The resulting fit parameters for Run 1 are given in Table 4.2 and the modelled data are also plotted in Fig. 4-6 for comparison with the measured data. Plots and tables for the other Runs are included in Appendix B.

Taking for example, Run 1, and assuming $[1,5]$ to be an appropriate fit-range,

R	t_{min}	t_{max}
1	15	35
2	15	30
3	12	25
4	10	25
5	9	20
6	10	20
7	10	15

Table 4.1: This table shows the fit ranges that are used for determining $V(R)$ from $W(R,t)$.

the measured lattice string tension $\tilde{\sigma} = 0.16480(13)$. This corresponds to a lattice spacing of $a_s = 0.18176(16)$ fm.

The values for the potential obtained during these simulations did not vary significantly over the bootstraps. The result of this was that the error bars used in the Cornell fit were extremely small and the variance of the fit parameters did not vary across the bootstraps. This led to the large χ^2 values obtained in the fits and also to the small statistical errors quoted in the tables. It is also generally accepted that fitting the measured potential to the Cornell potential is not the most accurate method for determining the lattice spacing. It can also be seen again from Table 4.2 that the measured value for $\tilde{\sigma}$ was not stable and depended largely on the values of R_{max} and R_{min} chosen. It was decided to use a more reliable method to set the lattice spacings.

4.2.3 Sommer Scale

An alternate way to determine the scale of a lattice simulation was introduced in [116]. This method involves using the force $F(r)$ between static quarks at intermediate distances, r to define a hadronic scale r_0. The implicit equation used to do this is determined by

$$r^2 \, F(r)|_{r=r(c)} = c. \tag{4.30}$$

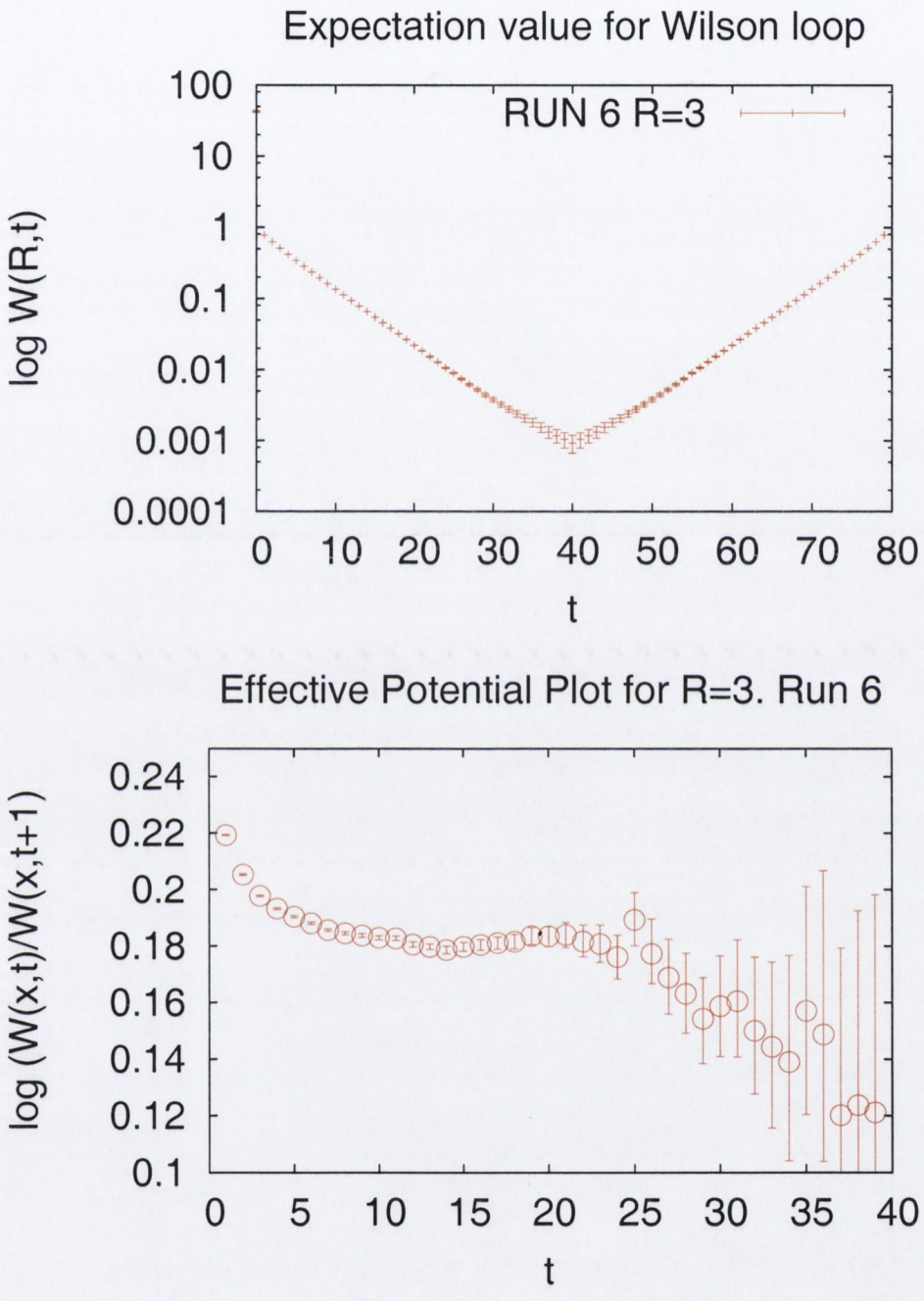

Figure 4-1: This figure shows the first two steps involved in measuring the interquark potential. This is from Run 6. The spatial lattice spacing is $R = 3$. The top plot shows the expectation value of the Wilson loop $W(x,t)$ averaged over the 1000 bootstrapped sets of 250 configurations. The bottom plot shows the value $V(x,t)$ obtained by taking the log of the ratio of $W(x,t)$ on adjacent timeslices. Two more plots showing the next stage of the procedure are given in Fig. 4-2.

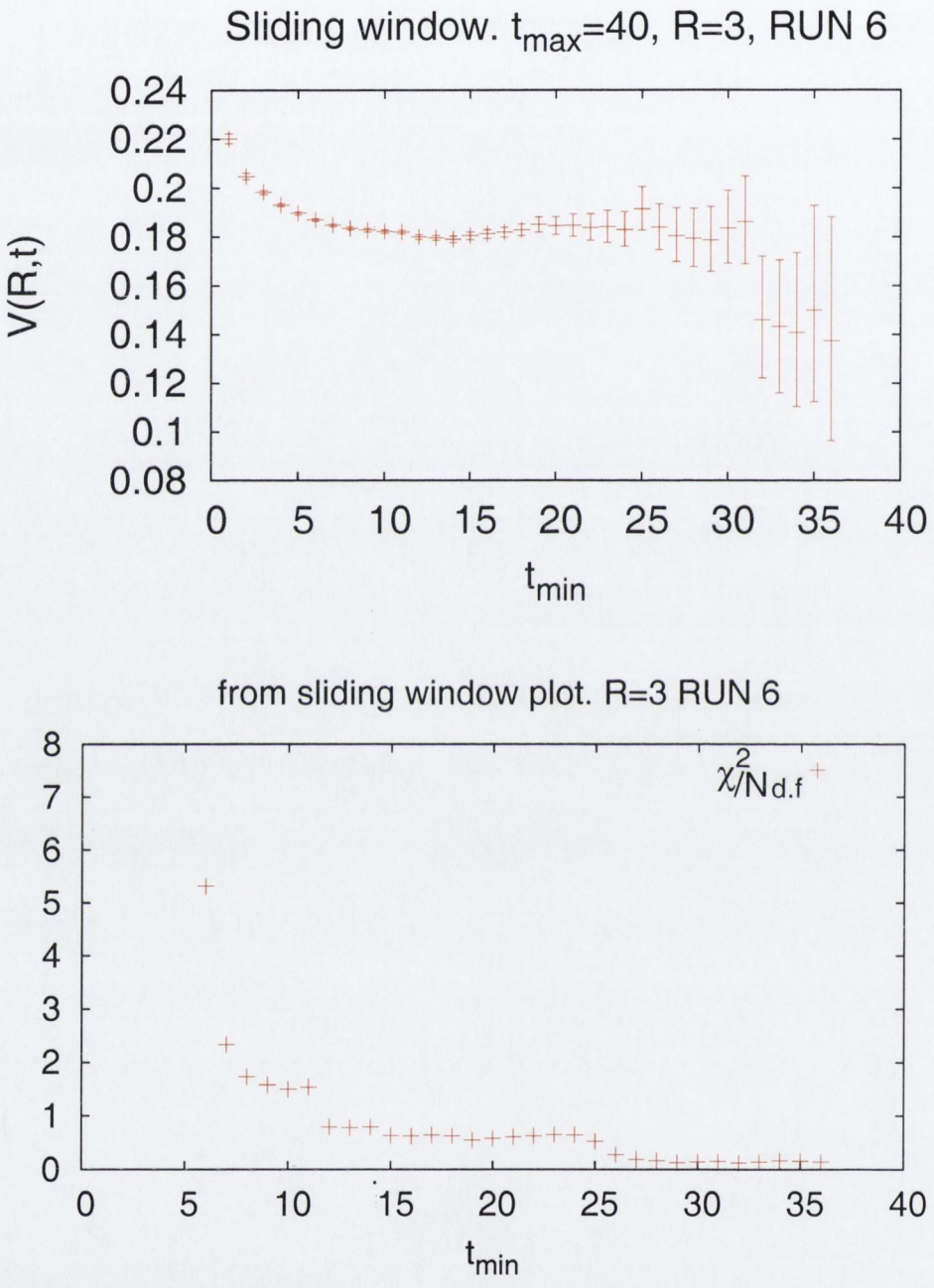

Figure 4-2: This figure shows the next two steps involved in measuring the interquark potential. These plots are a continuation of the two plots presented in Fig. 4-1. The top plot is a sliding window plot, fitting $W(x,t)$ to a single exponential between t_{min} and $t_{max} = 40$. The bottom plot shows the value for the $\chi^2/N_{\text{d.f}}$ for the corresponding fit.

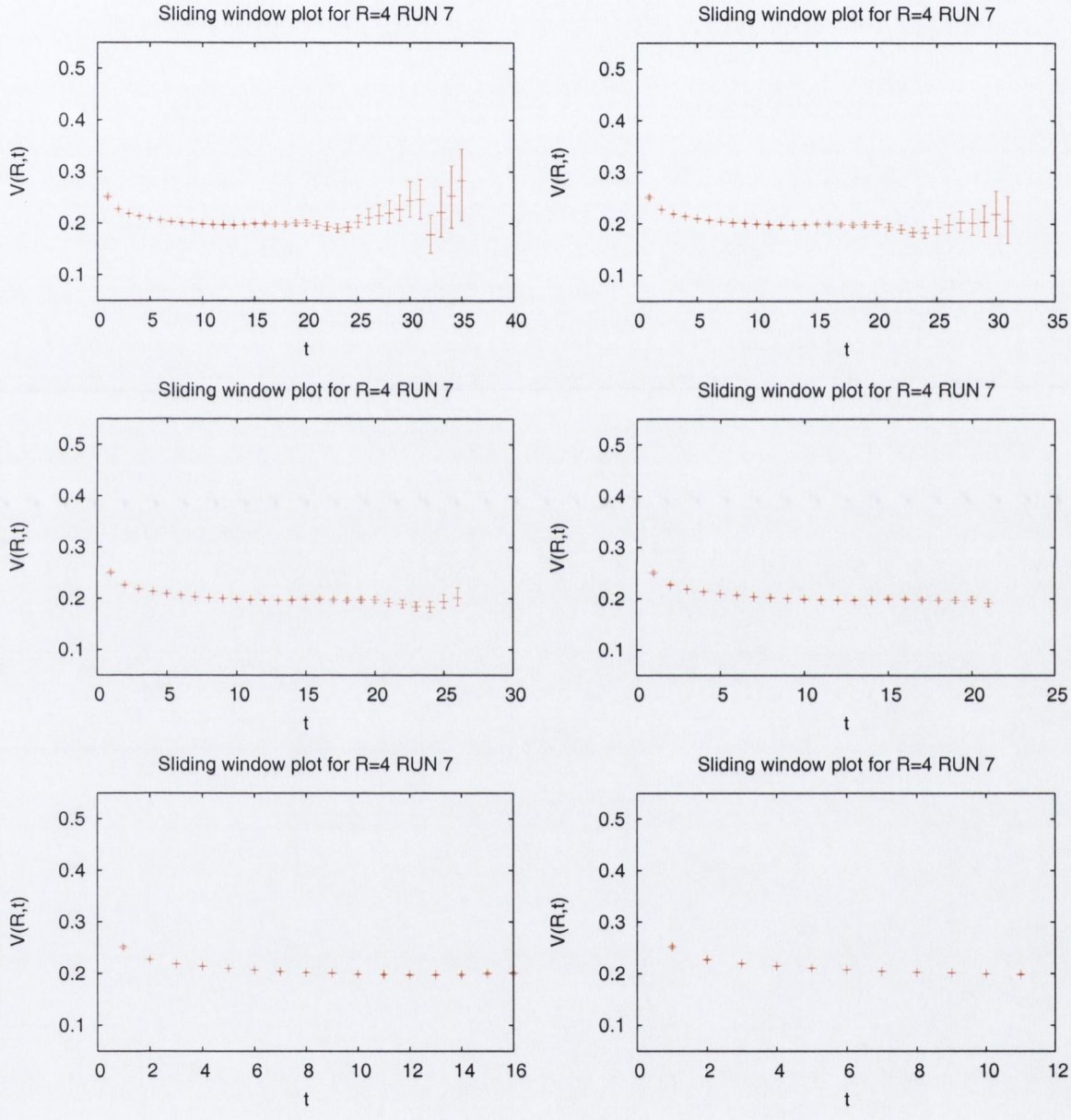

Figure 4-3: Plots comparing the effect of choosing a different value of $t_{\max}$. Above are shown sliding window fits for Run 7 for a range of different values of $t_{max} = \{40, 35, 30, 25, 25, 20, 15\}$. The corresponding $\chi^2/N_{\text{d.f}}$ values are shown in Fig. 4-4.

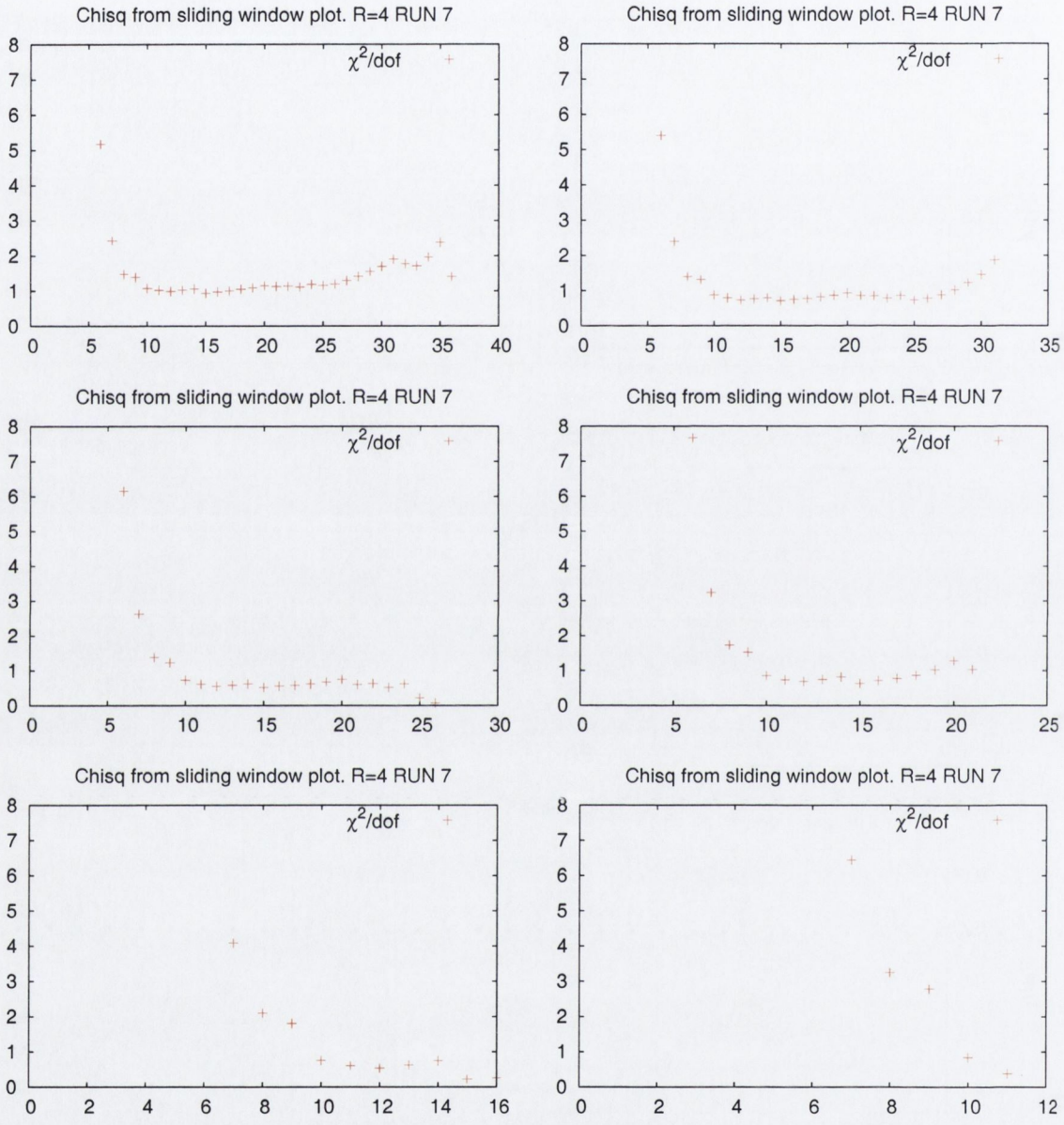

Figure 4-4: These plots show the $\chi^2/N_{\mathrm{d.f}}$ values for the fits in the corresponding plots in Fig. 4-3.

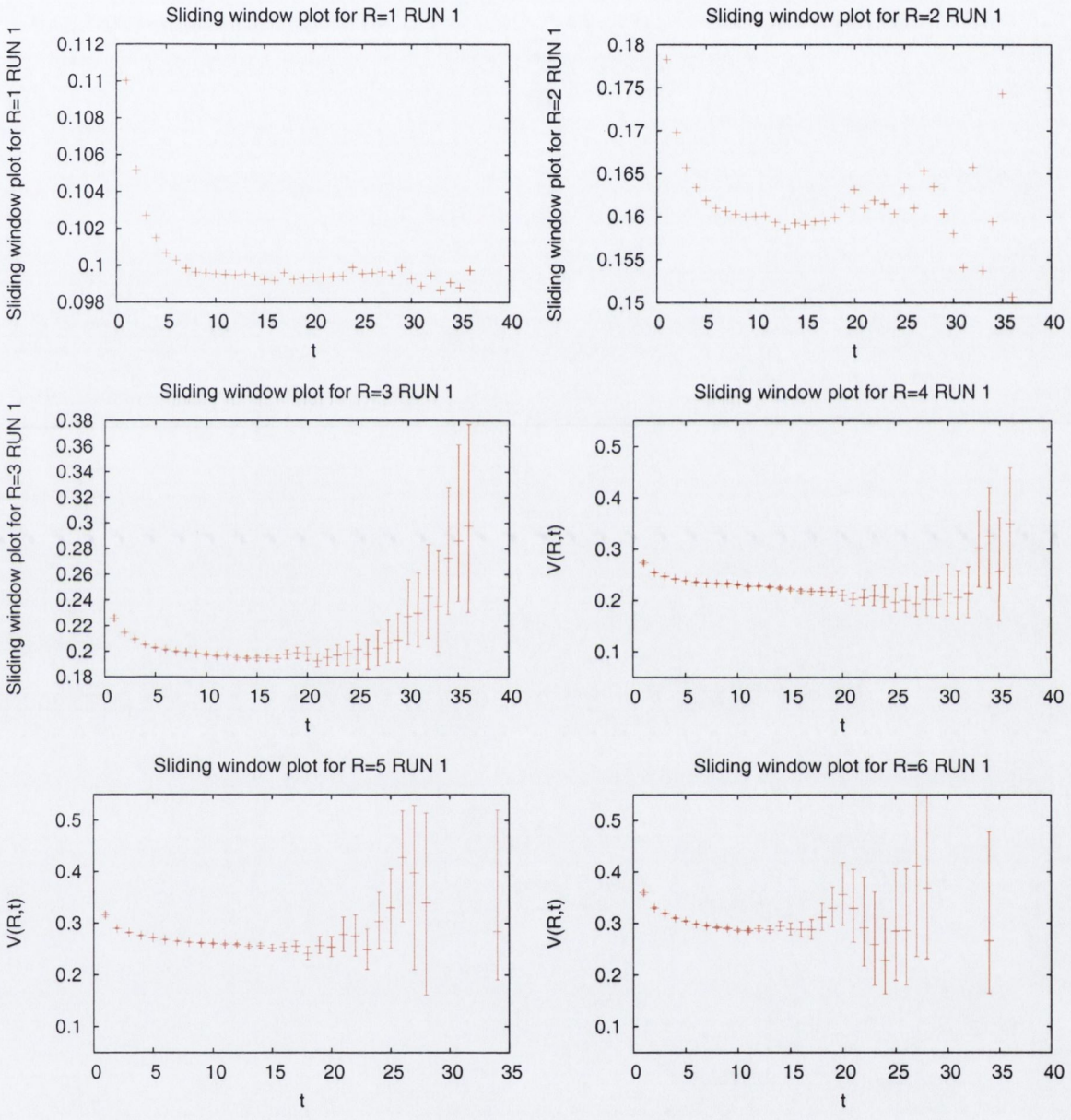

Figure 4-5: A comparison of interquark potential measurements for different spatial separations. These sliding window plots show the effective potential $V(R,t)$ extracted by fitting $W(R,t)$ to a single exponential. For each plot, the x-axis denotes the value of t_{min} used in the fit. T_{max} is set to 40 for all of the plots. The plot $R = 7$ is not included. The spatial separation for each plot is included in the title of that plot.

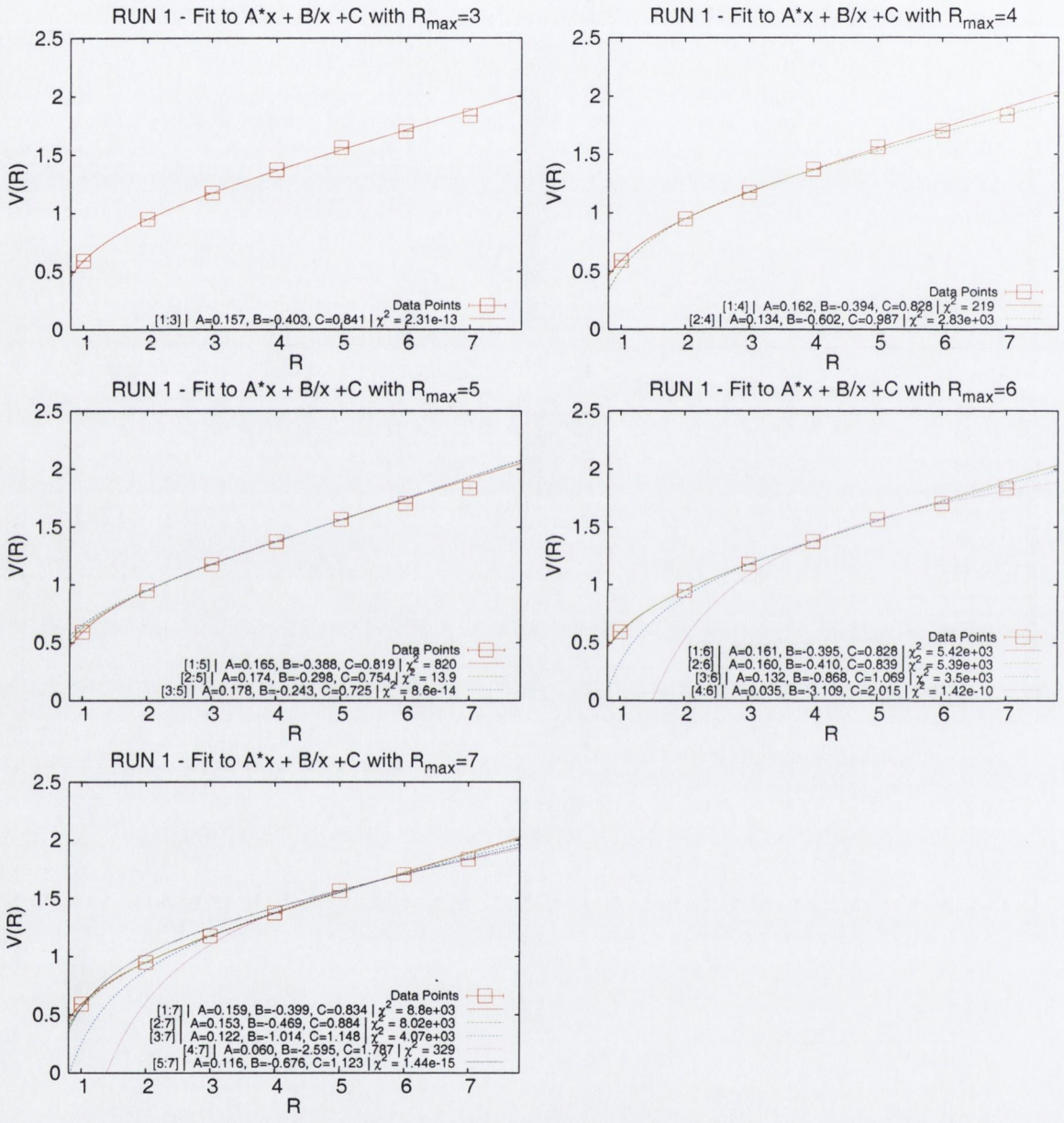

Figure 4-6: Fits to the Cornell Potential for Run 1 for all values of $R_{\max}$ and $R_{\min}$. The resulting measured fit parameters can be found in Tab. 4.2. Note that Run 1 is chosen merely for illustrative purposes. Run 7 was the final tuned run.

Range	A	B	C	χ^2/dof
[1:7]	0.15955 (0.00006)	-0.39860 (0.00011)	0.83424 (0.00017)	8.80e+03
[2:7]	0.15285 (0.00024)	-0.46687 (0.00014)	0.88178 (0.00044)	8.02e+03
[3:7]	0.12166 (0.00026)	-1.02717 (0.00113)	1.15409 (0.00238)	4.07e+03
[4:7]	0.05828 (0.00065)	-2.62498 (0.00143)	1.80018 (0.00778)	3.29e+02
[5:7]	0.11736 (0.00143)	-0.61256 (0.00524)	1.10321 (0.00286)	1.44e-15
[1:6]	0.16155 (0.00002)	-0.39459 (0.00004)	0.82823 (0.00006)	5.42e+03
[2:6]	0.16031 (0.00027)	-0.40674 (0.00094)	0.83679 (0.00075)	5.39e+03
[3:6]	0.13181 (0.00091)	-0.88324 (0.01146)	1.07595 (0.00869)	3.50e+03
[4:6]	0.03229 (0.00002)	-3.16467 (0.01175)	2.03898 (0.00769)	1.42e-10
[1:5]	0.16480 (0.00013)	-0.38810 (0.00026)	0.81848 (0.00039)	8.20e+02
[2:5]	0.17521 (0.00012)	-0.29204 (0.00017)	0.74963 (0.00045)	1.39e+01
[3:5]	0.17820 (0.00018)	-0.24664 (0.00681)	0.72586 (0.00349)	8.60e-14
[1:4]	0.16170 (0.00006)	-0.39430 (0.00011)	0.82779 (0.00017)	2.19e+02
[2:4]	0.13450 (0.00018)	-0.59844 (0.00004)	0.98425 (0.00054)	2.83e+03
[1:3]	0.15687 (0.00000)	-0.40395 (0.00001)	0.84227 (0.00001)	2.31e-13

Table 4.2: Fit parameters for the fit to the Cornell potential for RUN 1. The first column shows the relevant fit range. The central columns show the fit parameters from a fit to $Ax + B/x + C$. The figures in brackets are statistical errors obtained using a 68% confidence interval over the set of 1000 bootstraps. The final column shows the χ^2 per degree of freedom for the best fit. The relevent plots are those in Fig. 4-6.

The force $F(R)$ can be determined from the potential by the discretisation of the derivative of the potential with respect to distance in the standard way i.e.

$$F(r) = -\frac{dV(r)}{dR}. \tag{4.31}$$

Forward, backward and central-difference approximations were measured. The central-difference approximation was taken as the most accurate estimation. The values for the forward and backward difference provide a measure of the systematic error inherent in the discretisation.

It can be determined from phenomenological potential models that $r_0 = r(1.65)$ for Eq. 4.30 above corresponds to a value of $r = 0.49$ fm. Other values of $r(c)$ have been proposed. For example, for the case of short distances, a value of $r_1 = r(0.65)$ was introduced by [117] and it was determined that using this value resulted in $\frac{r_1}{r_0} = 0.51$. However, as seen in Fig. 4-7, using r_0 would be a more appropriate choice as it involved interpolation for each of the finite-difference schemes whereas r_1 would necessitate an extrapolation for the backward and central difference approximations.

The plots for the measurements of $F(R)$ for each of the runs are presented in Fig. 4-7. The resulting interpolations to $r(c)$ give rise to determinations of the lattice spacings given in Table 4.3. The determination of the spacing by this method agrees with a previous measurement from [118]. That study used the preliminary tuned point corresponding to Run 6 and determined the lattice spacing to be $a_s \sim 0.17$ fm from the (1P-1S) splitting in charmonium. This corresponds to a value of 0.17(1) fm determined using the Sommer scale with a central difference approximation for $F(R)$. The errors quoted are determined from the values obtained when using the forward and backward difference discretisations.

4.2.4 Karsch Coefficients

The Karsch coefficients presented above in Section 4.1 are simply the partial derivatives of the action input parameters with respect to the renormalised anisotropy and spatial lattice spacing. Attempts have been made to calculate these coefficients per-

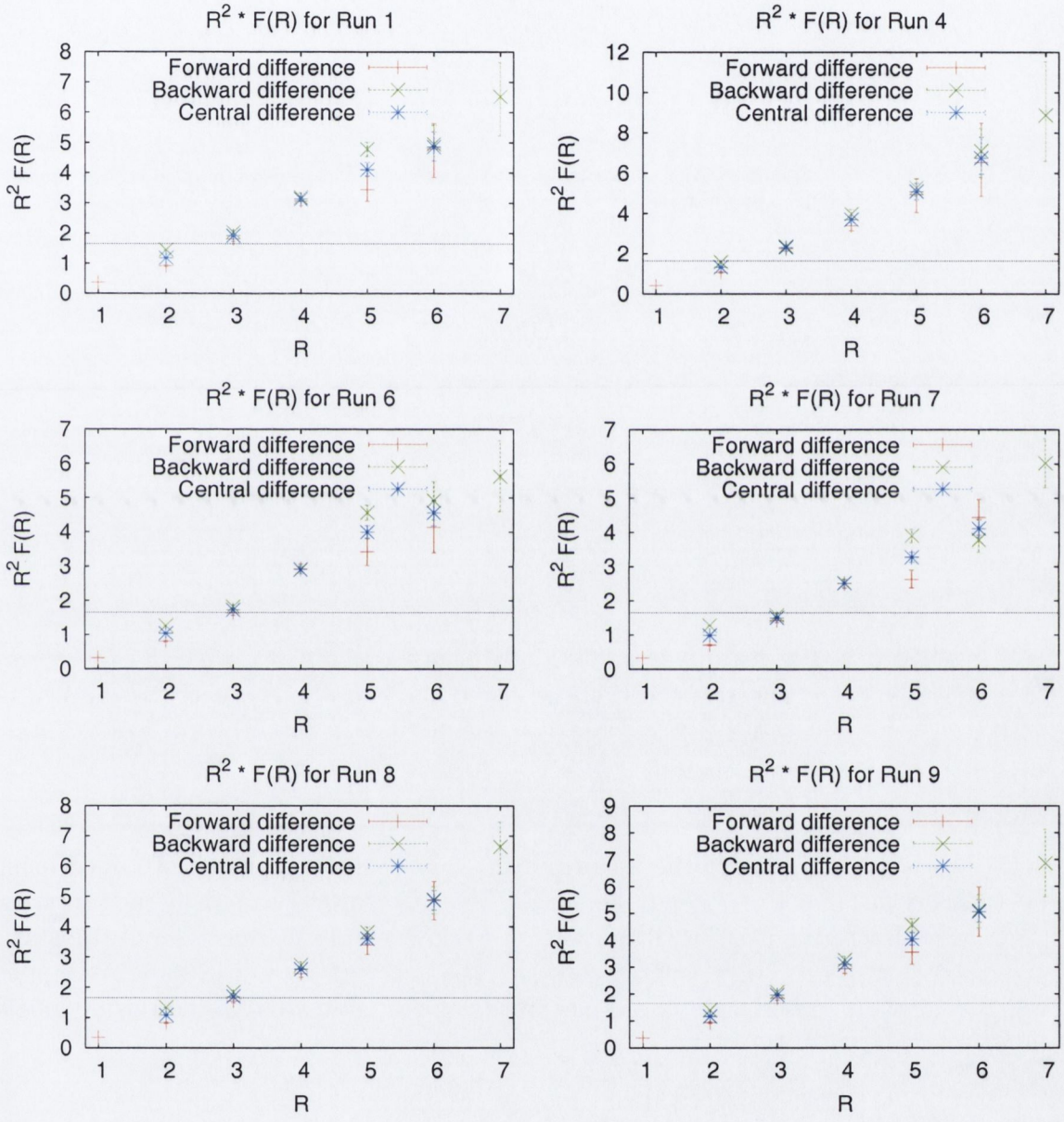

Figure 4-7: These plots show $R^2 \times F(R)$ vs R for each of the runs. This data was used in order to set the scale using the Sommer parameter as in Sec. 4.2.3. The horizontal line shows where $R^2 \times F(R) = 1.65$

		Average	Median	Low	High
Run 1	Forward	0.171891	0.172228	0.167275	0.176393
	Backward	0.206549	0.206900	0.203044	0.210080
	Central	0.184393	0.184468	0.181959	0.186834
Run 4	Forward	0.194474	0.194823	0.190801	0.198158
	Backward	0.231735	0.231887	0.230410	0.233135
	Central	0.208027	0.208045	0.205795	0.210268
Run 6	Forward	0.161442	0.161640	0.156932	0.166007
	Backward	0.180817	0.181129	0.176449	0.185176
	Central	0.168923	0.168953	0.166396	0.171529
Run 7	Forward	0.146766	0.147003	0.141161	0.152151
	Backward	0.148068	0.148860	0.138544	0.157131
	Central	0.147536	0.147560	0.144190	0.150779
Run 8	Forward	0.154058	0.154249	0.148937	0.159312
	Backward	0.183588	0.184044	0.178833	0.188434
	Central	0.165274	0.165320	0.162601	0.167797
Run 9	Forward	0.173983	0.174267	0.169978	0.178169
	Backward	0.202687	0.202948	0.199851	0.205453
	Central	0.185282	0.185376	0.183336	0.187115

Table 4.3: This table shows the measurements of the lattice spacing obtained using the Sommer parameter r_0 to set the scale. The value of force used in each interpolation were determined by forward, backward and central differences from the static interquark potential. The measurements are obtained over a set of 1000 bootstrapped configurations. The high and low values in the above table are obtained using a 68% confidence interval.

turbatively [110, 111]. The perturbative coefficients are known to lead to pathological results such as negative pressure and a non-vanishing pressure gap at the deconfining phase in $SU(3)$ gauge theory [119]. Non-perturbative calculations have proved difficult [112]. A study by [122] attempted their measurement for the case of staggered fermions using a similar procedure to one of those used in this study. [119] attempted to compute them from a precise measurement of the finite temperature deconfining transition curve.

This study attempted a non-perturbative determination of the coefficients. Two approaches are employed in the measurement of these coefficients. In the first approach it is assumed that the action input parameters are linearly dependent on the measured output parameters. Identifying this assumption with a Taylor expansion shows that the fitted parameters for a linear fit are the required Karsch coefficients. In the second approach, the measured output parameters are taken to be linearly dependent on the input parameters. A matrix is defined from the resulting fit parameters and this matrix is then inverted in order to determine the Karsch coefficients. The notation used in the following sections is repeated here for clarity.

Notation:

The input parameters which are varied between the different simulations are the gluon anisotropy ξ_g^0, the quark anisotropy ξ_q^0, the dimensionless bare quark mass m_0 and the spatial plaquette u_s. After each simulation a number of output parameters are measured. The output gluon anisotropy, ξ_g, is determined from the "sideways potential" (Sec. 3.3.1). The output quark anisotropy, ξ_q, is determined from the pseudoscalar dispersion relation as explained in (Sec. 3.3.2). The lattice spacing, a_s, is determined using the Sommer Scale (Sec. 4.2.3. The pion and rho rest-masses, m_π

Run	ξ_q^0	ξ_g^0	u_s	m_0	β
1	6.0	8.0	0.32	-0.057	1.513
4	8.72	6.65	0.32	-0.057	1.544
5	8.83	7.44	0.32	-0.057	1.522
6	7.52	8.06	0.32	-0.057	1.514
7	7.43	8.42	0.32	-0.057	1.508
8	7.43	8.42	0.32	-0.05	1.514
9	7.43	8.42	0.31	-0.057	1.458

Table 4.4: This table shows the input parameters for the quark and gluon actions for each of the runs used in the determination of the Karsch coefficients.

and m_ρ, are also determined. A number of composite variables are defined as:

$$\xi^+ = \frac{\xi_q + \xi_g}{2}, \tag{4.32}$$

$$\xi^- = \frac{\xi_g - \xi_q}{2}, \tag{4.33}$$

$$\mathrm{M} = \left(\frac{m_\pi}{m_\rho}\right)^2. \tag{4.34}$$

M is chosen rather than $\frac{m_\pi}{m_\rho}$ as it is expected to be linearly related to the quark mass [120].

Simulation Details

250 gauge configurations were generated for each Run. The input parameters for each Run are given in Table 4.4.

4.3 Method 1

The first attempt considers the action input parameters, $\{\xi_q^0, \xi_g^0, u_s, m_0\}$, as a linear Taylor expansion of the renormalised measured parameters, $\{\xi^+, a_s, \xi^-, \mathrm{M}\}$. This

method is analogous to the one used in [121, 122]. This leads to the equations

$$\Delta\xi_q^0 = \frac{\partial\xi_q^0}{\partial\xi^+}\Delta\xi^+ + \frac{\partial\xi_q^0}{\partial a_s}\Delta a_s + \frac{\partial\xi_q^0}{\partial\xi^-}\Delta\xi^- + \frac{\partial\xi_q^0}{\partial \mathrm{M}}\Delta\mathrm{M}, \tag{4.35}$$

$$\Delta\xi_g^0 = \frac{\partial\xi_g^0}{\partial\xi^+}\Delta\xi^+ + \frac{\partial\xi_g^0}{\partial a_s}\Delta a_s + \frac{\partial\xi_g^0}{\partial\xi^-}\Delta\xi^- + \frac{\partial\xi_g^0}{\partial \mathrm{M}}\Delta\mathrm{M}, \tag{4.36}$$

$$\Delta u_s = \frac{\partial u_s}{\partial\xi^+}\Delta\xi^+ + \frac{\partial u_s}{\partial a_s}\Delta a_s + \frac{\partial u_s}{\partial\xi^-}\Delta\xi^- + \frac{\partial u_s}{\partial \mathrm{M}}\Delta\mathrm{M}, \tag{4.37}$$

$$\Delta m_0 = \frac{\partial m_0}{\partial\xi^+}\Delta\xi^+ + \frac{\partial m_0}{\partial a_s}\Delta a_s + \frac{\partial m_0}{\partial\xi^-}\Delta\xi^- + \frac{\partial m_0}{\partial \mathrm{M}}\Delta\mathrm{M}. \tag{4.38}$$

The quantities $\frac{\partial\xi_q^0}{\partial\xi^+}$ etc., which are the required Karsch Coefficients, can thus be obtained from a simple 5d hyper-planar fit

$$Z = c_1x_1 + c_2x_2 + c_3x_3 + c_4x_4 + c_5. \tag{4.39}$$

Four equations are needed order to perform a fit such as Eq. 4.39 meaning that at least five separate runs are needed to fit to each of the Eqs. 4.35 - 4.38 above. With more than five runs, a constrained fit can be performed. A χ^2 minimisation is attempted using the Levenberg-Marquardt procedure as described in Sec. 2.11.1. However, the standard procedure cannot be followed exactly as the variance on each run is not known beforehand. In order to work around this, an iterative procedure is employed in which the initial values for the variances are determined randomly. The fitting procedure is followed as normal and the fit parameters are determined. The fitted parameters are then inserted back into the original equations and a new estimate for the variances are determined. This procedure is then repeated until the results for the fit parameters converge. The variance for each run determined from the "best fit" values and the resulting covariance matrix is used for each of the individual 1000 bootstraps. A 68% confidence interval is used over the bootstraps in order to determine the errors.

4.4 Method 2

Considering the measured renormalised values as a Taylor expansion of the input quantities $\xi_q^0, \xi_g^0, u_s, m_0$ leads to

$$\Delta\xi^+ = \frac{\partial\xi^+}{\partial\xi_q^0}\Delta\xi_q^0 + \frac{\partial\xi^+}{\partial\xi_g^0}\Delta\xi_g^0 + \frac{\partial\xi^+}{\partial u_s}\Delta u_s + \frac{\partial\xi^+}{\partial m_0}\Delta m_0, \tag{4.40}$$

$$\Delta a_s = \frac{\partial a_s}{\partial\xi_q^0}\Delta\xi_q^0 + \frac{\partial a_s}{\partial\xi_g^0}\Delta\xi_g^0 + \frac{\partial a_s}{\partial u_s}\Delta u_s + \frac{\partial a_s}{\partial m_0}\Delta m_0, \tag{4.41}$$

$$\Delta\xi^- = \frac{\partial\xi^-}{\partial\xi_q^0}\Delta\xi_q^0 + \frac{\partial\xi^-}{\partial\xi_g^0}\Delta\xi_g^0 + \frac{\partial\xi^-}{\partial u_s}\Delta u_s + \frac{\partial\xi^-}{\partial m_0}\Delta m_0, \tag{4.42}$$

$$\Delta\mathrm{M} = \frac{\partial\mathrm{M}}{\partial\xi_q^0}\Delta\xi_q^0 + \frac{\partial\mathrm{M}}{\partial\xi_g^0}\Delta\xi_g^0 + \frac{\partial\mathrm{M}}{\partial u_s}\Delta u_s + \frac{\partial\mathrm{M}}{\partial m_0}\Delta m_0. \tag{4.43}$$

These equations can be written in the form of a matrix equation

$$\vec{y} = B\vec{x}, \tag{4.44}$$

with

$$B = \begin{pmatrix} \frac{\partial\xi^+}{\partial\xi_q^0} & \frac{\partial\xi^+}{\partial\xi_g^0} & \frac{\partial\xi^+}{\partial u_s} & \frac{\partial\xi^+}{\partial m_0} \\ \frac{\partial a_s}{\partial\xi_q^0} & \frac{\partial a_s}{\partial\xi_g^0} & \frac{\partial a_s}{\partial u_s} & \frac{\partial a_s}{\partial m_0} \\ \frac{\partial\xi^-}{\partial\xi_q^0} & \frac{\partial\xi^-}{\partial\xi_g^0} & \frac{\partial\xi^-}{\partial u_s} & \frac{\partial\xi^-}{\partial m_0} \\ \frac{\partial\mathrm{M}}{\partial\xi_q^0} & \frac{\partial\mathrm{M}}{\partial\xi_g^0} & \frac{\partial\mathrm{M}}{\partial u_s} & \frac{\partial\mathrm{M}}{\partial m_0} \end{pmatrix}, \tag{4.45}$$

and

$$\vec{y} = \begin{pmatrix} \Delta\xi^+ \\ \Delta a_s \\ \Delta\xi^- \\ \Delta\mathrm{M} \end{pmatrix}, \quad \vec{x} = \begin{pmatrix} \Delta\xi_q^0 \\ \Delta\xi_g^0 \\ \Delta u_s \\ \Delta m_0 \end{pmatrix}. \tag{4.46}$$

The required Karsch coefficients can be determined from the inverse of the above

Run	ξ_q	ξ_g	a_s	$a_t m_\pi$	$a_t m_\rho$
1	$5.54^{+0.05}_{-0.05}$	$5.83^{+0.04}_{-0.04}$	$0.184^{+0.002}_{-0.003}$	$0.1037^{+0.0008}_{-0.0005}$	$0.154^{+0.002}_{-0.002}$
4	$7.08^{+0.04}_{-0.04}$	$5.67^{+0.04}_{-0.04}$	$0.208^{+0.002}_{-0.002}$	$0.0925^{+0.0005}_{-0.0003}$	$0.129^{+0.001}_{-0.001}$
5	$6.95^{+0.08}_{-0.08}$	$5.95^{+0.04}_{-0.04}$	$0.179^{+0.002}_{-0.003}$	$0.0637^{+0.0007}_{-0.0004}$	$0.111^{+0.003}_{-0.003}$
6	$6.21^{+0.10}_{-0.08}$	$5.90^{+0.03}_{-0.03}$	$0.169^{+0.002}_{-0.003}$	$0.0657^{+0.0011}_{-0.0004}$	$0.120^{+0.003}_{-0.002}$
7	$5.78^{+0.04}_{-0.03}$	$6.04^{+0.02}_{-0.02}$	$0.148^{+0.003}_{-0.003}$	$0.067^{+0.003}_{-0.003}$	$0.126^{+0.002}_{-0.002}$
8	$6.42^{+0.04}_{-0.05}$	$6.05^{+0.02}_{-0.02}$	$0.165^{+0.003}_{-0.003}$	$0.0891^{+0.0006}_{-0.0004}$	$0.129^{+0.001}_{-0.001}$
9	$6.26^{+0.05}_{-0.05}$	$6.08^{+0.03}_{-0.03}$	$0.185^{+0.002}_{-0.002}$	$0.0779^{+0.0006}_{-0.0004}$	$0.119^{+0.002}_{-0.002}$

Table 4.5: This table shows the measured quantities which are used for the Karsch fitting procedure. Each quoted value is determined from fitting to the non-bootstrapped data. The error bars are determined from a 68% confidence interval across 1000 bootstraps.

matrix, i.e.

$$B^{-1} = \begin{pmatrix} \frac{\partial \xi_q^0}{\partial \xi^+} & \frac{\partial \xi_q^0}{\partial a_s} & \frac{\partial \xi_q^0}{\partial \xi^-} & \frac{\partial \xi_q^0}{\partial \mathrm{M}} \\ \frac{\partial \xi_g^0}{\partial \xi^+} & \frac{\partial \xi_g^0}{\partial a_s} & \frac{\partial \xi_g^0}{\partial \xi^-} & \frac{\partial \xi_g^0}{\partial \mathrm{M}} \\ \frac{\partial u_s}{\partial \xi^+} & \frac{\partial u_s}{\partial a_s} & \frac{\partial u_s}{\partial \xi^-} & \frac{\partial u_s}{\partial \mathrm{M}} \\ \frac{\partial m_0}{\partial \xi^+} & \frac{\partial m_0}{\partial a_s} & \frac{\partial m_0}{\partial \xi^-} & \frac{\partial m_0}{\partial \mathrm{M}} \end{pmatrix}. \tag{4.47}$$

Unlike the previous method, the variances of each point in the phase space can be determined directly from the measured variables. No iterative procedure is needed.

4.5 Results

Run 7 was chosen to be the central run around which the other runs were expanded. This leads to 6 equations with 4 parameters for each of the fitted values. This allowed the use of constrained fits with two degrees of freedom.

Note on β vs. u_s:

As can be seen from the actions in Eqs. 4.12 and 4.11 and also from Table 4.4 there are five input parameters for each run. However two of these variables, u_s and β are dependent on each other. Therefore it is appropriate to take one of them to be a fixed parameter and consider the other one to vary. It was decided to take u_s to be the

varying parameter and to treat β as a constant. For the sake of comparison, the fits were also attempted by using β as a varying parameter in order to see if this affected the fitted values for the other coefficients. In practice, the values for β were tuned during the initial gauge generation process in order to obtain a particular value of u_s.

The coefficients for the partial derivatives of the input β values with respect to the output values, $\frac{\partial\beta}{\partial\xi^+}$, are also determined for the sake of comparison.

4.5.1 Results for method 1

As discussed in the previous section, this method involves starting by guessing the initial variances assigned to each point. A fit is performed to each bootstrap. Two different approaches were used for the initial guess in the fitting procedure. The first approach consists of performing an unconstrained fit using the "best-fit" values. These values are the measurements obtained from the original unbootstrapped configurations. This initial guess is then used as the starting point for each of the individual bootstraps for the first iteration. For each subsequent iteration, the guess starts with the fitted values obtained from the previous iteration. In the second approach, the same initial guess from the best-fit is used for each iteration. After each iteration of the procedure the fitted parameters are inserted back into the original equation along with the input values and the variances are determined by using the jackknife method over the 1000 bootstrapped data sets. For example, considering Eq. 4.35, the measured parameters are $\{\Delta\xi^+, \Delta a_s, \Delta\xi^-, \Delta\mathrm{M}\}$. After each iteration the values, $\{\frac{\partial\xi_q^0}{\partial\xi^+}, \frac{\partial\xi_q^0}{\partial a_s}, \frac{\partial\xi_q^0}{\partial\xi^-}, \frac{\partial\xi_q^0}{\partial\mathrm{M}}\}$ are determined. Then the "modelled" value ξ^m is determined from

$$\Delta\xi^m = \frac{\partial\xi_q^0}{\partial\xi^+}\Delta\xi^+ + \frac{\partial\xi_q^0}{\partial a_s}\Delta a_s + \frac{\partial\xi_q^0}{\partial\xi^-}\Delta\xi^- + \frac{\partial\xi_q^0}{\partial\mathrm{M}}\Delta\mathrm{M} \tag{4.48}$$

and the variance of ξ_q^0 is taken to be the variance of ξ^m. However this procedure is somewhat circular and does not lead to a good independent estimate of the variance. If the first iteration leads to a very close fit to the measured values for ξ_q^0, this in

turns leads to a very small estimate of the variance for the next iteration. This in turn affects the χ^2 goodness of fit measure for that iteration and will also limit the inverse-Hessian part of the Marquardt-Levenberg algorithm. There is a danger that the algorithm can get stuck in a local minimum and will not move far from its previous position. Various tolerance levels for convergence were also examined. The tolerance level is defined as the maximum change in corresponding fitted values for the same bootstrapped sample between consecutive iterations. It was found that the results did not deviate substantially when changing the tolerance level from 0.001 through to 0.0000001.

The resulting fits from this procedure were not stable. The iterative procedure immediately led to very small estimates for the variances which then approached zero with subsequent iterations. As a consequence of this, the initial random covariance matrix had a large influence in which direction the minimising algorithm progressed. Thus the final fits for an individual bootstrap data set changed with different initial variances. The average values over the entire bootstrapped set was relatively stable in that the majority of fitting attempts gave similar answers but the final χ^2 values were far too large for the fit to be trusted in any case. It should also be noted that the second approach mentioned above, whereby the same initial guess is used for each iteration, failed to produce any meaningful results except for the case of very large tolerances ~ 0.01. The reason for this is that as the iterations progress the variances reduce as described above. With a very small covariance matrix, the fitting procedure will fail to move from the initial guess. Table 4.6 illustrates the fitting procedure for Eq. 4.37. This table shows how the fitted values change between the first and final iteration of the iterative procedure and also between different random initial variances. The values for both the average value over each bootstrap and the value for one specific individual bootstrap sample (labelled bootstrap 1) are presented. It can be seen that the fitted parameters do not change significantly between the first and final iteration. This is due to the jackknife estimates of the variance quickly becoming very small and inhibiting the fitting procedure. Considering the two different initial covariance matrices, it can also be seen that although the average values do not vary

	Initial covariance matrix 1				Initial covariance matrix 2	
	1st iteration		Final value		Final value	
	Average	# 1	Average	# 1	Average	# 1
$\frac{\partial u_s}{\partial \xi^+}$	$-0.0338^{+0.0058}_{-0.0055}$	-0.0271	$-0.0382^{+0.0066}_{-0.0065}$	-0.0300	$-0.0170^{+0.0084}_{-0.0084}$	-0.0150
$\frac{\partial u_s}{\partial a_s}$	$-0.2764^{+0.1093}_{-0.1050}$	-0.3695	$-0.2621^{+0.1433}_{-0.1285}$	-0.3736	$-0.2726^{+0.0590}_{-0.0537}$	-0.2453
$\frac{\partial u_s}{\partial \xi^-}$	$-0.0368^{+0.0059}_{-0.0057}$	-0.0309	$-0.0378^{+0.0064}_{-0.0060}$	-0.0314	$-0.0270^{+0.0077}_{-0.0077}$	-0.0253
$\frac{\partial u_s}{\partial M}$	$0.0079^{+0.0218}_{-0.0216}$	0.0313	$0.0089^{+0.0281}_{-0.0275}$	0.0379	$0.0086^{+0.0083}_{-0.0083}$	-0.0083

Table 4.6: This table illustrates the effects of starting with different initial covariance matrices in the iterative procedure. In this case the relevant equation is Eq.4.37. The first column shows the coefficient in question. The second shows the result of the fitting procedure after the first iteration. The figure quoted is the average value. The error bars are obtained from a 68% confidence interval over 1000 bootstraps. The third column shows the result for fitting a specific individual bootstrap sample. The fourth column and fifth columns show the equivalent results after the iterative procedure is completed. The sixth and seventh columns show the same results after the iterative procedure is completed after starting with a different initial random covariance matrix. However the respective $\chi^2/N_{\text{d.f}}$ are 0.0002, $\sim$ 7000 and $\sim$ 10000 respectively. These $\chi^2/N_{\text{d.f}}$ values call the quality of all the fits into question. These values can also be compared with those given in Table 4.7. In particular note that the individual bootstrap values for $\frac{\partial u_s}{\partial M}$ changed signs between repeats of the procedure.

greatly between the two runs, the results for the individual bootstraps can change significantly. However, on examining the $\chi^2/N_{\text{d.f}}$ for all of these fits it can be seen that they are either too large or too small for the fitted values to have any significance.

4.5.2 Results for method 2

The fitting procedure for this method is more straightforward than the previous method. Each of the Eqs. 4.40-4.43 are fitted in order to obtain the parameters of the matrix in Eq. 4.45. This matrix is then inverted and the Karsch Coefficients are determined from the inverse of this matrix as shown in Eq. 4.47. In order to obtain a measure of the legitimacy of this inversion procedure fit and the choice of u_s over β, it was repeated with u_s replaced by β. The results for fitting Eqs. 4.40 - 4.43 are given below in equation Eq. 4.49

$$
\begin{aligned}
B &= \begin{pmatrix}
\frac{\partial \xi^+}{\partial \xi_q^0} & \frac{\partial \xi^+}{\partial \xi_g^0} & \frac{\partial \xi^+}{\partial u_s} & \frac{\partial \xi^+}{\partial m_0} \\
\frac{\partial a_s}{\partial \xi_q^0} & \frac{\partial a_s}{\partial \xi_g^0} & \frac{\partial a_s}{\partial u_s} & \frac{\partial a_s}{\partial m_0} \\
\frac{\partial \xi^-}{\partial \xi_q^0} & \frac{\partial \xi^-}{\partial \xi_g^0} & \frac{\partial \xi^-}{\partial u_s} & \frac{\partial \xi^-}{\partial m_0} \\
\frac{\partial \mathrm{M}}{\partial \xi_q^0} & \frac{\partial \mathrm{M}}{\partial \xi_g^0} & \frac{\partial \mathrm{M}}{\partial u_s} & \frac{\partial \mathrm{M}}{\partial m_0}
\end{pmatrix} \\
&= \begin{pmatrix}
0.230^{+0.020}_{-0.020} & -0.095^{+0.029}_{-0.027} & -23.6^{+4.1}_{-3.3} & 43.0^{+4.7}_{-4.8} \\
-0.0097^{+0.0014}_{-0.0015} & -0.0388^{+0.0025}_{-0.0028} & -3.27^{+0.27}_{-0.32} & 1.79^{+0.56}_{-0.47} \\
-0.137^{+0.017}_{-0.020} & 0.376^{+0.025}_{-0.030} & 20.4^{+3.0}_{-4.1} & -43.1^{+4.9}_{-4.7} \\
-0.0852^{+0.0075}_{-0.0071} & -0.218^{+0.015}_{-0.013} & -18.7^{+1.8}_{-1.8} & 34.4^{+2.3}_{-2.2}
\end{pmatrix}.
\end{aligned} \tag{4.49}
$$

The $\chi^2/N_{\mathrm{d.f}}$ for the "best fits" in the rows in Eq. 4.49 are 9.8, 4.8, 8.3 and 3.0 respectively. The resulting matrix inversion leads to the values quoted in Tab. 4.7. The fitting procedure was repeated with u_s replaced by β in the above equations. The resulting fits lead to the matrix

$$
\begin{aligned}
B &= \begin{pmatrix}
\frac{\partial \xi^+}{\partial \xi_q^0} & \frac{\partial \xi^+}{\partial \xi_g^0} & \frac{\partial \xi^+}{\partial \beta} & \frac{\partial \xi^+}{\partial m_0} \\
\frac{\partial a_s}{\partial \xi_q^0} & \frac{\partial a_s}{\partial \xi_g^0} & \frac{\partial a_s}{\partial \beta} & \frac{\partial a_s}{\partial m_0} \\
\frac{\partial \xi^-}{\partial \xi_q^0} & \frac{\partial \xi^-}{\partial \xi_g^0} & \frac{\partial \xi^-}{\partial \beta} & \frac{\partial \xi^-}{\partial m_0} \\
\frac{\partial \mathrm{M}}{\partial \xi_q^0} & \frac{\partial \mathrm{M}}{\partial \xi_g^0} & \frac{\partial \mathrm{M}}{\partial \beta} & \frac{\partial \mathrm{M}}{\partial m_0}
\end{pmatrix} \\
&= \begin{pmatrix}
0.231^{+0.020}_{-0.020} & -0.195^{+0.038}_{-0.034} & -4.98^{+0.84}_{-0.65} & 48.3^{+4.8}_{-5.1} \\
-0.010^{+0.001}_{-0.001} & -0.054^{+0.003}_{-0.004} & -0.690^{+0.057}_{-0.067} & 2.70^{+0.61}_{-0.52} \\
-0.140^{+0.018}_{-0.020} & 0.458^{+0.031}_{-0.038} & 4.23^{+0.62}_{-0.82} & -47.4^{+5.0}_{-4.9} \\
-0.085^{+0.008}_{-0.007} & -0.304^{+0.021}_{-0.020} & -3.96^{+0.39}_{-0.39} & 39.8^{+2.7}_{-2.6}
\end{pmatrix}
\end{aligned} \tag{4.50}
$$

The $\chi^2/N_{\mathrm{d.f}}$ for the "best fits" fits in the rows in Eq. 4.50 are 6.5, 3.2, 6.7 and 6.6 respectively. Again the inversion of this matrix gives the required Karsch coefficients.

The results for the Karsch coefficients from all three different fitting procedures are given together in Table 4.7.

	Method 1	Method 2	
		u_s	β
$\frac{\partial \xi_q^0}{\partial \xi^+}$	$1.58^{+0.51}_{-0.53}$	$1.55^{+0.47}_{-0.39}$	$1.51^{+0.48}_{-0.39}$
$\frac{\partial \xi_q^0}{\partial a_s}$	$-14.64^{+8.55}_{-8.16}$	$2.51^{+5.72}_{-4.74}$	$1.79^{+5.88}_{-4.63}$
$\frac{\partial \xi_q^0}{\partial \xi^-}$	$-2.53^{+0.51}_{-0.52}$	$-2.01^{+0.54}_{-0.44}$	$-2.10^{+0.53}_{-0.44}$
$\frac{\partial \xi_q^0}{\partial \mathrm{M}}$	$-2.71^{+1.69}_{-1.70}$	$-4.60^{+0.59}_{-0.68}$	$-4.44^{+0.59}_{-0.69}$
$\frac{\partial \xi_g^0}{\partial \xi^+}$	$3.00^{+0.53}_{-0.51}$	$2.64^{+0.52}_{-0.41}$	$2.64^{+0.52}_{-0.42}$
$\frac{\partial \xi_g^0}{\partial a_s}$	$-4.29^{+4.19}_{-4.38}$	$-5.24^{+4.35}_{-4.65}$	$-5.39^{+4.26}_{-4.65}$
$\frac{\partial \xi_g^0}{\partial \xi^-}$	$4.07^{+0.55}_{-0.59}$	$3.76^{+0.52}_{-0.48}$	$3.76^{+0.51}_{-0.48}$
$\frac{\partial \xi_g^0}{\partial \mathrm{M}}$	$2.11^{+1.06}_{-1.06}$	$1.68^{+0.62}_{-0.60}$	$1.63^{+0.63}_{-0.60}$
$\frac{\partial u_s}{\partial \xi^+}$	$-0.03154^{+0.0061}_{-0.0060}$	$-0.0352^{+0.0055}_{-0.0070}$	
$\frac{\partial u_s}{\partial a_s}$	$-0.310^{+0.059}_{-0.054}$	$-0.380^{+0.063}_{-0.074}$	
$\frac{\partial u_s}{\partial \xi^-}$	$-0.0324^{+0.0076}_{-0.0071}$	$-0.0404^{+0.0056}_{-0.0073}$	
$\frac{\partial u_s}{\partial \mathrm{M}}$	$0.029^{+0.012}_{-0.011}$	$0.013^{+0.011}_{-0.009}$	
$\frac{\partial \beta}{\partial \xi^+}$	$-0.177^{+0.051}_{-0.054}$		$-0.224^{+0.035}_{-0.044}$
$\frac{\partial \beta}{\partial a_s}$	$-1.95^{+0.38}_{-0.38}$		$-1.97^{+0.38}_{-0.44}$
$\frac{\partial \beta}{\partial \xi^-}$	$-0.264^{+0.041}_{-0.041}$		$-0.275^{+0.036}_{-0.047}$
$\frac{\partial \beta}{\partial \mathrm{M}}$	$0.0770^{+0.070}_{-0.072}$		$0.077^{+0.063}_{-0.053}$
$\frac{\partial m_0}{\partial \xi^+}$	$0.0075^{+0.0071}_{-0.0068}$	$0.0014^{+0.0026}_{-0.0026}$	$0.0011^{+0.0026}_{-0.0025}$
$\frac{\partial m_0}{\partial a_s}$	$-0.141^{+0.067}_{-0.073}$	$-0.233^{+0.034}_{-0.039}$	$-0.233^{+0.034}_{-0.040}$
$\frac{\partial m_0}{\partial \xi^-}$	$0.0022^{+0.0079}_{-0.0073}$	$-0.0031^{+0.0028}_{-0.0030}$	$-0.0031^{+0.0029}_{-0.0030}$
$\frac{\partial m_0}{\partial \mathrm{M}}$	$0.0405^{+0.0059}_{-0.0059}$	$0.0355^{+0.0058}_{-0.0043}$	$0.0358^{+0.0058}_{-0.0044}$

Table 4.7: This table shows the result of the attempts to fit the Karsch Coefficients. The numbers quoted in the first column are the average results obtained over 1000 bootstraps using the iterative procedure described above. The second and third columns show the results obtained by inverting the parameter matrix. The second column considers $\{\xi_q^0, \xi_g^0, u_s, m_0\}$ as input variables compared to $\{\xi_q^0, \xi_g^0, \beta, m_0\}$ for the third column. All quoted errors are obtained using a 68% confidence interval

Run	$\Delta\xi_q^0$	$\Delta\xi_q^0$	Δm_0	Δu_s	$\Delta\beta$
$\Delta 4$	1.29	-1.77	0.000	0.00	0.036
$\Delta 8$	0.00	0.00	0.007	0.00	0.006
$\Delta 9$	0.00	0.00	0.000	-0.01	-0.050
$\Delta 1$	-1.43	-0.42	0.000	0.00	0.005
$\Delta 5$	1.40	-0.98	0.000	0.00	0.014
$\Delta 6$	0.09	-0.36	0.000	0.00	0.006

Table 4.8: This table shows the input values used for each of the Karsch fits. Run 7 is taken to be the central run around which the other runs are expanded. $(\Delta\xi_q^0)_{\Delta 4} = (\xi_q^0)_{\text{Run 4}} - (\xi_q^0)_{\text{Run 7}}$ etc. The first four rows of the table are used in order to find an initial guess via an unconstrained fit.

4.5.3 Discussion of Results

Some of the input parameters from Table 4.4 did not vary across each runs. This leads to a lot of the "Δ" values being zero as can be seen in Table 4.8. For the iterative procedure, i.e. Eqs. 4.35 - 4.38, this issue is not as significant as it is for Eqs. 4.40 - 4.43. For the inverse matrix method only one of the runs will contribute to the measured value of the derivatives with respect to u_s and m_0. Ideally each input parameter should be different on each run. The runs labelled 1-7 were generated for the purpose of the Tuning Study in Chapter 3. The computational overhead involved in re-generating these with different input parameters was beyond the scope of this study. The final two simulations, labelled Run 8 & Run 9 were then generated with different values of m_0 and u_s respectively.

The fitted values are presented together in Table 4.7. The results from the second column are measurements from using the iterative method. As mentioned previously, although the average value over all bootstraps tended to remain relatively stable, the measurements from individual bootstraps did vary considerably. This also led to discrepancies in the errors between runs. The figures in this table are quoted with the understanding that they were chosen as fits in which the errors using a 68% confidence interval were reasonable. A proportion of the fitting runs led to the measured value being zero within errors. As such, these figures are presented merely for the sake of comparison. It should be pointed out that many of the quoted numbers are similar or do agree within errors with those from the matrix inversion method, the individual

fitting runs were not selected for this reason.

The third and fourth columns present the results from the matrix inversion method with u_s and β respectively being chosen as one of the input variables. The $\chi^2/N_{\text{d.f}}$ values for the initial fits before the matrix inversion were in the region $\sim 3-10$ which would be considered as moderate fits. The coefficients $\frac{\partial \xi_q^0}{\partial a_s}$ and $\frac{\partial m_0}{\partial \xi^+}$ were zero within errors. $\frac{\partial m_0}{\partial \xi^-}$ was almost zero within the quoted confidence interval. It can be seen that there is a surprisingly good correspondence between all three columns. The only coefficients which are not consistent are $\frac{\partial \xi_q^0}{\partial a_s}$ and $\frac{\partial m_0}{\partial \xi^-}$ and it can be seen that the former is zero for the matrix inversion and the latter is zero for the iterative method.

One particularly interesting result from Table 4.4 is the value for $\frac{\partial \xi_g^0}{\partial a_s}$. One would assume that increasing the input value ξ_g^0 would lead to a corresponding increase in the renormalised lattice spacing a_s. However the values from all three methods were negative. This could be interpreted as evidence that the system deviates from the assumption of linearity over the region of phase space that the simulations were performed. It should also be noted that the spatial lattice spacing is relatively coarse, being in the region $0.15 \sim 0.2$ fm and this may also contribute to an unquantified systematic error.

4.6 Future work

There are a number of obvious suggestions which would be used if the study was to be repeated. For the iterative method, the fits could be attempted using a different minimisation method than the Marquardt-Levenberg. It can be postulated that the reason that this method does not give consistent results is due to the use of the initial random covariance matrix. The use of algorithms such as basic steepest descent or conjugate gradient would not entail the use of the covariance matrix. For the case of the inverse matrix method, it would be highly beneficial for the determination of the original fitted parameters if each input parameter varied for each separate run. It can be seen from Table 4.8 that only one of the input equations actually contributes to the determination of the derivative of the output parameter with respect to m_0 and u_s.

Chapter 5

Concluding remarks

This thesis concerns itself with the non-perturbative study of action parameters in anisotropic QCD. It has shown that the action parameters can be precisely determined for dynamical anisotropic simulations using a two-dimensional plane fit. The tuning procedure leads to the recovery of Lorentz invariance and the tuned dataset can subsequently be used for a variety of physics including spectroscopy and decays.

The second part of the thesis considers the application of the techniques developed for determination of the action parameters to the field of finite temperature QCD. The equations of state of a finite temperature QCD system are paramount to the understanding of that system. One method of determining these equations of state requires the knowledge of Karsch's anisotropy coefficients. These coefficients have proven notoriously difficult to calculate, both perturbatively and non-perturbatively. This study shows that the same datasets used in the tuning procedure mentioned above can also provide a basis for a non-perturbative determination of these coefficients. It is shown how the application of two different approaches can result in a significant increase in stability of the measurements and an associated reduction in statistical errors.

Appendix A

Appendix

A.1 Hardware specifications

The main computing facilities available from "TCHPC" were the clusters detailed in Table A.1.

A.1.1 Tables of momenta used

The tables of momenta which were averaged over for the purposes of generating dispersion relations are given in Tables A.1.1 and A.1.1.

Name	Nodes	RAM	Arch	Interconnect	Theoretical Peak Performance
iitac.tchpc.tcd.ie	356 Dual AMD Opteron	1.4TB	64bit	Voltaire Infiniband	3.4TFlops
moloch.tchpc.tcd.ie	65 Dual Intel Xeon	130GB	32bit	Gigabit Ethernet	0.8TFlops
aegir.maths.tcd.ie	32 2Dual Intel Xeon	32GB	32bit	Gigabit Ethernet	0.064TFlops

Moloch Node	Specifications
Processors	2
Vendor	Intel
Model	Xeon
CPU Speed	3.06 Ghz
Cache size	L1 16Kb instruction, L1 16Kb data, L2 512Kb
RAM	2GB 400Mhz DDR
Disk	SCSI 73407 MB
Ethernet	2 Broadcom BCM5703 Gigabit Ethernet

IITAC Node	Specifications
Processors	2
Vendor	AMD
Model	Opteron 250
CPU	Speed 2.4 Ghz
Cache	size L1 64Kb instruction, L1 64Kb data, L2 1024Kb
RAM	4GB DDR PC3200
Disk	80GB SATA
Ethernet	2 Broadcom BCM5704 Gigabit Ethernet

Table A.1: Main computing clusters available from TCHPC

(0,0,0)
(0,0,1),(0,1,0),(1,0,0)
(0,1,1),(1,0,1),(1,1,0)
(1,1,1)
(0,0,2),(0,2,0),(2,0,0)
(0,1,2),(1,0,2),(1,2,0),(0,2,1),(2,1,0),(2,0,1)
(1,1,2),(1,2,1),(2,1,1)
(2,2,1),(2,1,2),(1,2,2)
(2,2,2)

Table A.2: This table shows the equivalent momenta used to generate point propagators. Note that not all possible momenta in the range $[0 - 12]$ were used.$(0, 2, 2), (0, 0, 3), (0, 3, 1), (1, 3, 1)$ and equivalent momenta were omitted

(0,0,0)
(0,0,1),(0,1,0),(1,0,0)
(0,1,1),(0,1,-1),(1,0,1),(1,0,-1),(1,1,0),(1,-1,0)
(1,1,1),(1,1,-1),(1,-1,1),(-1,1,1)
(0,0,2),(0,2,0),(2,0,0)
(0,1,2),(0,1,-2),(0,2,1),(0,2,-1),(1,0,2),(1,0,-2),(1,2,0),(1,-2,0),(2,0,1),(2,0,-1),(2,1,0),(2,-1,0)

Table A.3: Momenta used for all-to-all propagators

Appendix B

Determination of a_S

A preliminary determination of the lattice spacings were made by fitting the interquark potential to the Cornell potential and using the fitted parameters to set the scale. The final determination was made by using the Sommer parameter. The potential plots and Cornell fit parameters which were not included in the main body of the thesis are included here for completeness.

Range	A	B	C	χ^2/dof
[1:7]	0.20089 (0.00000)	-0.37904 (0.00005)	0.84123 (0.00005)	2.17e+03
[2:7]	0.19528 (0.00010)	-0.43269 (0.00071)	0.87927 (0.00116)	1.98e+03
[3:7]	0.15870 (0.00117)	-1.05791 (0.00773)	1.19044 (0.00873)	8.85e+00
[4:7]	0.15976 (0.00305)	-1.03158 (0.03895)	1.17972 (0.01798)	4.36e+00
[5:7]	0.15274 (0.00843)	-1.26887 (0.24462)	1.26215 (0.08859)	2.84e-14
[1:6]	0.20194 (0.00022)	-0.37692 (0.00042)	0.83806 (0.00066)	1.50e+03
[2:6]	0.19950 (0.00040)	-0.39968 (0.00003)	0.85433 (0.00042)	1.48e+03
[3:6]	0.15894 (0.00021)	-1.05442 (0.01360)	1.18855 (0.00552)	8.85e+00
[4:6]	0.16272 (0.00541)	-0.96940 (0.09121)	1.15235 (0.04575)	8.42e-10
[1:5]	0.20329 (0.00005)	-0.37422 (0.00006)	0.83402 (0.00011)	1.06e+03
[2:5]	0.20626 (0.00079)	-0.34793 (0.00523)	0.81493 (0.00423)	1.02e+03
[3:5]	0.15749 (0.00097)	-1.07394 (0.02474)	1.19939 (0.01192)	5.28e-14
[1:4]	0.20580 (0.00013)	-0.36919 (0.00027)	0.82648 (0.00039)	7.97e+02
[2:4]	0.23355 (0.00050)	-0.16128 (0.00296)	0.66700 (0.00093)	8.29e-17
[1:3]	0.19545 (0.00024)	-0.38985 (0.00046)	0.85748 (0.00069)	1.23e-15

Table B.1: Fit parameters for the fit to the Cornell potential for RUN 4. The first column shows the relevant fit range. The central columns show the fit parameters from a fit to $Ax + B/x + C$. The figures in brackets are statistical errors obtained using a 68% confidence interval over the set of 1000 bootstraps. The final column shows the χ^2 per degree of freedom for the best fit. The relevent plots are those in Fig. B-1.

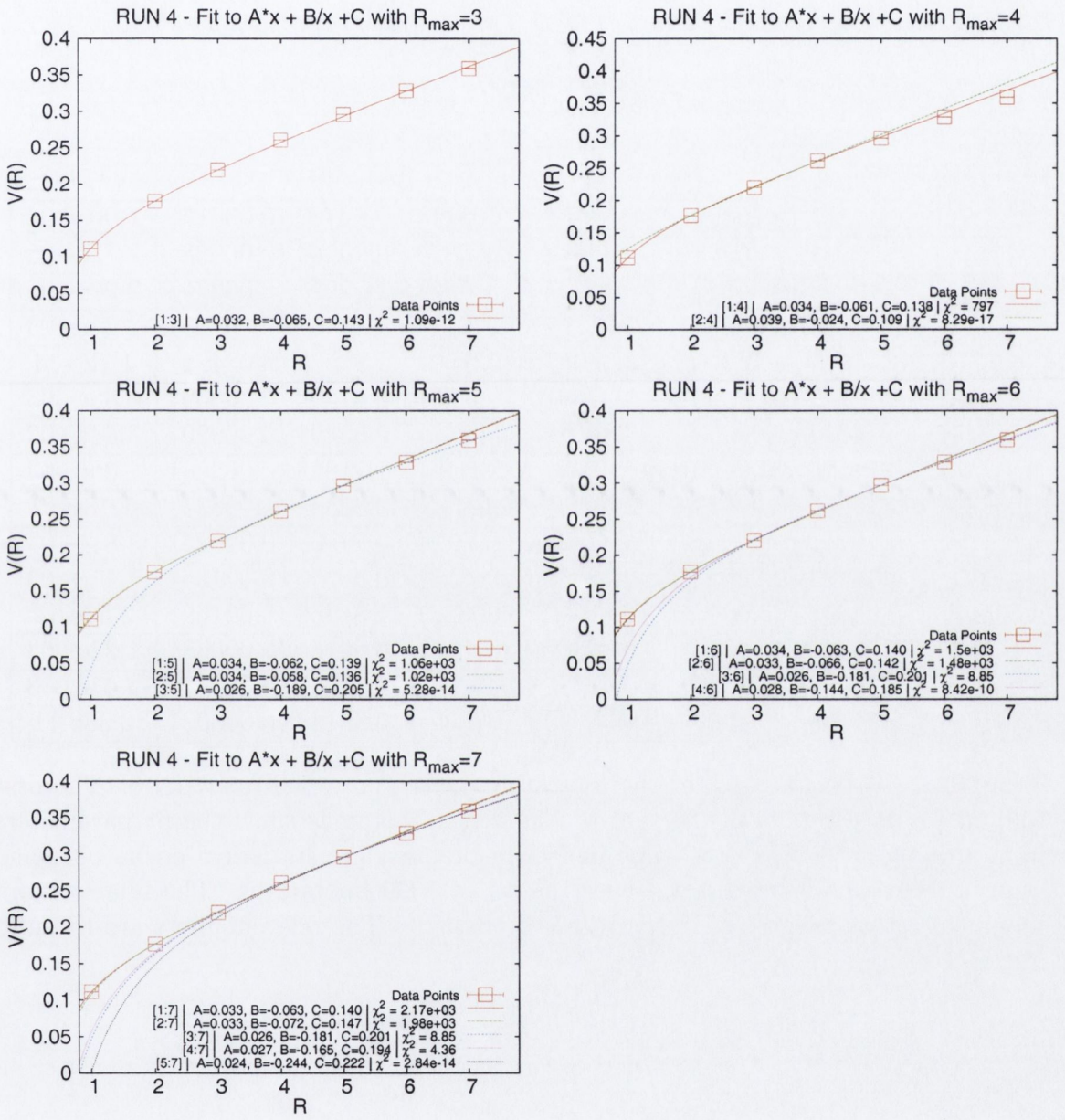

Figure B-1: Fits to the Cornell Potential for Run 4 for all values of $R_{\max}$ and $R_{\min}$. The resulting measured fit parameters can be found in Tab. B.1.

Range	A	B	C	χ^2/dof
[1:7]	0.14871 (0.00006)	-0.38104 (0.00011)	0.82777 (0.00017)	1.00e+04
[2:7]	0.13811 (0.00008)	-0.48678 (0.00027)	0.90184 (0.00028)	7.72e+03
[3:7]	0.10099 (0.00030)	-1.16625 (0.00482)	1.22978 (0.00270)	2.29e+03
[4:7]	0.10696 (0.00056)	-1.01398 (0.01062)	1.16867 (0.00745)	2.24e+03
[5:7]	-0.04177 (0.00132)	-6.09987 (0.02799)	2.92683 (0.02491)	1.72e-14
[1:6]	0.15129 (0.00003)	-0.37587 (0.00006)	0.82002 (0.00009)	3.88e+03
[2:6]	0.14613 (0.00007)	-0.42519 (0.00030)	0.85499 (0.00090)	3.44e+03
[3:6]	0.11535 (0.00110)	-0.95081 (0.00419)	1.11628 (0.00364)	1.36e+03
[4:6]	0.17650 (0.00043)	0.44838 (0.00159)	0.52581 (0.00635)	1.13e-10
[1:5]	0.15160 (0.00009)	-0.37525 (0.00017)	0.81908 (0.00026)	3.81e+03
[2:5]	0.14473 (0.00021)	-0.43665 (0.00283)	0.86353 (0.00134)	3.41e+03
[3:5]	0.08842 (0.00003)	-1.31332 (0.00328)	1.31858 (0.00169)	2.57e-14
[1:4]	0.15741 (0.00013)	-0.36362 (0.00025)	0.80165 (0.00038)	1.25e+03
[2:4]	0.13943 (0.00006)	-0.49402 (0.00053)	0.90282 (0.00072)	3.43e+03
[1:3]	0.14748 (0.00000)	-0.38348 (0.00000)	0.83143 (0.00000)	2.38e-11

Table B.2: Fit parameters for the fit to the Cornell potential for RUN 5. The first column shows the relevant fit range. The central columns show the fit parameters from a fit to $Ax + B/x + C$. The figures in brackets are statistical errors obtained using a 68% confidence interval over the set of 1000 bootstraps. The final column shows the χ^2 per degree of freedom for the best fit. The relevent plots are those in Fig. B-2.

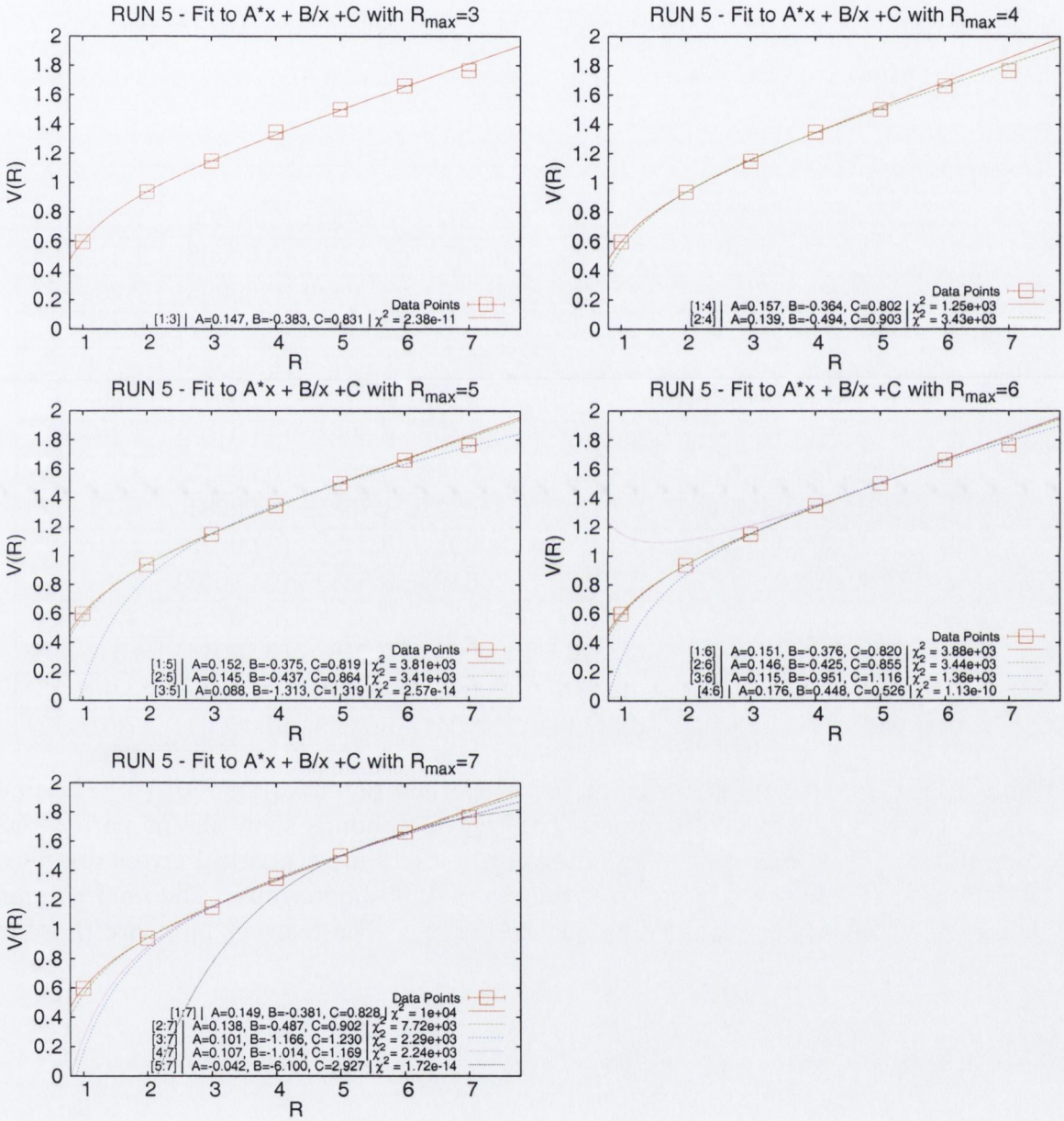

Figure B-2: Fits to the Cornell Potential for Run 5 for all values of $R_{\max}$ and $R_{\min}$. The resulting measured fit parameters can be found in Tab. B.2.

Range	A	B	C	χ^2/dof
[1:7]	0.14902 (0.00003)	-0.33200 (0.00002)	0.74841 (0.00006)	1.23e+04
[2:7]	0.14678 (0.00015)	-0.35563 (0.00071)	0.76468 (0.00038)	1.21e+04
[3:7]	0.12250 (0.00007)	-0.80187 (0.00043)	0.98114 (0.00093)	7.26e+03
[4:7]	0.05099 (0.00063)	-2.61871 (0.01575)	1.71324 (0.00297)	6.46e+00
[5:7]	0.06079 (0.00013)	-2.28213 (0.05737)	1.59724 (0.00553)	4.19e-09
[1:6]	0.15182 (0.00006)	-0.32644 (0.00005)	0.74006 (0.00014)	4.86e+03
[2:6]	0.15758 (0.00001)	-0.26902 (0.00147)	0.69989 (0.00103)	4.26e+03
[3:6]	0.14469 (0.00070)	-0.48461 (0.00940)	0.80878 (0.00315)	3.59e+03
[4:6]	0.04612 (0.00041)	-2.72201 (0.01432)	1.75853 (0.00281)	4.72e-11
[1:5]	0.15430 (0.00006)	-0.32139 (0.00007)	0.73252 (0.00013)	2.91e+03
[2:5]	0.16865 (0.00027)	-0.19009 (0.00019)	0.63827 (0.00058)	3.87e+02
[3:5]	0.18466 (0.00084)	0.04877 (0.00960)	0.51168 (0.00770)	4.69e-14
[1:4]	0.14894 (0.00006)	-0.33227 (0.00008)	0.74875 (0.00014)	4.11e+02
[2:4]	0.15981 (0.00034)	-0.24949 (0.00301)	0.68567 (0.00179)	3.40e-13
[1:3]	0.14453 (0.00000)	-0.34114 (0.00004)	0.76204 (0.00004)	7.61e-12

Table B.3: Fit parameters for the fit to the Cornell potential for RUN 6. The first column shows the relevant fit range. The central columns show the fit parameters from a fit to $Ax + B/x + C$. The figures in brackets are statistical errors obtained using a 68% confidence interval over the set of 1000 bootstraps. The final column shows the χ^2 per degree of freedom for the best fit. The relevent plots are those in Fig. B-3.

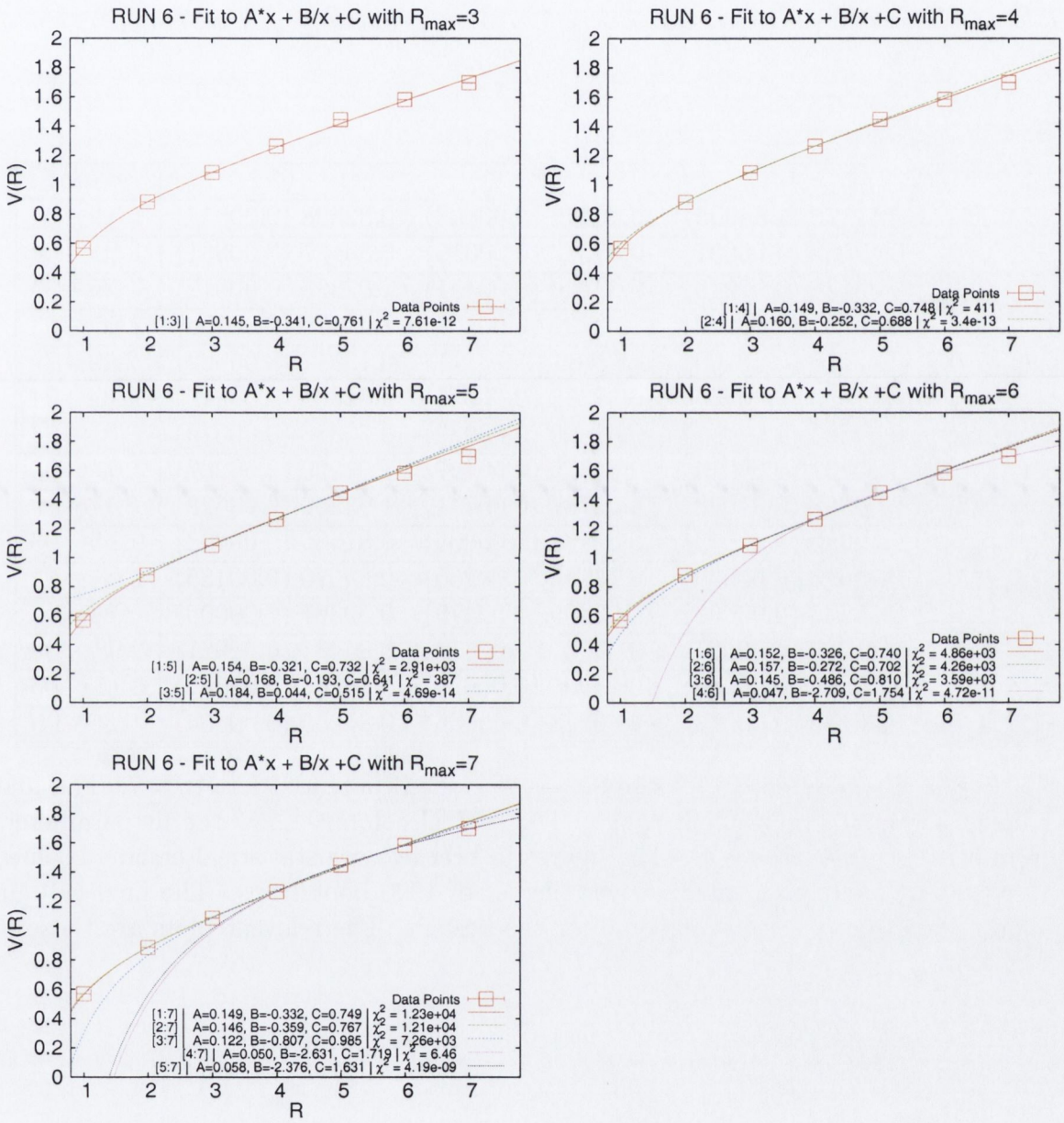

Figure B-3: Fits to the Cornell Potential for Run 6 for all values of $R_{\max}$ and $R_{\min}$. The resulting measured fit parameters can be found in Tab. B.3.

Range	A	B	C	χ^2/dof
[1:7]	0.11776 (0.00005)	-0.40016 (0.00009)	0.82498 (0.00014)	1.53e+04
[2:7]	0.12063 (0.00001)	-0.37023 (0.00019)	0.80427 (0.00031)	1.50e+04
[3:7]	0.09626 (0.00040)	-0.83240 (0.00451)	1.02303 (0.00012)	7.05e+03
[4:7]	0.05929 (0.00039)	-1.83725 (0.00107)	1.41375 (0.00156)	2.86e+03
[5:7]	0.16728 (0.00100)	1.87466 (0.01589)	0.13518 (0.00992)	2.29e-15
[1:6]	0.11839 (0.00005)	-0.39890 (0.00011)	0.82308 (0.00016)	1.36e+04
[2:6]	0.12683 (0.00005)	-0.31425 (0.00039)	0.76388 (0.00076)	1.16e+04
[3:6]	0.09751 (0.00018)	-0.81355 (0.00497)	1.01299 (0.00207)	7.03e+03
[4:6]	0.00388 (0.00038)	-3.02737 (0.00741)	1.93260 (0.00628)	6.17e-11
[1:5]	0.12080 (0.00003)	-0.39408 (0.00005)	0.81586 (0.00008)	9.24e+03
[2:5]	0.14473 (0.00030)	-0.17150 (0.00256)	0.65670 (0.00185)	1.08e+02
[3:5]	0.15265 (0.00061)	-0.05185 (0.00475)	0.59361 (0.00005)	2.89e-13
[1:4]	0.11263 (0.00007)	-0.41041 (0.00014)	0.84035 (0.00021)	2.98e+03
[2:4]	0.11096 (0.00005)	-0.41908 (0.00025)	0.84804 (0.00009)	3.15e+03
[1:3]	0.10190 (0.00018)	-0.43188 (0.00036)	0.87255 (0.00054)	6.86e-11

Table B.4: Fit parameters for the fit to the Cornell potential for RUN 7. The first column shows the relevant fit range. The central columns show the fit parameters from a fit to $Ax + B/x + C$. The figures in brackets are statistical errors obtained using a 68% confidence interval over the set of 1000 bootstraps. The final column shows the χ^2 per degree of freedom for the best fit. The relevent plots are those in Fig. B-4.

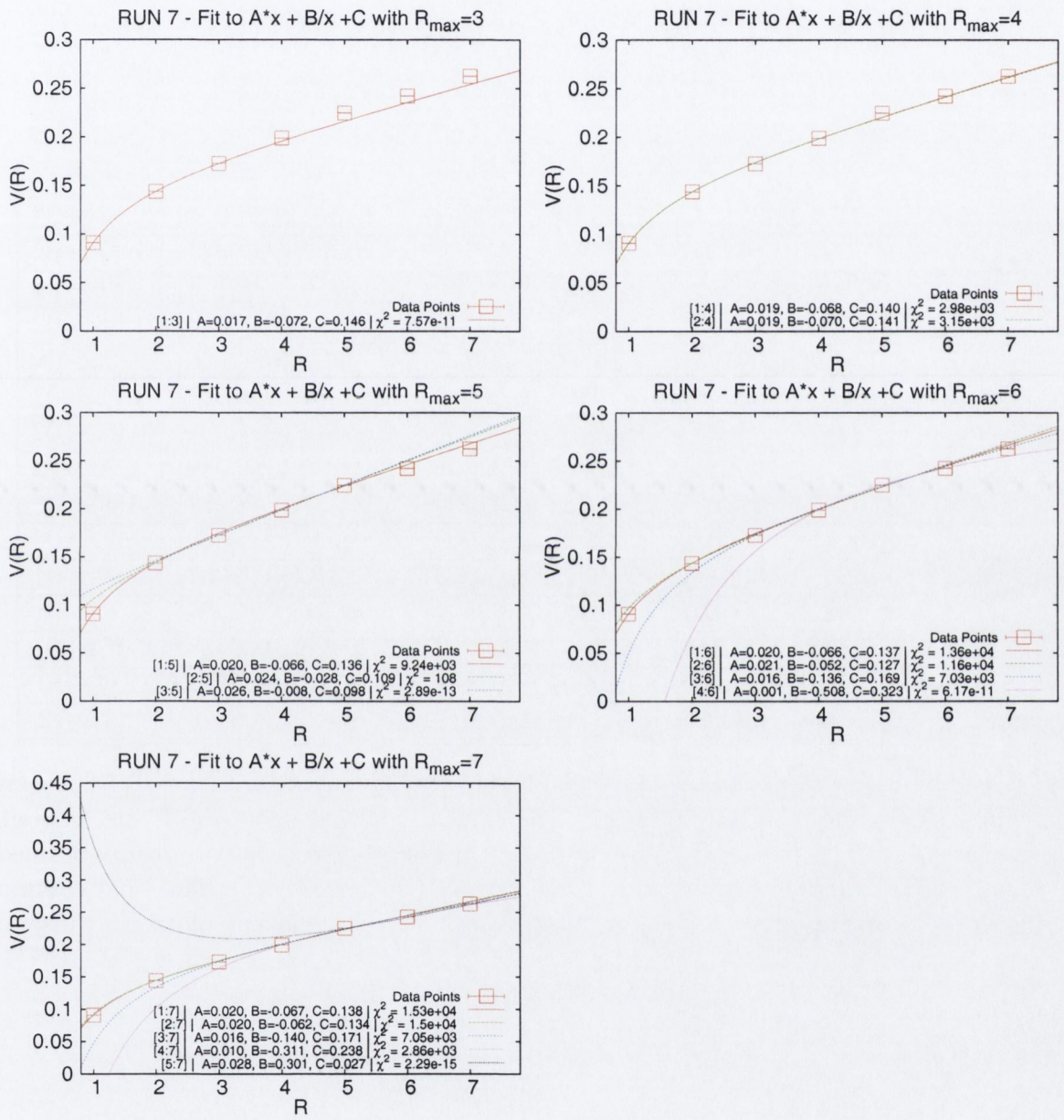

Figure B-4: Fits to the Cornell Potential for Run 7 for all values of $R_{\max}$ and $R_{\min}$. The resulting measured fit parameters can be found in Tab. B.4.

Range	A	B	C	χ^2/dof
[1:7]	0.13404 (0.00004)	-0.39058 (0.00009)	0.80365 (0.00013)	2.73e+03
[2:7]	0.12597 (0.00007)	-0.47507 (0.00101)	0.86204 (0.00074)	7.07e+02
[3:7]	0.11830 (0.00001)	-0.62631 (0.00330)	0.93256 (0.00175)	1.81e+02
[4:7]	0.11184 (0.00043)	-0.78996 (0.00342)	0.99834 (0.00048)	1.08e+02
[5:7]	0.13424 (0.00123)	-0.02306 (0.07277)	0.73326 (0.02735)	4.08e-15
[1:6]	0.13501 (0.00008)	-0.38864 (0.00017)	0.80074 (0.00025)	1.72e+03
[2:6]	0.12767 (0.00023)	-0.46062 (0.00057)	0.85142 (0.00088)	6.25e+02
[3:6]	0.11810 (0.00040)	-0.62907 (0.00329)	0.93408 (0.00089)	1.78e+02
[4:6]	0.10142 (0.00058)	-1.00764 (0.01020)	1.09427 (0.00261)	1.45e-12
[1:5]	0.13617 (0.00007)	-0.38632 (0.00013)	0.79726 (0.00020)	2.98e+02
[2:5]	0.13219 (0.00011)	-0.42329 (0.00023)	0.82372 (0.00037)	6.82e+01
[3:5]	0.12521 (0.00049)	-0.53187 (0.00834)	0.88017 (0.00384)	3.89e-15
[1:4]	0.13800 (0.00016)	-0.38267 (0.00032)	0.79178 (0.00048)	2.07e+01
[2:4]	0.13700 (0.00063)	-0.39044 (0.00181)	0.79768 (0.00167)	1.99e-10
[1:3]	0.13844 (0.00009)	-0.38178 (0.00017)	0.79046 (0.00026)	2.27e-12

Table B.5: Fit parameters for the fit to the Cornell potential for RUN 8. The first column shows the relevant fit range. The central columns show the fit parameters from a fit to $Ax + B/x + C$. The figures in brackets are statistical errors obtained using a 68% confidence interval over the set of 1000 bootstraps. The final column shows the χ^2 per degree of freedom for the best fit. The relevent plots are those in Fig. B-5.

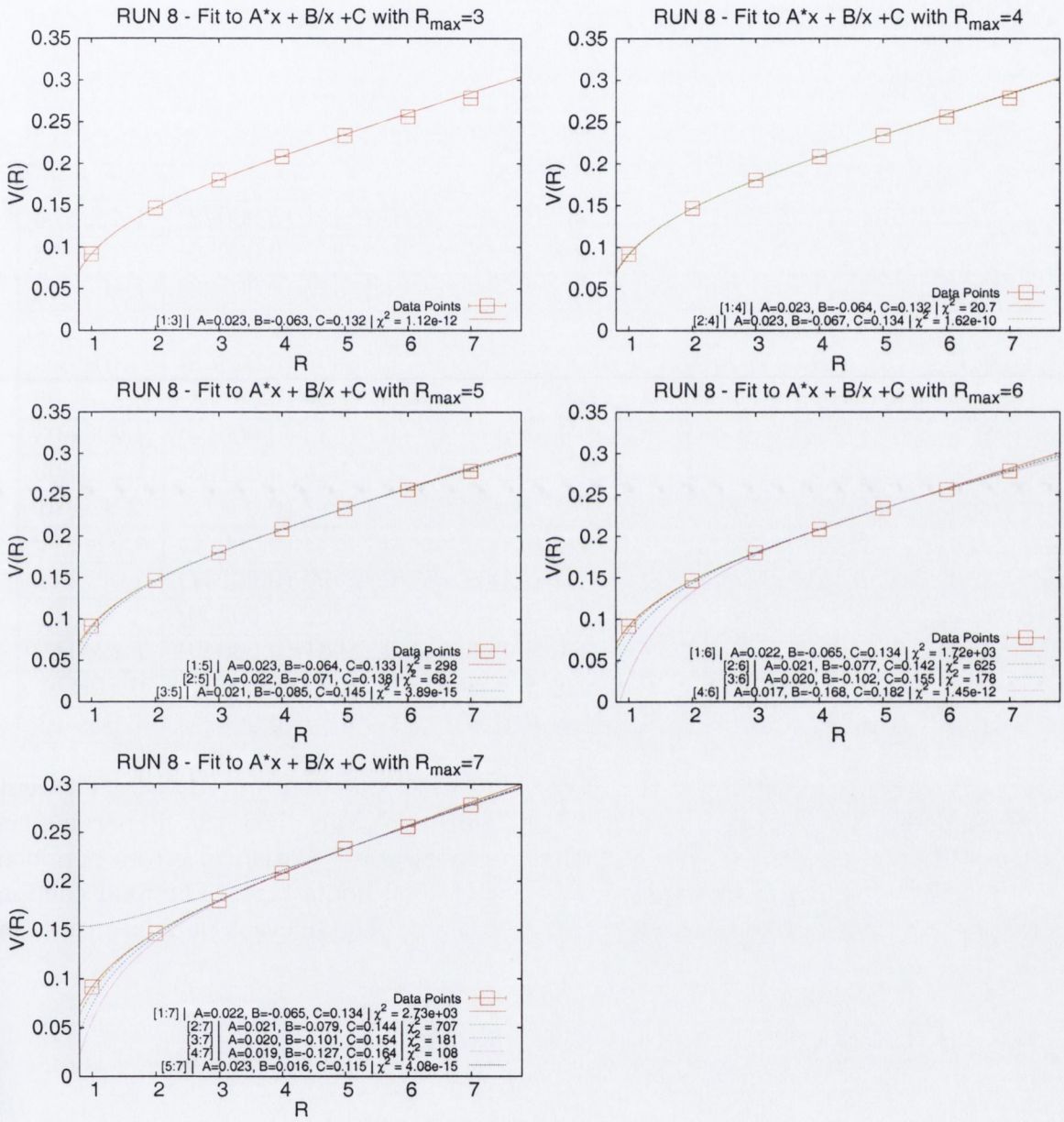

Figure B-5: Fits to the Cornell Potential for Run 8 for all values of $R_{\max}$ and $R_{\min}$. The resulting measured fit parameters can be found in Tab. B.5.

Range	A	B	C	χ^2/dof
[1:7]	0.16517 (0.00007)	-0.35537 (0.00014)	0.75801 (0.00022)	1.42e+04
[2:7]	0.14736 (0.00011)	-0.52453 (0.00078)	0.87820 (0.00056)	7.37e+03
[3:7]	0.11611 (0.00030)	-1.09459 (0.00316)	1.15336 (0.00228)	1.46e+03
[4:7]	0.08371 (0.00093)	-1.92886 (0.00901)	1.48770 (0.00312)	2.42e+02
[5:7]	0.13638 (0.00279)	-0.13330 (0.11594)	0.86602 (0.02858)	1.01e-14
[1:6]	0.16772 (0.00008)	-0.35027 (0.00016)	0.75037 (0.00024)	6.37e+03
[2:6]	0.15605 (0.00018)	-0.45559 (0.00201)	0.82635 (0.00074)	4.40e+03
[3:6]	0.12310 (0.00022)	-0.99662 (0.00488)	1.09995 (0.00102)	1.26e+03
[4:6]	0.06009 (0.00042)	-2.42188 (0.02698)	1.70517 (0.00477)	2.82e-10
[1:5]	0.16978 (0.00002)	-0.34615 (0.00004)	0.74418 (0.00006)	4.64e+02
[2:5]	0.16729 (0.00016)	-0.36781 (0.00010)	0.75999 (0.00047)	4.03e+02
[3:5]	0.14922 (0.00017)	-0.63933 (0.00436)	0.90302 (0.00299)	2.55e-13
[1:4]	0.17140 (0.00006)	-0.34290 (0.00013)	0.73931 (0.00019)	1.22e+02
[2:4]	0.17809 (0.00006)	-0.29286 (0.00080)	0.70091 (0.00131)	1.50e-14
[1:3]	0.16892 (0.00009)	-0.34786 (0.00019)	0.74674 (0.00028)	6.55e-12

Table B.6: Fit parameters for the fit to the Cornell potential for RUN 9. The first column shows the relevant fit range. The central columns show the fit parameters from a fit to $Ax + B/x + C$. The figures in brackets are statistical errors obtained using a 68% confidence interval over the set of 1000 bootstraps. The final column shows the χ^2 per degree of freedom for the best fit. The relevent plots are those in Fig. B-6.

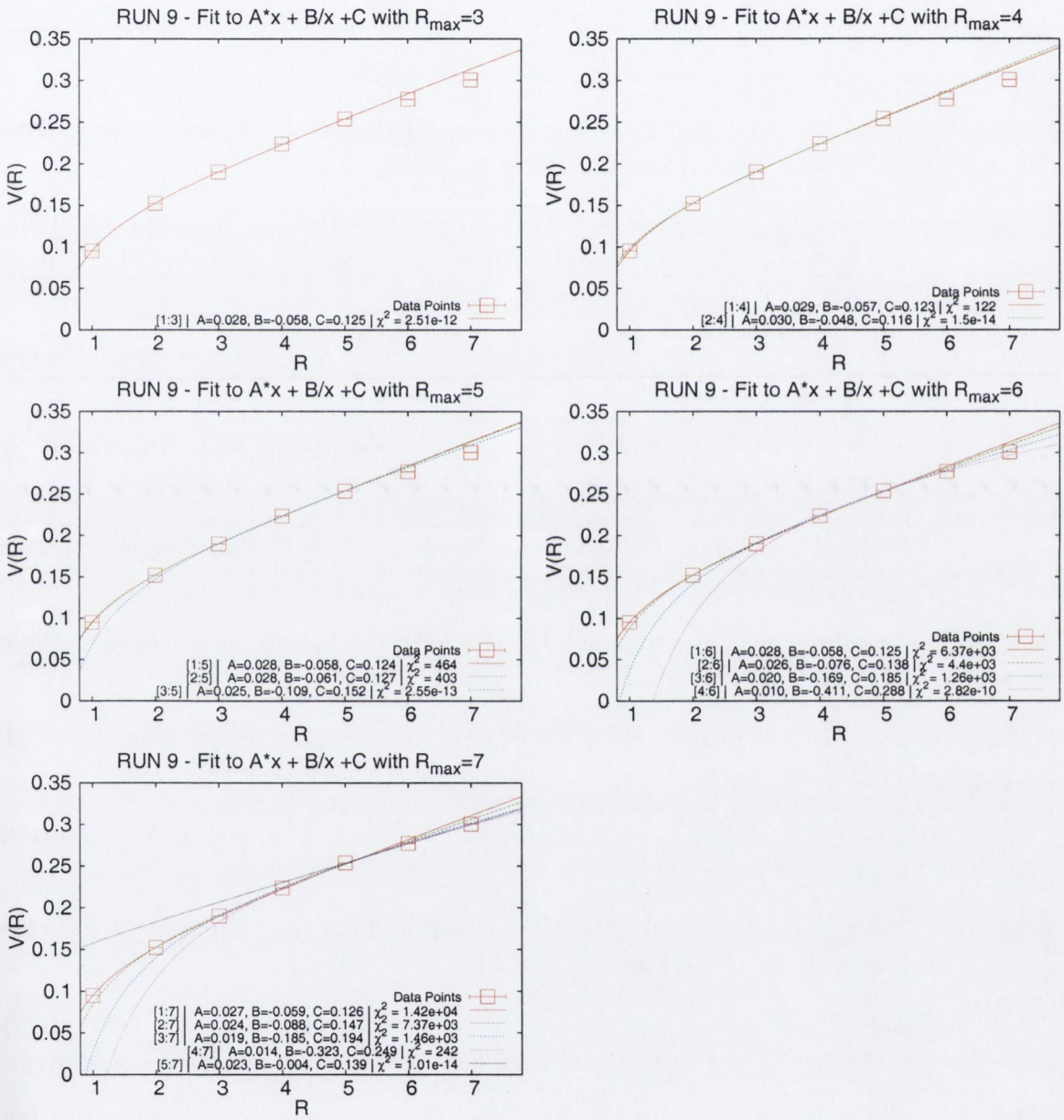

Figure B-6: Fits to the Cornell Potential for Run 9 for all values of $R_{\max}$ and $R_{\min}$. The resulting measured fit parameters can be found in Tab B.6.

Bibliography

[1] J. D. Jackson, *Classical Electrodynamics 3rd Ed.*, John Wiley & Sons, New York and Chichester, 1998, ISBN: 978-0-471-30932-1.

[2] S. F. Novaes, *Standard Model: An Introduction*,"Particle and Fields", Proc. X J. A. Swieca Summer School (World Scientific, Singapore, 2000), [hep-ph/0001283].

[3] M. E. Peskin, D. V. Schroeder, *An Introduction to Quantum Field Theory*, Westview Press (1995), ISBN: 0-202-50397-2.

[4] R. P. Feynman, *Very High-Energy Collisions of Hadrons*, Phys. Rev. Lett. 23, 1415-1417 (1969).

[5] D.J. Gross, F. Wilczek, *Ultraviolet Behavior of Non-Abelian Gauge Theories*, Phys. Rev. Lett. 30, 1343-1346 (1973).

[6] H. D. Politzer, *Reliable Perturbative Results for Strong Interactions?*, Phys. Rev. Lett. 30, 1346-1349 (1973).

[7] S. Coleman, D.J. Gross, *Price of Asymptotic Freedom*, Phys. Rev. Lett. 31, 851-854 (1973).

[8] M. A. Luty, J. March-Russell, *Baryons from Quarks in the 1/N Expansion*, Nucl. Phys. B426, 71-93 (1994), [hep-ph/9310369].

[9] U. van Kolck, L.J. Abu-Raddad, D.M. Cardamone, *Introduction to Effective Field Theories in QCD*, [nucl-th/0205058].

[10] G. Ecker, *Chiral perturbation theory*, Prog. Part. Nucl. Phys. 35, 1-80 (1995), [hep-ph/9501357].

[11] B. Ananthanarayan, *Review of chiral perturbation theory*, Pramana 61, 911-920 (2003), [hep-ph/0304061].

[12] S. Sharpe, R. Singleton, *Spontaneous Flavor and Parity Breaking with Wilson Fermions*, Phys. Rev. D58 074501 (1998), [hep-lat/9804028].

[13] S. Aoki, *Chiral perturbation theory with Wilson-type fermions including a^2 effects: $N_f = 2$ degenerate case*, Phys.Rev. D68, 054508 (2003), [hep-lat/0306027].

[14] C. Allton et al., *Physical Results from 2+1 Flavor Domain Wall QCD and SU(2) Chiral Perturbation Theory.*, Phys. Rev. D78 114509 (2008), [hep-lat/0804.0473].

[15] D. Gross, *Gauge Theory-Past, Present, and Future?*, Chinese Journal of Physics Vol. 30, No. 7 Dec. 1992.

[16] H. Georgi, *Lie Algebras in Particle Physics*, Perseus Books Group, ISBN: 978-0738202334.

[17] H. J. Rothe, *Lattice Gauge Theories. An introduction*, World Scientific Lecture Notes in Physics - Vol. 74.

[18] G. P. Lepage, *Lattice QCD for Novices*, [hep-lat/0506036].

[19] I. Montvay, G. Münster, *Quantum Fields on a Lattice*, Cambridge University Press (2003). ISBN: 0-521-40432-0.

[20] R. Gupta, *Introduction to Lattice QCD*, [hep-lat/9807028].

[21] N. H. Christ, R. Friedberg, T. D. Lee, *Random lattice field theory: General formulation*, Nucl. Phys. B202, 89-125 (1982).

[22] M. Lüscher, *Volume dependence of the energy spectrum in massive quantum field theories. I. Stable particle states*, Commun. Math. Phys. 104, 177-206 (1986).

[23] B. Orth, T. Lippert, K. Schilling, *Finite-size effects in lattice QCD with dynamical Wilson fermions*, Phys. Rev. D72, 014503 (2005).

[24] S. Aoki, T. Umemura, M. Fukugita, N. Ishizuka, H. Mino, M. Okawa, A. Ukawa, *Finite-size effects of hadron masses in lattice QCD: A comparative study for quenched and full QCD simulations*, Phys. Rev. D50, 486-494 (1994).

[25] F. Butler, H. Chen, J. Sexton, A. Vaccarino, D. Weingarten, *Hadron mass predictions of the valence approximation to lattice QCD*, Nucl. Phys. B430 179 (1994); Phys. Rev. Lett. 70, 2849-2852 (1993).

[26] K. Wilson, *Confinement of quarks*, Phys. Rev. D10, 2445-2459 (1974).

[27] D. H. Adams, *Simplified Test of Universality in Lattice QCD*, Phys. Rev. Lett. 92, 162002 (2004), [hep-lat/0312025].

[28] D. H. Adams, *Testing universality and the fractional power prescription for the staggered fermion determinant*, [hep-lat/0409013v1].

[29] K. Wilson, *Quarks and Strings on a Lattice*, New Phenomena In Subnuclear Physics. Part A. Proceedings of the First Half of the 1975 International School of Subnuclear Physics, Erice, Sicily, July 11 - August 1, 1975, ed. A. Zichichi, Plenum Press, New York, 1977, 69-142, Also published in *Proc. Gauge theories and modern field theory* Boston Conf. (1975).

[30] K. Symanzik, *Continuum Limit and Improved Action in Lattice Theories (I). Principles and ϕ^4 theory*, Nucl. Phys. B226, 187-204 (1983).

[31] K. Symanzik, *Continuum Limit and Improved Action in Lattice Theories (II). $\mathcal{O}(N)$ non-linear sigma model in perturbation theory*, Nucl. Phys. B226, 205-227 (1983).

[32] P. Weisz, *Continuum Limit Improved Lattice Action for Pure Yang-Mills Theory(I)*, Nucl. Phys. B212, 1 (1983).

[33] G. Curci, P. Menotti, G. Paffauti, *Symanzik's Improved Lagrangian for Lattice Gauge Theory*, Phys. Lett. B130, 205-214 (1983).

[34] P. Weisz, R. Wohlert, *Continuum Limit Improved Lattice Action for Pure Yang-Mills Theory(II)*, Nucl. Phys. B236, 397-422 (1984).

[35] M. Lüscher and P. Weisz, *On-shell improved lattice gauge theories*, Commun. Math. Phys. 97, 59-98 (1985), [Erratum-ibid. 98 (1985) 433].

[36] P. B. Mackenzie, G. P. Lepage, *Viability of lattice perturbation theory*, Phys. Rev. D48, 2250-2264 (1993).

[37] M. Alford, W. Dimm, G. P. Lepage, G. Hockney, P. B. Mackenzie, *Lattice QCD on Small Computers*, Phys.Lett. B361, 87-94 (1995), [hep-lat/9507010].

[38] H. P. Shanahan et. al., *The effect of tree-level and mean-field improvement on the light-hadron spectrum in quenched QCD*, Phys.Rev. D55, 1548-1558 (1997), [hep-lat/9608063].

[39] K. Wilson, J. Kogut, *The renormalization group and the ϵ expansion*, Phys. Rep. C12, 75-199 (1974).

[40] K. Wilson, *The renormalization group: Critical phenomena and the Kondo problem*, Rev. Mod. Phys. 47, 773-840 (1975).

[41] P. Hasenfratz, F. Niedermayer, *Perfect lattice action for asymptotically free theories*, Nucl. Phys. B414, 785-814 (1994), [hep-lat/9308004].

[42] P. Hasenfratz, *The theoretical background and properties of perfect actions*, [hep-lat/9803027v1].

[43] Y. Iwasaki, *Renormalization Group Analysis of Lattice Theories and Improved Lattice Action. II. Four-Dimensional Nonabelian Su(N) Gauge Model.*, UTHEP-118 (1983). Nucl. Phys. B258, 141-156 (1985).

[44] P. de Forcrand et. al., *Renormalization group flow of SU(3) lattice gauge theory - Numerical studies in a two coupling space*, Nucl. Phys. B577, 263-278 (2000), [hep-lat/9911033].

[45] S. Necco, *Universality and scaling behavior of RG gauge actions.*, Nucl. Phys. B683, 137-167 (2004). [hep-lat/0309017].

[46] Beinlich, B.; Karsch, F.; Laermann, E., *Improved Actions for QCD Thermodynamics on the Lattice*, Nucl. Phys. B462, 415-436 (1996), [hep-lat/9510031].

[47] B. Sheikholeslami, R. Wohlert, *Improved continuum limit lattice action for QCD with wilson fermions*, Nucl. Phys. B259, 572-596 (1985).

[48] M. Alford, T. Klassen, P. Lepage, *A quark action for very coarse lattices*, Phys.Rev. D58. 034503 (1998). [hep-lat/9712005].

[49] T. R. Klassen, *The Anisotropic Wilson Gauge Action*, Nucl. Phys. B533. 557-575 (1998), [hep-lat/9803010].

[50] C. Morningstar, M. J. Peardon, *The glueball spectrum from novel improved actions*, Nucl. Phys. Proc. Suppl. 83, 887-889 (2000), [hep-lat/9911003].

[51] H. W. Hamber, C. Min Wu, *Some predictions for an improved fermion action on the lattice*, Phys. Lett. B133, 351-358 (1983).

[52] Justin Foley, Alan O Cais, Mike Peardon, Sinead M. Ryan, *A non-perturbative study of the action parameters for anisotropic-lattice quarks*, Phys.Rev. D73, 014514 (2006), [hep-lat/0405030].

[53] W. Bardeen, A. Duncan, E. Eichten, G. Hockney, H. Thacker, *Light quarks, zero modes, and exceptional configurations.*, Phys. Rev. D57, 1633-1641 (1998), [hep-lat/9705008]; Phys. Rev. D57, 1633-1641 (1998), [hep-lat/9705008].

[54] C. T. H. Davies et al., *High-Precision Lattice QCD Confronts Experiment*, Phys. Rev. Lett. 92, 022001 (2004).

[55] J. Viehoff et al., *Improving Stochastic Estimator Techniques for Disconnected Diagrams*, Nucl. Phys. Proc. Suppl. 63, 269-271 (1998), [hep-lat/9710050v2].

[56] H. Neff, N. Eicker, Th. Lippert, J. W. Negele, K. Schilling, *On the low fermionic eigenmode dominance in QCD on the lattice.* Phys. Rev. D64, 114509 (2001). [hep-lat/0106016].

[57] J. Foley et al., *Practical all-to-all propagators for lattice QCD*, Comput. Phys. Commun. 172, 145-162 (2005), [hep-lat/0505023].

[58] W. H. Press, S. A. Teukolsky, W. T. Vetterling, B. P. Flannery, *Numerical Recipes in C*, Cambridge University Press (1992). ISBN:978-0521431088.

[59] R. Fletcher and M.J.D. Powell, *A rapidly convergent descent method for minimization*, Comput. J., 6, 163-168 (1963/1964).

[60] R. Fletcher, *Practical methods of optimization*, Chichester : Wiley, (2001). ISBN:978-0471494638.

[61] A. Hasenfratz, F. Knechtli, *Flavor Symmetry and the Static Potential with Hypercubic Blocking*, Phys. Rev. D64, 034504 (2001) [hep-lat/0103029].

[62] S. Dürr, *Gauge action improvement and smearing*, Comput. Phys. Commun. 172, 163-186 (2005), [hep-lat/0409141].

[63] M. Albanese et al., *Glueball Masses and String Tension in Lattice QCD*, Phys. Lett. B192, 163-169 (1987).

[64] C. Morningstar and M. J. Peardon, *Analytical smearing of SU(3) link variables in lattice QCD*, Phys. Rev. D69, 054501 (2004), [hep-lat/0311018].

[65] H.B Nielsen, M. Ninomiya, *Absence of Neutrinos on a lattice*, Nucl. Phys. B185 20-64 (1981).

[66] L. H. Karsten, J. Smit, *Lattice Fermions: Species Doubling, Chiral Invariance, and the Triangle Anomaly* Nucl. Phys. B183, 103-140 (1981).

[67] P. Hasenfratz, *Chiral symmetry on the lattice*, [hep-lat/0406033].

[68] M. Lüscher, *Exact chiral symmetry on the lattice and the Ginsparg-Wilson relation*, Phys. Lett. B428, 342-345 (1998), [hep-lat/9802011].

[69] S. D. Cohen, *QCD, Symmetry Breaking and the Random Lattice*, Nucl. Phys. B - Proc. Suppl. Vol. 140, 698-700, (2005).

[70] J. Kogut, L. Susskind, *Hamiltonian formulation of Wilson's lattice gauge theories*, Phys. Rev. D11, 395-408 (1975).

[71] B. Bunk, M. Della Morte, K. Jansen, F. Knechtli,*Locality with staggered fermions*, Nucl. Phys. B697, Issues 1-2, 343-362 (2004).

[72] A. Hasenfratz, R. Hoffmann, *Validity of the Rooted Staggered Determinant in the continuum limit*, Phys.Rev. D74, 014511 (2006), [hep-lat/0604010].

[73] P. H. Ginsparg, K. G. Wilson, *A remnant of chiral symmetry on the lattice*, Phys. Rev. D25, 2649 (1982).

[74] I. Horvath, *Ginsparg-Wilson Relation and Ultralocality*, Phys. Rev. Lett. 81, 4063-4066 (1998), [hep-lat/9808002v2].

[75] D. B. Kaplan, *A method for Simulating Chiral Fermions on the Lattice*, Phys. Lett. B288, 342-347 (1992), [hep-lat/9206013].

[76] Rajamani Narayanan, Herbert Neuberger, *Infinitely many regulator fields for chiral fermions*, Phys. Lett. B302, 62-69 (1993), [hep-lat/9212019].

[77] H. Neuberger, *Exactly massless quarks on the lattice*, Phys. Lett. B417, 141 (1998).

[78] H. Neuberger, *Overlap lattice Dirac operator and dynamical fermions*, Phys. Rev. D60, 065006 (1999).

[79] R. Frezzotti, P. A. Grassi, S. Sint, P. Weisz, *Lattice QCD with a chirally twisted mass term*, JHEP 0108, 58-87 (2001), [hep-lat/0101001].

[80] R. Morrin et al., *Dynamical QCD simulations on anisotropic lattices*, Phys.Rev. D74, 014505 (2006), [hep-lat/0602021].

[81] I.T Drummond, R.R Horgan, H. Shanahan, M. J. Peardon, *Measuring the aspect ratio renormalisation of anisotropic-lattice gluons*, Phys. Rev. D63, 074501 (2001), [hep-lat/0003019].

[82] S. Duane, A. D. Kennedy, B. J. Pendleton and D. Roweth, *Hybrid Monte Carlo*, Phys. Lett B196, 216-222 (1987).

[83] R. Morrin et al., *Tuning anisotropies for dynamical gauge configurations*, PoS LAT2005 (2005) 236-242, [hep-lat/0510016].

[84] R. Morrin et al., *Charmonium spectral functions in $N_f = 2$ QCD*, PoS LAT2005 (2005) 176-182, [hep-lat/0509115].

[85] G. Aarts et al., *Mesons at high temperature in $N_f = 2$ QCD*, Nucl. Phys. Proc. Suppl. 153, 296-299 (2006), [hep-lat/0511028].

[86] G. Aarts et al., *Charmonium spectral functions in two-flavour QCD*, Nucl. Phys. A785, 198-201 (2007), [hep-lat/0608009].

[87] G. Aarts et al., *Charmonium spectral functions in $N_f = 2$ QCD at high temperature*, PoS(LAT2006) 126-132, [hep-lat/0610065].

[88] J. C. Collins and M.J. Perry, *Superdense Matter: Neutrons or Asymptotically Free Quarks?*, Phys. Rev. Lett. 34, 1353-1356 (1975).

[89] *Results from the first three years at RHIC: Hunting the Quark Gluon Plasma*, "http://www.bnl.gov/npp/Hunting the QGP.pdf".

[90] T. Ludlam, *Experimental results from the early measurements at RHIC; hunting for the quark-gluon plasm*, Nucl. Phys. A750, 9-29 (2005).

[91] I. Belikov, *Physics of the ALICE Experiment*, [hep-ex/0605035v1].

[92] E. Laermann, O. Philipsen, *The Status of Lattice QCD at Finite Temperature*, Ann. Rev. Nucl. Part. Sci. 53, 163-198 (2003). [hep-ph/0303042].

[93] A.D. Linde, *Infrared problem in the thermodynamics of the Yang-Mills gas.* Phys. Lett. B96, 289-292 (1980).

[94] Y. Nakahara, M. Asakawa, T. Hatsuda, *Hadronic Spectral Functions in Lattice QCD*, Phys.Rev. D60, 091503 (1999). [hep-lat/9905034v2].

[95] T. Umeda, *Constant contribution in meson correlators at finite temperature.* [hep-lat/0701005v2].

[96] C. Bernard et al., *Equation of state for two flavor QCD at $N_t = 6$.* Phys. Rev. D55, 6861-6869 (1997). [hep-lat/9612025].

[97] J. Engels et al., *Thermodynamics of four flavour QCD with improved staggered fermions.* Phys. Lett. B396, 210-216 (1997). [hep-lat/9612018].

[98] F. Karsch, E. Laermann, and A. Peikert, *The Pressure in two flavor, (2+1)-flavor and three flavor QCD.* Phys. Lett. B478, 447-455 (2000). [hep-lat/0002003].

[99] CP-PACS Collaboration, A. Ali Khan et al., *Equation of state in finite-temperature QCD with two flavors of improved Wilson quarks.* Phys. Rev. D63, 034502 (2001). [hep-lat/0103028].

[100] F. Karsch, *SU(N) Gauge Theory Couplings on Asymmetric Lattices*, Nucl. Phys. B205, 285-300 (1982) .

[101] S. Huang, J. Potvin, C. Rebbi, S. Sanielevici, *Surface tension in finite-temperature quantum chromodynamics*, Phys. Rev. D42, 2864-2874 (1990).

[102] G. Burgers, F. Karsch, A. Nakamura, I. O. Stamatescu, *QCD on anisotropic lattices*, Nucl. Phys. B304, 587-600 (1988).

[103] E. Eichten, K. Gottfried, T. Kinoshita, J. Kogut, K. D. Lane, and T. -M. Yan, *Spectrum of Charmed Quark-Antiquark Bound States*, Phys. Rev. Lett. 34, 369-372 (1975).

[104] G.S. Bali and K. Schilling. *Running Coupling and the Lambda-Parameter from SU(3) Lattice Simulations.* Phys. Rev. D47, 661-672 (1993). [hep-lat/9208028].

[105] C. Michael. *The Running Coupling from Lattice Gauge Theory.* Phys. Lett. B283, 103-106 (1992). [hep-lat/9205010].

[106] C. B. Lang and C. Rebbi. *Potential and Restoration of Rotational Symmetry in SU(2) Lattice Gauge Theory.* Phys. Lett. B115, 137-142 (1982).

[107] J. L. Richardson, *The heavy quark potential and the Υ, J/Ψ systems.* Phys. Lett. B82, Issue 2, 272-274 (1979).

[108] C. Alexandrou, S. Guesken, F. Jegerlehner, K. Schilling, R. Sommer. *The Static Approximation of Heavy-Light Quark-Systems - A Systematic Lattice Study*, Nucl. Phys. B414, 815-855 (1994). [hep-lat/9211042].

[109] U. Glässner, S. Güsken, H. Hoeber, Th. Lippert, G. Ritzenhöfer, K. Schilling, G. Siegert, A. Spitz, A. Wachter. *First Evidence of N_f-Dependence in the QCD Interquark Potential.* Phys. Lett. B383, 98-104 (1996). [hep-lat/9604014].

[110] F. Karsch and I. Stamatescu, *QCD Thermodynamics with Light Quarks: Quantum Corrections to the Fermionic Anisotropy Parameter*, Phys. Lett. B227, 153-160 (1989).

[111] R. Trinchero, *One-loop fermion contribution in an asymmetric lattice regularization of SU(N) gauge theories*, Nucl. Phys B227, 61-74 (1983).

[112] T. Blum, Leo Kärkaäinen, D. Toussaint, S. Gottlieb, *β- function and equation of state for QCD with two flavors of quarks*, Phys. Rev. D51, 5153-5164 (1995).

[113] G.S. Bali, Th. Düssel, Th. Lippert. Neff, Z. Prkain and K. Schilling.*String breaking with dynamical Wilson fermions.* Nucl. Phys. B Proc. Suppl. Vol. 140, 609-611 (2005). [hep-lat/0409137].

[114] F. Knechtli, R. Sommer. *String breaking as a mixing phenomenon in the SU(2) Higgs model.* Nucl. Phys. B590, 309-328 (2000). [hep-lat/0005021].

[115] G. S. Bali, H. Neff, T. Duessel, T. Lippert, K. Schilling. *Observation of String Breaking in QCD.* Phys. Rev. D71 114513 (2005). [hep-lat/0505012v2].

[116] R. Sommer. *A New Way to Set the Energy Scale in Lattice Gauge Theories and its Application to the Static Force and α_s in SU(2) Yang–Mills Theory.* Nucl. Phys. B411, 839-854 (1994). [hep-lat/9310022].

[117] S. Necco, R. Sommer. *The $N_f = 0$ heavy quark potential from short to intermediate distances.* Nucl. Phys. B622, 328-346 (2002). [hep-lat/0108008].

[118] K. J. Juge et al., *The spectrum of radial, orbital and gluonic excitations of charmonium*, [hep-lat/0610124v1].

[119] S. Ejiri, Y. Iwasaki, K. Kanaya.*Non-perturbative determination of anisotropy coefficients in lattice gauge theories.* Phys.Rev. D58, 094505 (1998). [hep-lat/9806007].

[120] R. Gupta, T. Bhattacharya, *Light Quark Masses from Lattice QCD*, Phys.Rev. D55, 7203-7217 (1997), [hep-lat/9605039v3].

[121] L. Levkova, *Staggered fermion thermodynamics using anisotropic lattices..* Nucl. Phys. Proc. Suppl. 119, 520-522 (2003). [hep-lat0209069].

[122] L. Levkova, T. Manke, R. Mawhinney, *Two-flavor QCD thermodynamics using anisotropic lattices..* Phys. Rev. D73 074504 (2006). [hep-lat/0603031].